Université du Québec
Institut National de la Recherche Scientifique
Centre Énergie Matériaux Télécommunications

# RAPID SYNTHESIS OF A 2D/2D COF/$BiVO_4$ HETEROJUNCTION FOR $CO_2$ PHOTOREDUCTION

Par
Sina Moradi

Mémoire présentée pour l'obtention du grade de
Maître ès sciences (M.Sc.)
en sciences de l'énergie et des matériaux

**Jury d'évaluation**

| | |
|---|---|
| Président du jury et Examinateur interne | Prof. Daniel Guay<br>INRS-ÉMT, Université du Québec |
| Examinateur externe | Prof. Maryam Ebrahimi<br>Université de Lakehead |
| Examinateur interne | Prof. Daniel Guay<br>INRS-ÉMT, Université du Québec |
| Directeur de recherche | Prof. Dongling Ma<br>INRS-ÉMT, Université du Québec |

# REMERCIEMENTS

I would like to express my heartfelt gratitude to everyone who contributed to the completion of this thesis. A special thank you goes to my supervisors, Professor Dongling Ma, and Dr. Cristina Rodriguez Seco, for their invaluable guidance and unwavering support. I am also grateful to my family for being there for me throughout this journey.

I would like to acknowledge the support and help of my teammates, Zahra Kalantari, Gege He, Ruiqi Yang, Chen Wang, Yong Wang, Wanting He, and Ting Yu, as well as my friend Ahmed El Hattab and all the technicians and specialists at INRS-EMT.

To all those who have been a part of this journey, thank you for your assistance and encouragement. Your contributions have made a significant difference, and I am truly grateful.

# RÉSUMÉ

Les niveaux croissants d'émissions de $CO_2$ représentent une menace significative pour le climat et les écosystèmes de notre planète, soulignant le besoin urgent de solutions innovantes pour réduire les émissions, créer de nouvelles sources d'énergie respectueuses de l'environnement et éliminer les gaz à effet de serre de l'atmosphère. La réduction photocatalytique du $CO_2$, grâce à sa capacité à exploiter l'énergie solaire et à entraîner des réactions de réduction du $CO_2$, émerge comme un candidat prometteur pour relever ces défis. Les frameworks organiques covalents (COFs) se sont révélés être des candidats prometteurs pour cette fin en raison de leurs caractéristiques structurales uniques et de leurs structures poreuses bien définies et ajustables avec de nombreux sites catalytiques actifs, permettant une capture et une conversion efficaces du $CO_2$ par des processus stimulés par la lumière. Dans ce projet, nous avons cherché à développer un nanocomposite 2D/2D COF-316/$BiVO_4$ pour améliorer l'efficacité de la réduction du $CO_2$ sans recourir à des photosensibilisateurs supplémentaires en optimisant le transfert de charge à l'interface au sein de l'hétérojonction. Nous avons synthétisé le COF-316 en utilisant une nouvelle méthode de chauffage assistée par micro-ondes, réduisant le temps de réaction de 95% par rapport à la synthèse conventionnelle. Une analyse approfondie a confirmé la réussite de la synthèse du COF (COF-$316_M$) synthétisé par micro-ondes en analysant ses propriétés physiques et sa composition chimique. Le COF-$316_M$ a démontré une grande surface spécifique de 592,27 $m^2/g$, supérieure à celle du COF-$316_S$ synthétisé de manière conventionnelle (544,34 $m^2/g$). De plus, des nanofeuillets de $BiVO_4$ en 2D ont été synthétisés par une méthode synthétique colloïdale et utilisés ultérieurement pour établir une hétérojonction 2D/2D avec le COF-$316_M$ par le biais d'une synthèse in situ. Nous avons étudié les performances photocatalytiques de COF-$316_S$, COF-$316_M$, $BiVO_4$ et COF-$316_M$/$BiVO_4$ (20% - 50%) sous irradiation lumineuse visible, en phase gaz-solide, et sans avoir besoin d'agents sacrificiels ou de photosensibilisateurs supplémentaires. COF-$316_S$ a montré un taux de production de CO d'environ 2,5 µmol $g^{-1}.h^{-1}$ tandis que COF-$316_M$ a présenté une valeur plus élevée de 3,8 µmol $g^{-1}.h^{-1}$. Cette meilleure performance a été attribuée à l'amélioration de la surface BET obtenue grâce à la méthode de chauffage par micro-ondes. Cependant, l'incorporation de $BiVO_4$ dans le cadre COF a entraîné une diminution de l'activité photocatalytique par rapport à COF-

316$_S$ et COF-316$_M$. Des mesures XPS in situ ont été effectuées pour mieux comprendre le mécanisme de transfert de charge entre ces deux matériaux.

Mots clés : COF, $BiVO_4$, Photocatalyse, Réduction de $CO_2$, Hétérojonction

# Abstract

The escalating levels of $CO_2$ emissions pose a significant threat to our planet's climate and ecosystems, highlighting the urgent need for innovative solutions to reduce emissions, create novel environmentally friendly energy sources and eliminate green house gases from the atmosphere. Photocatalytic $CO_2$ reduction with its capability to harness solar energy and drive $CO_2$ reduction reactions, emerges as a promising candidate for addressing these challenges. Covalent organic frameworks (COFs) have emerged as promising candidates for this purpose due to their unique structural features, well-defined and tunable porous structures with abundant catalytic active sites, enabling efficient $CO_2$ capture and conversion through light-driven processes. In this project, we aimed to develop a 2D/2D COF-316/$BiVO_4$ nanocomposite to enhance $CO_2$ reduction efficiency without additional photosensitizers by optimizing charge transfer at the interface within the heterojunction. We synthesized COF-316 using a novel microwave-assisted heating method, reducing the reaction time by 95% compared to conventional synthesis. A deep analysis confirmed the successful synthesis of microwave-synthesized COF (COF-$316_M$) by analyzing its physical properties and chemical composition. COF-$316_M$ demonstrated a great surface area of 592.27 $m^2/g$, being larger than that of the conventionally synthesized COF-$316_S$ (544.34 $m^2/g$). Also, 2D $BiVO_4$ nanosheets were synthesized via a colloidal synthetic method and subsequently utilized to establish a 2D/2D heterojunction with COF-$316_M$ through an in-situ synthesis. We studied the photocatalytic performance of COF-$316_S$, COF-$316_M$, $BiVO_4$, and COF-$316_M$/$BiVO_4$ (20% - 50%) under visible light irradiation, in gas-solid phase, and without the need for sacrificial agents or additional photosensitizers. COF-$316_S$ showed a CO production rate of ~2.5 $\mu mol\ g^{-1}.h^{-1}$ while COF-$316_M$ exhibited a 1.52-time higher value of 3.8 $\mu mol\ g^{-1}.h^{-1}$. This higher performance was attributed to the improved BET surface area achieved through the microwave heating method. However, incorporating $BiVO_4$ into the COF framework resulted in decreased photocatalytic activity compared to COF-$316_S$ and COF-$316_M$. In-situ XPS measurements were performed to have a better understanding of charge transfer mechanism between these two materials.



**Keywords:** COF, $BiVO_4$, Photocatalysis, $CO_2$ Reduction, Heterojunction

# SOMMAIRE RÉCAPITULATIF

# SYNTHÈSE RAPIDE D'UNE HÉTÉROJONCTION COF/$BiVO_4$ 2D/2D POUR LA PHOTORÉDUCTION DU $CO_2$

## 0.1 Présentation

Les COFs (Framework organiques covalents) sont un type des polymères organiques poreux ayant une grande surface spécifique et des propriétés ajustables, ce qui les rend attractifs pour leur utilisation en photocatalyse[1]. Leur surface spécifique peut varier en fonction de leur structure et de leur méthode de synthèse[2], [3]. Cependant, les valeurs rapportées pour la surface BET des COFs se situent généralement dans une plage de 300 à 2500 $m^2/g$, ce qui est supérieur à celui des oxydes métalliques dont la surface BET varie généralement de quelques dizaines à quelques centaines de $m^2/g$[4]–[6]. Un autre grand avantage des COFs par rapport à d'autres types de photocatalyseurs est leur capacité à absorber une large gamme de longueurs d'onde lumineuses, y compris la lumière visible, ce qui permet une utilisation efficace de l'énergie solaire[7], [8]. De plus, leur structure peut être conçue et adaptée pour optimiser les performances catalytiques et la sélectivité envers les produits désirés par le biais de différentes méthodes telles que la métallation ou la formation d'hétérojonctions[9], [10]. Ces propriétés démontrent le potentiel des COFs en tant que photocatalyseurs hautement efficaces et sélectifs pour les applications de réduction du $CO_2$[3].

Le COF-316 lié par dioxane, défini par sa stabilité robuste, sa structure 2D, ses nombreux micropores, une surface étendue (>500 $m^2/g$) et une large absorption lumineuse dans les UV et le visible, sert de photocatalyseur pour la réduction du $CO_2$ sous lumière visible[11]. La structure chimique du COF est illustrée dans la figure 0.1. Il peut adsorber efficacement les molécules de $CO_2$ grâce à ses groupes nitrile (-CN), et les convertir principalement en gaz CO[12]. Cependant, malgré ses performances photocatalytiques impressionnantes, le COF-316 présente certaines limitations importantes, telles qu'une faible capacité d'oxydation et un taux élevé de recombinaison des porteurs de charge, ce qui limite son activité photocatalytique, notamment dans les milieux aquatiques. Par

conséquent, les chercheurs travaillent à améliorer ses performances en incorporant d'autres matériaux ou en modifiant sa structure[7], [11], [13].

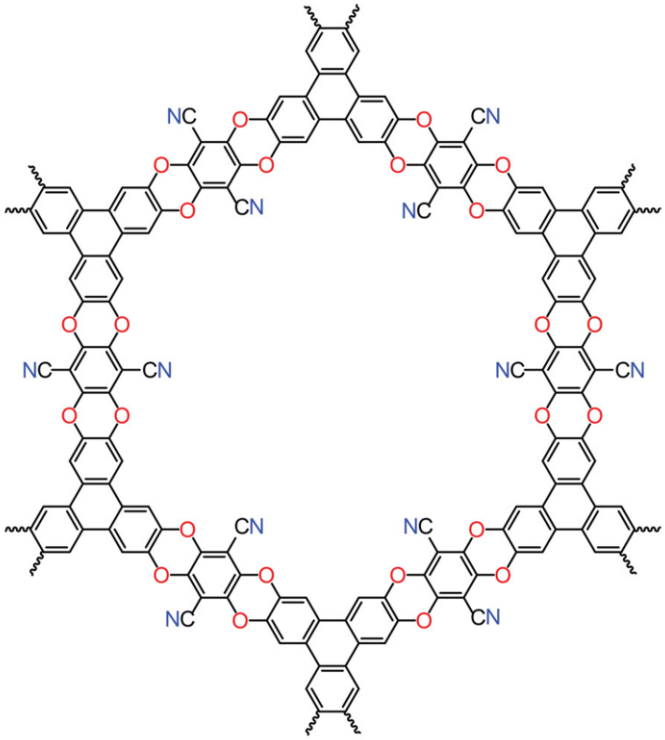


Figure 0.1. Structure chimique du COF-316.

Les matériaux 2D, tels que le COF-316, ont gagné une traction significative dans le domaine de la photocatalyse en raison de leurs nombreux avantages par rapport aux matériaux massifs[14]. Comparés à leurs homologues massifs, les matériaux 2D présentent généralement des surfaces spécifiques plus élevées, permettant une interaction accrue avec les molécules de $CO_2$ réactives. De plus, ils offrent des distances de migration plus courtes des porteurs de charge de l'intérieur vers la surface, facilitant ainsi des processus photocatalytiques plus efficaces. De plus, les matériaux 2D possèdent une concentration plus élevée de défauts catalytiquement utiles (par exemple, des lacunes d'oxygène) et une abondance d'atomes de surface avec des sites de coordination insaturés[15], [16]. Ces caractéristiques contribuent à la disponibilité d'un plus grand nombre de sites actifs pour les réactions catalytiques. Plus important encore,

la combinaison de nanomatériaux 2D pour former des hétérojonctions 2D/2D peut donner lieu à des effets synergiques résultant d'une séparation accrue des charges et d'une recombinaison réduite des porteurs $e^-/h^+$. Ces améliorations sont obtenues grâce à un meilleur contact de surface et une surface d'interface agrandie[17], [18].

Les semi-conducteurs à base de bismuth ont attiré une attention substantielle en tant que classe de matériaux en 2D, en raison de leurs propriétés physico-chimiques distinctives[19]. Notamment, les nanofeuillets de $BiVO_4$ présentent une activité photocatalytique remarquable pour le fractionnement de l'eau en raison de leur structure électronique avantageuse et de leur faible bande interdite de 2,4 eV[20]. Cette bande interdite étroite facilite l'absorption de la lumière visible, ce qui se traduit par d'excellentes performances. De plus, sa surface spécifique élevée fournit de nombreux sites actifs pour les réactions photocatalytiques, amplifiant ainsi ses performances catalytiques[19]. Sa capacité hautement oxydante permet au système d'oxyder l'eau, éliminant ainsi le besoin d'un agent sacrificiel[19], [20]. Ainsi, la combinaison de $BiVO_4$ et du COF-316 pour former un nanocomposite 2D/2D peut potentiellement créer un système photocatalytique hautement efficace et polyvalent qui peut entraîner efficacement la réduction du $CO_2$ en présence d'eau.

La synthèse assistée par micro-ondes des COFs a été constatée pour réduire significativement le temps de réaction. L'irradiation micro-ondes est connue pour chauffer efficacement les mélanges réactionnels grâce à l'interaction des rayonnements électromagnétiques avec les molécules polaires, principalement par rotation de dipôles et conduction ionique. Cette chauffe rapide et sélective peut entraîner plusieurs facteurs influençant la cinétique de réaction : (i) transfert de chaleur amélioré : le chauffage par micro-ondes génère de la chaleur localisée à l'intérieur du récipient de réaction. Cela permet un chauffage plus rapide et uniforme de l'ensemble du mélange réactionnel par rapport aux méthodes de chauffage conventionnelles. Par conséquent, les limitations de transfert de chaleur sont réduites, ce qui peut accélérer les taux de réaction, (ii) transfert d'énergie efficace : les micro-ondes se couplent directement avec les molécules réactives qui ont des moments dipolaires. Ce transfert d'énergie efficace peut fournir l'énergie d'activation nécessaire aux réactions chimiques de manière plus efficace que les

méthodes de chauffage traditionnelles, qui peuvent dépendre d'une diffusion de chaleur plus lente, (iii) distribution uniforme de la température : le chauffage par micro-ondes a tendance à créer une distribution de température plus uniforme à l'intérieur du récipient de réaction, minimisant les gradients de température. Cela peut prévenir une progression inégale de la réaction, contribuant ainsi à un meilleur contrôle cinétique.

Dans ma thèse, j'ai poursuivi trois objectifs principaux : (i) développer une nouvelle approche assistée par micro-ondes pour la synthèse du COF-316, réduisant considérablement le temps de synthèse, (ii) créer un nouveau nanocomposite 2D/2D COF-316/$BiVO_4$, visant à améliorer le transport des charges et, par conséquent, à améliorer l'efficacité de la réduction du $CO_2$ en formant une structure nanocomposite 2D/2D et en augmentant la surface catalytique active, (iii) établir un système de transfert de charges en mode Z, permettant une performance élevée de réduction photocatalytique du $CO_2$ en phase gaz-solide sans avoir besoin d'agents sacrificiels ou de photosensibilisateurs supplémentaires (voir Fig. 0.2).

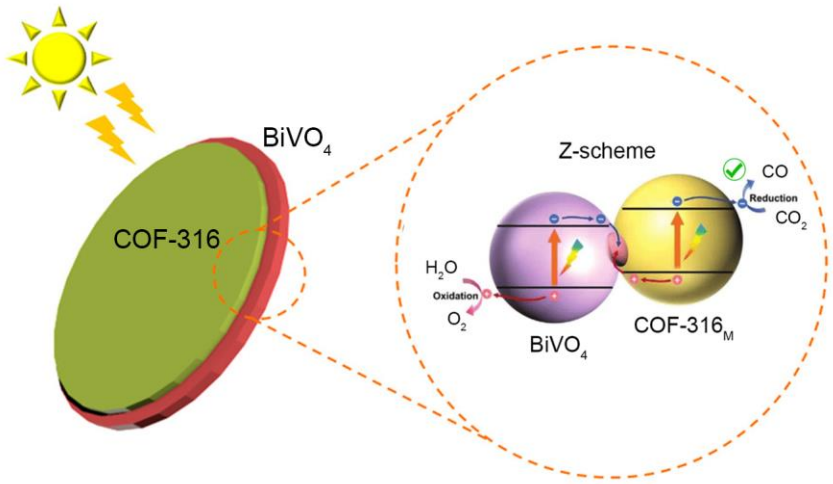


Figure 0.2. Mécanisme souhaité de transfert de charge en mode Z pour la réduction photocatalytique du $CO_2$ en 2D/2D.

Nous avons rapporté une nouvelle méthode de synthèse assistée par micro-ondes pour le COF-316 qui réduit le temps de réaction de 95% et développé un nouveau composite 2D/2D COF-$316_M$/$BiVO_4$ pour la réduction du $CO_2$ sous irradiation de lumière visible.

Contrairement aux techniques traditionnelles, cette méthode de chauffage par micro-ondes permet un chauffage plus rapide et plus efficace de l'intérieur[21]. Cette nouvelle approche, tirant parti des avantages des micro-ondes, rationalise le processus de synthèse, le rendant plus rapide et plus économe en énergie[22]. Les échantillons ont été caractérisés à l'aide de diverses techniques analytiques et leur performance photocatalytique a été examinée en phase gaz-solide en présence d'eau sans agent sacrificiel ni photosensibilisateur supplémentaire.

## 0.2 Caractérisation structurale et morphologique

La diffraction des rayons X (XRD) a été effectuée pour valider la structure cristalline des nanomatériaux et du nanocomposite. La figure 0.3a-b montre les diffractograms des échantillons de COF-316$_S$ et COF-316$_M$. Les pics aux valeurs 2θ de 4,34°, 8,8°, 11,22° et 26,9° correspondent respectivement aux plans de réflexion (100), (200), (210) et (001), indiquant une structure cristalline ordonnée de phase orthorhombique[12]. Les motifs de XRD de COF-316$_S$ et COF-316$_M$ ont montré une correspondance exacte, ce qui valide l'efficacité de la synthèse assistée par micro-ondes. Comme le montre la figure 0.3c, les pics associés aux nanofeuillets de $BiVO_4$ confirment leur phase monoclinique pure et leur haut degré de cristallinité[23]. Le profil de XRD du nanocomposite 2D/2D COF-316$_M$/$BiVO_4$ (présenté dans la figure 0.3d) affiche des pics de diffraction distincts pour les deux nanomatériaux, fournissant ainsi des preuves de l'incorporation réussie des nanofeuillets de $BiVO_4$ et du COF-316$_M$ à la surface l'un de l'autre sans altérer leurs structures cristallines. Les profils de diffraction de $BiVO_4$ et de COF-316$_M$/$BiVO_4$ présentent des variations dans l'intensité des pics (020) et (040) à 15° et 31°, respectivement, ce qui indique un changement dépendant de la quantité. Cette observation suggère un alignement parallèle préférentiel entre les plans {010} des nanofeuillets de $BiVO_4$ et le substrat sans aucun changement associé dans la phase ou la composition du matériau[16], [23].

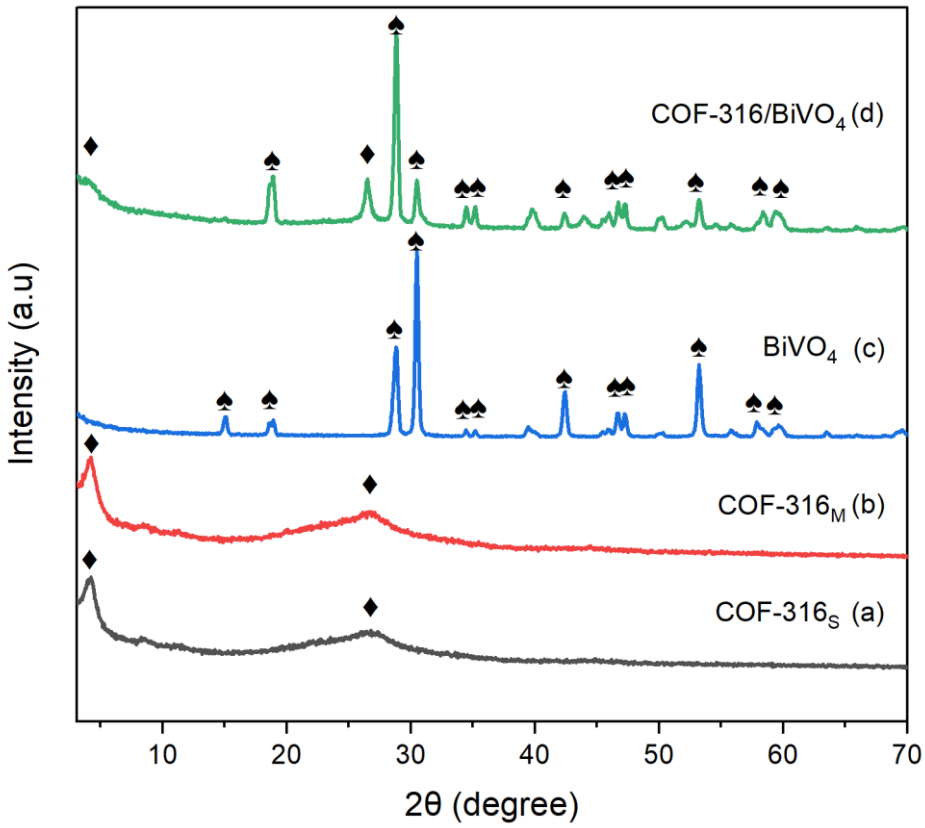


Figure 0.3. Profils de diffraction des rayons X (XRD) de (a) COF-316$_S$, (b) COF-316$_M$, (c) $BiVO_4$ et (d) du nanocomposite 2D/2D COF-316$_M$/$BiVO_4$.

Pour confirmer la composition chimique et les groupes fonctionnels du HTTP (bloc de construction), TFPN, COF-316$_S$, COF-316$_M$, $BiVO_4$ et COF-316$_M$/$BiVO_4$, la spectroscopie infrarouge à transformée de Fourier (FTIR) a été réalisée. Les résultats présentés dans la figure 0.4a-b ont montré les modes d'élongation asymétrique et symétrique caractéristiques du C-O dioxinique, observés dans les échantillons COF-316$_S$ et COF-316$_M$, à 1240 à 1262 et 1008 à 1020 $cm^{-1}$, respectivement[24]. Cette observation sert de preuve de la formation de la liaison dioxine dans la structure du COF-316$_M$. Parallèlement, la disparition de -OH (~3300 $cm^{-1}$) dans le HTTP a fourni des preuves supplémentaires de la formation de la liaison[25]. De plus, les résultats indiquent la présence de groupes fonctionnels -CN à ~2250 $cm^{-1}$ dans COF-316$_S$, COF-316$_M$ et COF-316$_M$/$BiVO_4$ qui peuvent potentiellement faciliter les réactions de réduction

photocatalytique du $CO_2$[11], [12]. Le spectre FTIR du nanocomposite 2D/2D COF-316$_M$/$BiVO_4$ a montré les pics d'absorption des composants COF-316$_M$ et $BiVO_4$. Le pic à 750 $cm^{-1}$ a été attribué à v1($VO_4$) du $BiVO_4$ monoclinique[26]. Ces résultats ont confirmé l'incorporation réussie des nanofeuillets de $BiVO_4$ à la surface du COF-316$_M$. Les résultats FT-IR ont soutenu la synthèse réussie de COF-316$_S$, COF-316$_M$, $BiVO_4$ et 2D/2D COF-316$_M$/$BiVO_4$.

Les mesures de spectroscopie photoélectronique à rayon X (XPS) ont été réalisées pour obtenir une meilleure compréhension de la composition élémentaire et de l'environnement chimique des éléments constituant le nanocomposite COF-316$_M$/$BiVO_4$. Le spectre de l'enquête complète de COF-316$_M$/$BiVO_4$ (figure 0.4c) a révélé la présence de C, O, N, Bi, V et F dans la structure. La composition élémentaire obtenue à partir du spectre XPS pour COF-316$_M$/$BiVO_4$ est résumée dans le tableau 1.

| Element | Atomic fraction (%) (XPS) | Atomic fraction (%) (EDX) |
|---|---|---|
| C | 71.2 | 70.9 |
| O | 20.4 | 19.9 |
| Bi | 2.3 | 2.6 |
| V | 2.1 | 2.5 |
| N | 3.1 | 3.5 |
| F | 0.9 | 0.6 |

Tableau 0.1. Composition élémentaire de COF-316$_M$/$BiVO_4$ (20% p/p)

La figure 0.4d illustre le spectre C 1s de l'échantillon COF-316$_M$/$BiVO_4$, montrant des pics distincts à 286,1, 284,6, 286.6, and 288,2 eV, attribués respectivement à -C≡N, C-C/C=C, C-O et C-F. Pour le spectre O 1s (figure 0.4e), l'énergie de liaison à 529,9 et 533,8 eV correspond respectivement à l'oxygène du réseau dans la structure de $BiVO_4$ et au C-O dans le framework du COF-316$_M$[16]. Le spectre N 1s a montré un pic distinct de N pyridinique (-C≡N) à 399,48 eV (voir figure 0.4f). Le spectre Bi 4f a affiché des motifs de fractionnement du spin-orbite pour les pics Bi $4f_{5/2}$ et Bi $4f_{7/2}$ (figure 0.4g) à 164,96 et

159,64 eV, respectivement. De plus, la figure 0.4h a montré les valeurs d'énergie de liaison de V $2p_{3/2}$ et V $2p_{1/2}$ dans le COF-$316_M$/$BiVO_4$ à 517,05 et 524,36 eV, respectivement, confirmant la présence de $V^{5+}$ dans le réseau[23]. Une petite quantité de F a également été détectée sous forme de liaison C-F, attribuée aux résidus de liens TFPN dans la structure. Cette légère contamination est couramment rapportée dans la synthèse des COFs liés par dioxane[11], [13]. Le motif XPS C 1s du COF-$316_M$ obtenu par synthèse assistée par micro-ondes a montré une parfaite correspondance avec celui du COF-$316_S$, fournissant ainsi une preuve supplémentaire de la réussite de la synthèse assistée par micro-ondes (voir figure 0.4i) [12], [24].

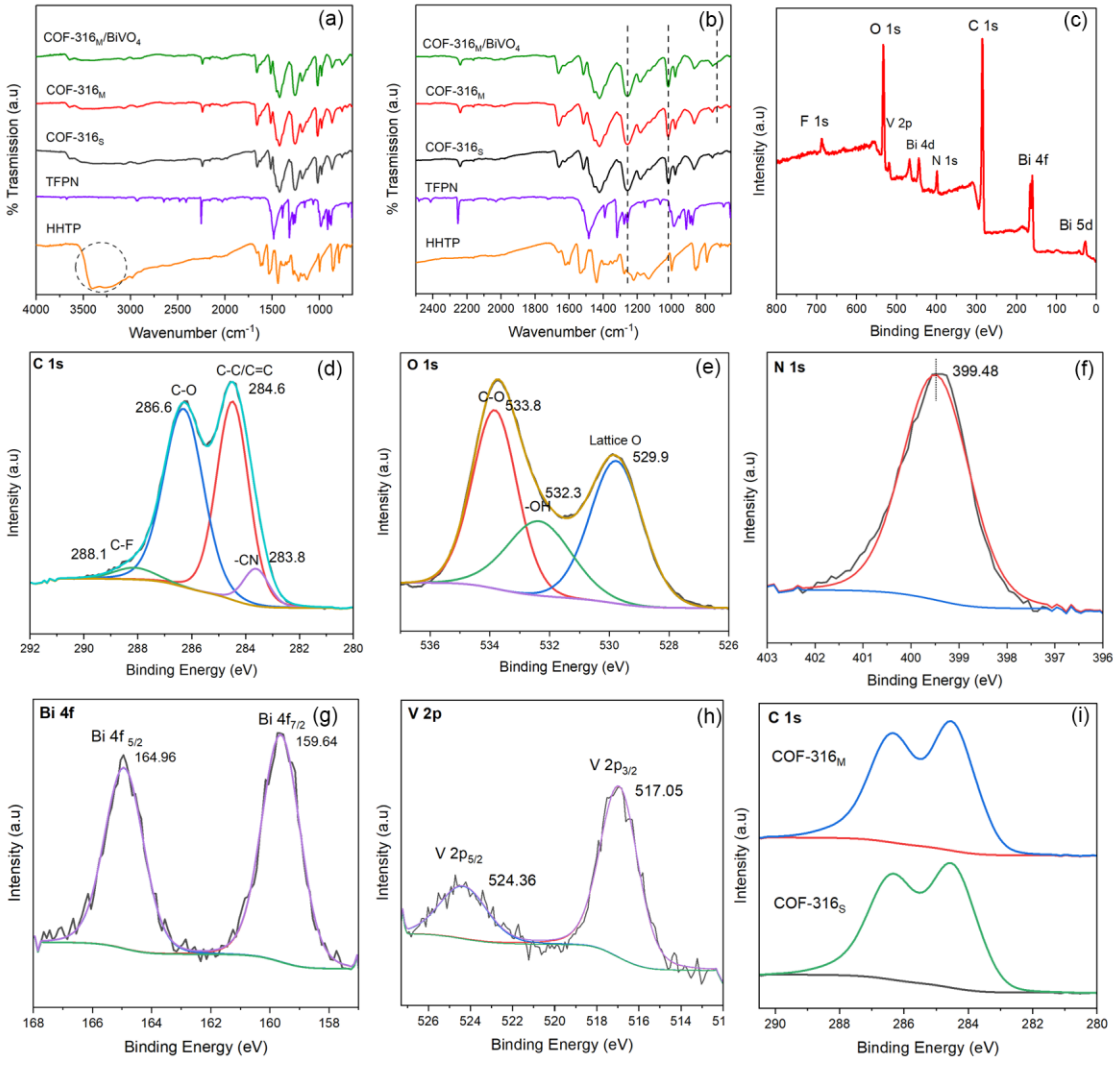


Figure 0.4. Profils FT-IR de (a-b) HTTP, TFPN, COF-$316_S$, COF-$316_M$ et du nanocomposite 2D/2D COF-$316_M$/$BiVO_4$. (c) Spectre complet de spectroscopie de

photoélectrons X (XPS) et spectres de haute résolution de (d) C 1s, (e) O 1s, (f) N 1s, (g) Bi 4f, (h) V 2p de l'échantillon COF-316$_M$/$BiVO_4$. (i) Spectres de haute résolution de C 1s pour les échantillons COF-316$_M$ et COF-316$_S$.

Afin d'étudier la structure et la morphologie des COF-316$_S$, COF-316$_M$, $BiVO_4$ et du nanocomposite 2D/2D COF-316$_M$/$BiVO_4$, la microscopies électroniques en transmission (TEM) et à haute résolution (HRTEM) ont été réalisées. Les images TEM des COF-316$_S$ et COF-316$_M$ ont révélé une remarquable similitude dans leur morphologie, les deux montrant une structure en feuillet uniforme et interconnectée (figure 0.5a-b). Les nanofeuillets de $BiVO_4$ ont montré une taille latérale de 1 à 1,5 micromètres, comme on peut le voir sur la figure 0.5c. L'analyse TEM du nanocomposite 2D/2D COF-316$_M$/$BiVO_4$ a montré la croissance réussie du COF-316$_M$ sur les nanofeuillets de $BiVO_4$ (figure 0.5d). De plus, les images HRTEM de COF-316$_M$/$BiVO_4$ (figure 0.5e-f) ont illustré le contact distinct entre le COF-316$_M$ et le $BiVO_4$, essentiel pour la séparation et la migration des porteurs de charge photoinduits[27]. L'image HRTEM a démontré que les nanofeuillets de $BiVO_4$ présentaient un haut degré de cristallinité, avec des franges de réseau présentant des espacements interplans de 0,260 et 0,255 correspondant respectivement aux plans (200) et (002) du $BiVO_4$ monoclinique[16]. Cependant, en raison de la sensibilité au faisceau électronique des COFs, l'imagerie HRTEM n'a pas réussi à révéler de franges de réseau claires ni de motif de diffraction pour le COF-316$_M$[28]. Les images de cartographie EDX ont fourni des preuves de l'existence des éléments C, O, N, Bi et V dans l'échantillon composite, indiquant ainsi l'absence de toute contamination (figure 0.5g-l). La dispersion des éléments C et N à travers les nanofeuillets de $BiVO_4$ soutient fortement l'intégration de $BiVO_4$ au sein des couches de COF-316$_M$, formant ainsi une structure 2D/2D distincte.

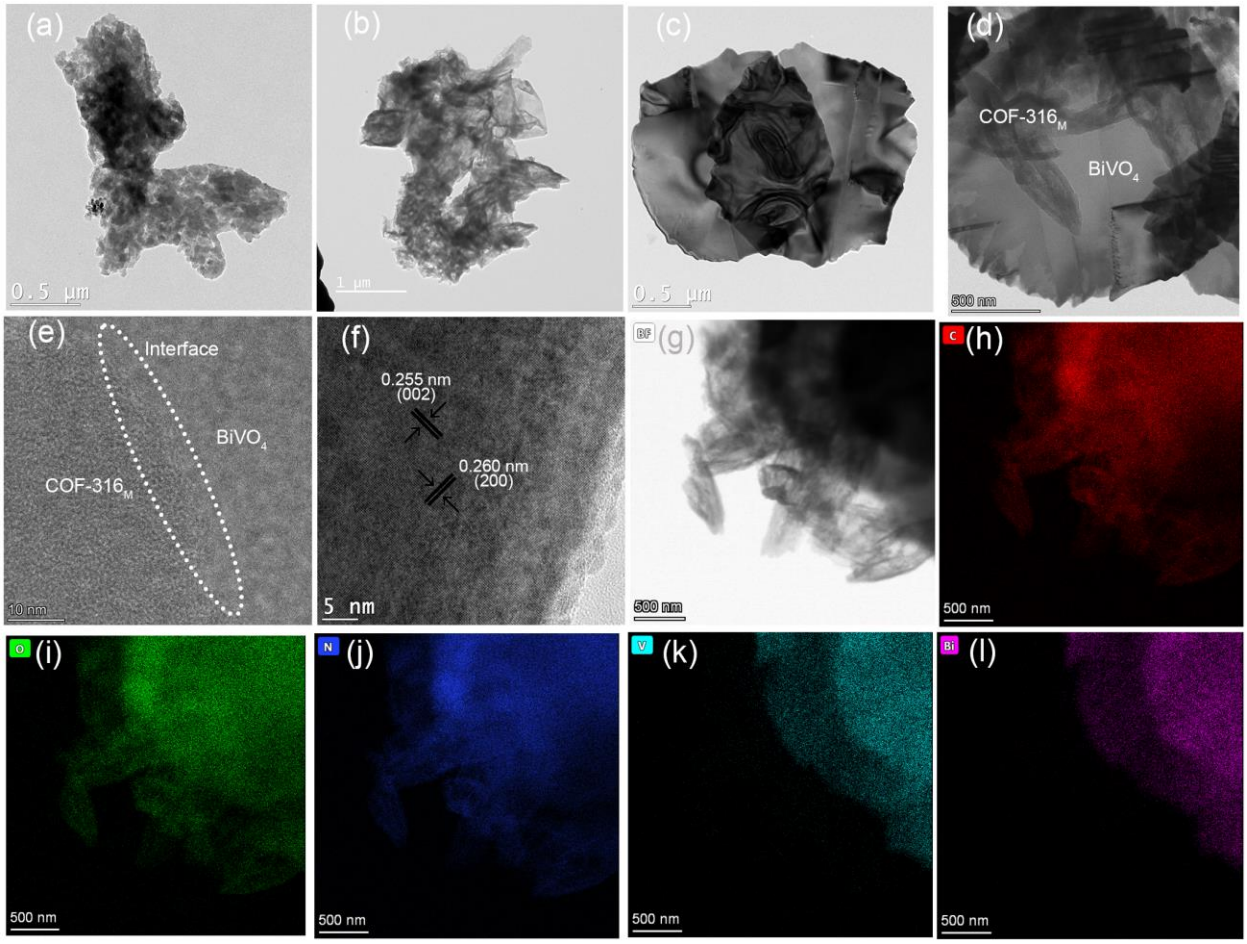


Figure 0.5. Images TEM de (a) COF-316$_S$, (b) COF-316$_M$, (c) $BiVO_4$, (d) nanocomposite 2D/2D COF-316$_M$/$BiVO_4$, (e-f) Images HRTEM de COF-316$_M$/$BiVO_4$, (g-l) Image TEM et images de cartographie EDS des éléments associés de COF-316$_M$/$BiVO_4$. Le cercle blanc dans e met en évidence l'interface entre les deux matériaux.

## 0.3 Analyse des propriétés texturales

Des mesures d'adsorption/désorption d'azote ont été effectuées aux conditions standard de température et de pression (STP) pour évaluer les structures poreuses et les surfaces spécifiques des échantillons COF-316$_S$, COF-316$_M$, $BiVO_4$ et du nanocomposite 2D/2D COF-316$_M$/$BiVO_4$ (Figure 0.6a-d). En utilisant la technique BET, la surface spécifique du COF-316M (592,264 $m^2$/g) était relativement plus élevée que celle du COF-316$_S$ (544,335 $m^2$/g). Les motifs d'isothermes affichent une forme distinctive de Type I[25], [29]. De plus, la surface spécifique du COF-316$_M$/$BiVO_4$ était de 260,291 $m^2$/g, ce qui est relativement plus faible que celle du COF-316$_M$ pur (voir les figures 3.6c-d). Cette différence peut être attribuée à la présence de $BiVO_4$, qui possède une faible surface spécifique d'environ 1,8 $m^2$/g et peut bloquer les micropores du COF-316$_M$. L'analyse de la distribution de taille des pores a été réalisée en utilisant le modèle de théorie fonctionnelle de la densité non locale (NL-DFT). L'analyse des isothermes d'adsorption d'azote a révélé que la distribution de taille des pores des échantillons COF-316 se situe entre environ 0,9 nm et 1,2 nm (voir les figures insérées dans les figures 3.6a-b), en bon accord avec les résultats expérimentaux et théoriques du mode d'empilement éclipsé trouvés dans la littérature[11]–[13], [25], [29]. Les similitudes entre les valeurs expérimentales et prédites de la taille des pores non seulement fournissent une validation robuste de l'analyse, mais servent également de preuve convaincante de l'efficacité de la synthèse assistée par micro-ondes. Cette caractéristique particulière des micropores a également été observée dans le COF-316$_M$/$BiVO_4$.

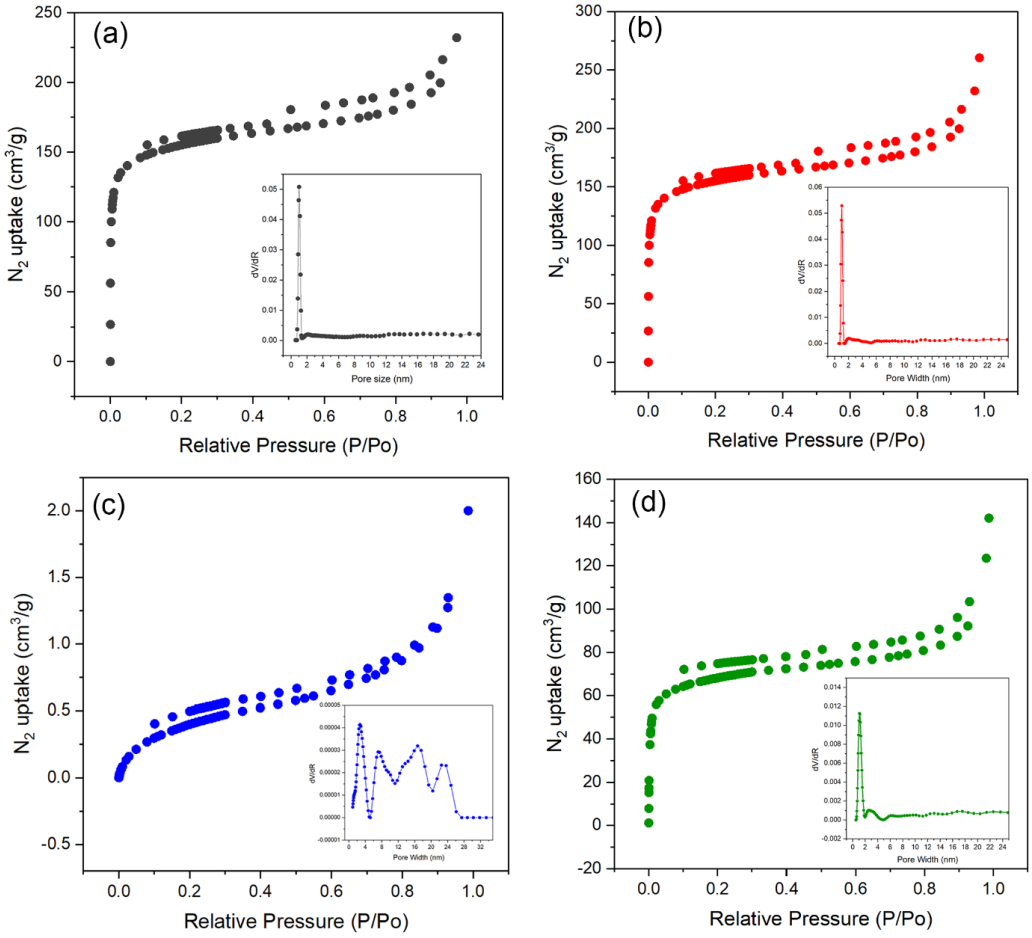


Figure 0.6. Isothermes d'adsorption/désorption d'azote et distribution de la taille des pores (encart) de (a) COF-316$_S$, (b) COF-316$_M$, (c) $BiVO_4$ et (d) du nanocomposite 2D/2D COF-316$_M$/$BiVO_4$.

## 0.4 Propriétés optiques

Les propriétés optiques du COF-316$_M$, de $BiVO_4$ et du nanocomposite 2D/2D COF-316$_M$/$BiVO_4$ ont été étudiées à l'aide d'un spectrophotomètre d'absorption UV-vis en état solide. Comme le montre la figure 0.7a, tous les échantillons présentent une absorption allant du spectre UV jusqu'à environ 475 nm dans le spectre visible. Les propriétés d'absorption du COF-316$_S$ et du COF-316$_M$ étaient presque similaires. Le COF-316$_M$/$BiVO_4$ présentait un léger décalage vers le bleu du bord d'absorption par rapport au COF-316$_M$, cependant, il présentait une absorption améliorée dans le spectre visible au-delà de la réponse optique de $BiVO_4$. Grâce à l'analyse des courbes de Tauc, les bandes interdites optiques mesurées pour le COF-316$_S$, le COF-316$_M$, $BiVO_4$ et le COF-316$_M$/$BiVO_4$ étaient respectivement de 2,11 eV, 2,12 eV, 2,35 eV et 2,28 eV (voir la figure 0.7b). Cela suggère une légère réduction de la bande interdite globale par rapport à $BiVO_4$ seul. Ainsi, la réduction de la bande interdite combinée à une augmentation de l'absorption de la lumière peut favoriser la génération de paires $e^-/h^+$. Par conséquent, le nanocomposite COF-316$_M$/$BiVO_4$ pourrait offrir des performances améliorées et une activité photocatalytique plus élevée dans les réactions de réduction du $CO_2$.

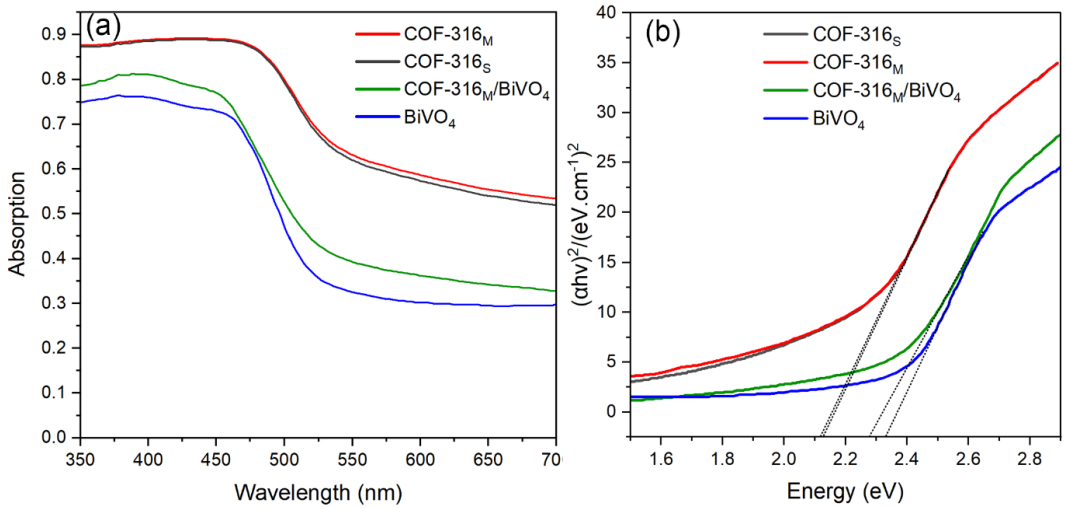


Figure 0.7. (a) Spectres d'absorption et (b) tracés de Tauc du COF-316$_S$, du COF-316$_M$, de $BiVO_4$ et du nanocomposite 2D/2D COF-316$_M$/$BiVO_4$.

## 0.5 Performance de réduction photocatalytique du $CO_2$

La performance photocatalytique du COF-$316_S$, du COF-$316_M$, de $BiVO_4$ et du nanocomposite 2D/2D COF-$316_M$/$BiVO_4$ (20% - 50%) a été étudiée sous lumière visible (>420 nm, 100 mW/$m^2$) et les résultats sont présentés dans la figure 0.8. Le COF-$316_S$ a montré une production de CO d'environ 2,5 µmol $g^{-1}.h^{-1}$, ce qui est en bon accord avec les valeurs rapportées dans la littérature[11], [12]. Notamment, le COF-$316_M$ a montré une plus grande réduction photocatalytique du $CO_2$ avec une production de 3,8 µmol $g^{-1}.h^{-1}$ par rapport à son homologue synthétisé par voie solvothermale (soit environ 150% d'activité accrue). Cela peut être attribué à la surface BET améliorée du COF-$316_M$ obtenue par la méthode de chauffage par micro-ondes par rapport au COF-$316_S$.

Pour vérifier que la source de CO provient de la conversion de $CO_2$ au sein du système et non du COF ou de la contamination par le carbone, trois expériences de contrôle ont été menées. La première consistait à faire passer de l'azote au lieu du $CO_2$, tandis que la deuxième expérience impliquait le passage de $CO_2$ en l'absence de photocatalyseurs. La troisième expérience consistait à faire passer du $CO_2$ en présence de catalyseur mais en l'absence de lumière (conditions d'obscurité). Dans toutes les expériences, aucun produit n'a été observé, fournissant ainsi des preuves de la génération exclusive de CO par conversion du $CO_2$. Le $BiVO_4$ lui-même a produit une petite quantité de CO en raison de sa faible capacité de rédox.

Étant donné que toutes les techniques de caractérisation ont montré les mêmes propriétés pour le COF-$316_S$ et le COF-$316_M$ synthétisés par voie solvothermale et assistée par micro-ondes, et que le COF-$316_M$ avec un temps de synthèse beaucoup plus court a également affiché un taux de production de $CO_2$ plus élevé, seul le COF-$316_M$ a été choisi pour être combiné avec le $BiVO_4$ pour former l'hétérojonction. De plus, la synthèse facile et rapide du COF-$316_M$ a été prise en compte à cet égard. En incorporant du $BiVO_4$ dans la structure du COF, les performances photocatalytiques ont diminué par rapport aux échantillons de COF-$316_S$ et de COF-$316_M$ purs. Le taux de production de CO pour le COF-$316_M$/$BiVO_4$ (20%), (30%), (40%) et (50%) était de 1, 0,8, 0,25, 0,15 µmol $g^{-1}.h^{-1}$.

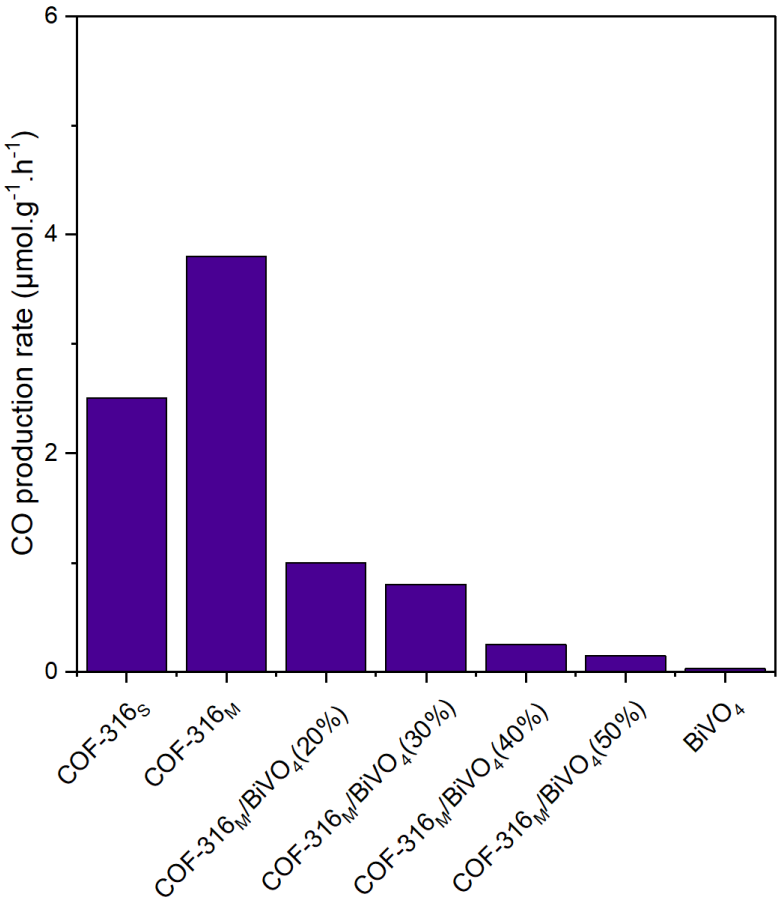


Figure 0.8. Étude comparative de l'activité photocatalytique du COF-316$_S$, du COF-316$_M$, de $BiVO_4$ et du nanocomposite 2D/2D COF-316$_M$/$BiVO_4$ avec différentes proportions de poids sous lumière visible, en utilisant l'eau comme agent de capture des trous sans aucun sensibilisateur.

Nous avons envisagé deux raisons potentielles pour la diminution de l'efficacité. Tout d'abord, nous avons exploré la possibilité qu'un retrait incomplet des ligands organiques à chaîne longue pendant le processus d'échange de ligands de la surface de $BiVO_4$ puisse entraîner des distances interparticules relativement grandes, un contact inefficace et un faible transfert de charges entre les deux composants COF-316$_M$ et $BiVO_4$[30], [31]. Cependant, l'analyse des spectres FTIR avant et après l'échange de ligands a indiqué un retrait presque complet des ligands OLA ou OA avec des vibrations autour de 2300 et 2800-2850 $cm^{-1}$, excluant cette possibilité comme cause de l'efficacité réduite (voir Figure 0.9).

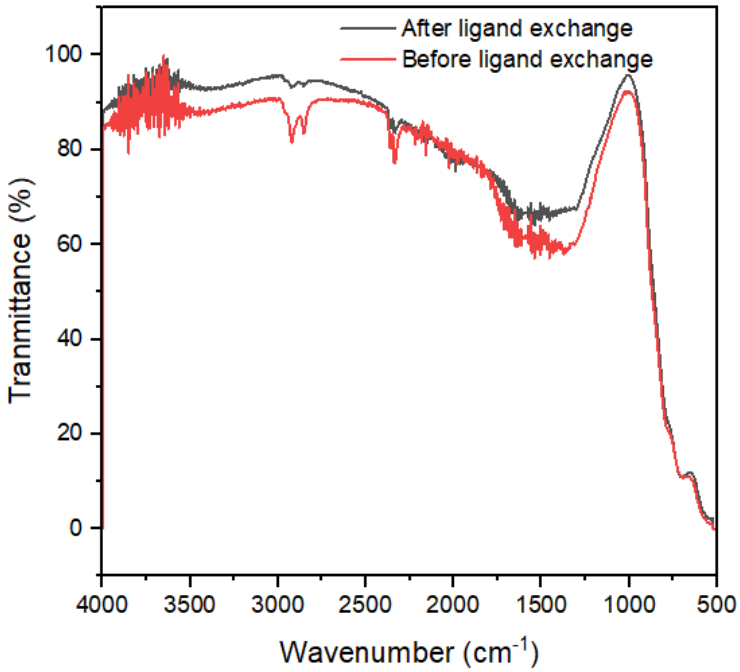


Figure 0.9. Spectres FTIR des nanofeuillets de $BiVO_4$ avant et après le processus d'échange de ligands.

La deuxième raison de la baisse d'efficacité pourrait être explorée en étudiant la voie et le mécanisme de transfert de charges. Pour comprendre en détail le mécanisme de transfert de charges au sein de l'hétérojonction, nous avons effectué une analyse détaillée en comparant les spectres XPS de COF-$316_M$/$BiVO_4$ dans trois conditions différentes : avant l'exposition à la lumière (dans l'obscurité), pendant l'irradiation lumineuse (sous lumière UV) et après (à nouveau dans l'obscurité). Il est important de noter que les changements dans les énergies de liaison d'un élément indiquent directement des variations dans sa densité électronique, ce que l'on peut s'attendre à voir lors de ce type d'analyse[32], [33]. Plus spécifiquement, une diminution ou une augmentation de la densité électronique entraîne respectivement un décalage négatif ou positif de l'énergie de liaison[34]. Cela fait de la spectroscopie XPS une technique puissante pour déterminer avec précision la direction du transfert de charges dans les hétérojonctions, comme COF-$316_M$/$BiVO_4$[35]. Selon la Figure 0.10a, les pics correspondant à Bi $4f_{7/2}$ et Bi $4f_{5/2}$ ont subi un décalage vers des valeurs inférieures d'environ 0,4 eV. Une tendance similaire a été observée pour V $2p_{3/2}$ et V $2p_{1/2}$, où ils ont montré un décalage vers des énergies de liaison négatives (Fig. 0.10b). Ce phénomène

confirme que la densité du nuage électronique près des atomes de Bi et de V de COF-316$_M$/$BiVO_4$ à l'intérieur de l'hétérojonction augmente. Par conséquent, un transfert d'électrons s'effectue du CB de COF-316$_M$ au CB de $BiVO_4$, suivant la voie de transfert de charges de l'hétérojonction de type II (voir Fig. 0.10f). Le décalage opposé observé dans le pic N 1s (Figure 0.10c) confirme davantage ce phénomène. Le retour ultérieur des pics à leur position d'origine après l'irradiation de la lumière UV fournit la preuve que ce décalage est le résultat d'un transfert de charges à l'interface, plutôt que d'un changement dans la composition chimique du matériau sous l'effet de la lumière[33], [36].

Les niveaux d'énergie de bande de valence et de conduction de COF-316$_M$ et de $BiVO_4$ ont été évalués à l'aide de la technique UPS (Fig. 0.10d-e). Dans la région de coupure secondaire, la fonction de travail (W) est déterminée comme W = 21,22 eV (He I) - (coupure - Ef) eV par rapport au vide. Pour analyser le niveau de bande de valence, l'équation EVB (par rapport au vide) = W + valeur d'extrapolation dans la région de bande de valence est utilisée. Pour convertir la valeur du potentiel W et VB à l'échelle NHE, l'équation ENHE = 4,5 eV - Evac est utilisée. Selon les résultats UPS et les graphiques Tauc dans la section 3.4, l'$E_f$, les potentiels $E_{VB}$ et $E_{CB}$ de $BiVO_4$ étaient respectivement de -3,76 eV, -6,9 eV et -4,55 eV par rapport au niveau du vide. De même, les potentiels $E_f$, $E_{VB}$ et $E_{CB}$ de COF-316$_M$ étaient respectivement de -4,58, -6,02 et -3,9 eV par rapport au niveau du vide. Comme discuté dans la section 1.2.5.2, en raison du niveau de Fermi plus élevé de $BiVO_4$ par rapport à COF-316$_M$, le mécanisme de transfert de charges lors du cintrage des bandes et de l'illumination lumineuse suivra le mécanisme de transfert de charges de l'hétérojonction de type II. En raison du potentiel redox pauvre de $BiVO_4$ (CB : +0,05 eV par rapport à NHE), l'aptitude redox des électrons transférés du CB de COF-316$_M$ au CB de $BiVO_4$ diminue considérablement, ce qui entraîne une diminution de la performance photocatalytique dans les composites.

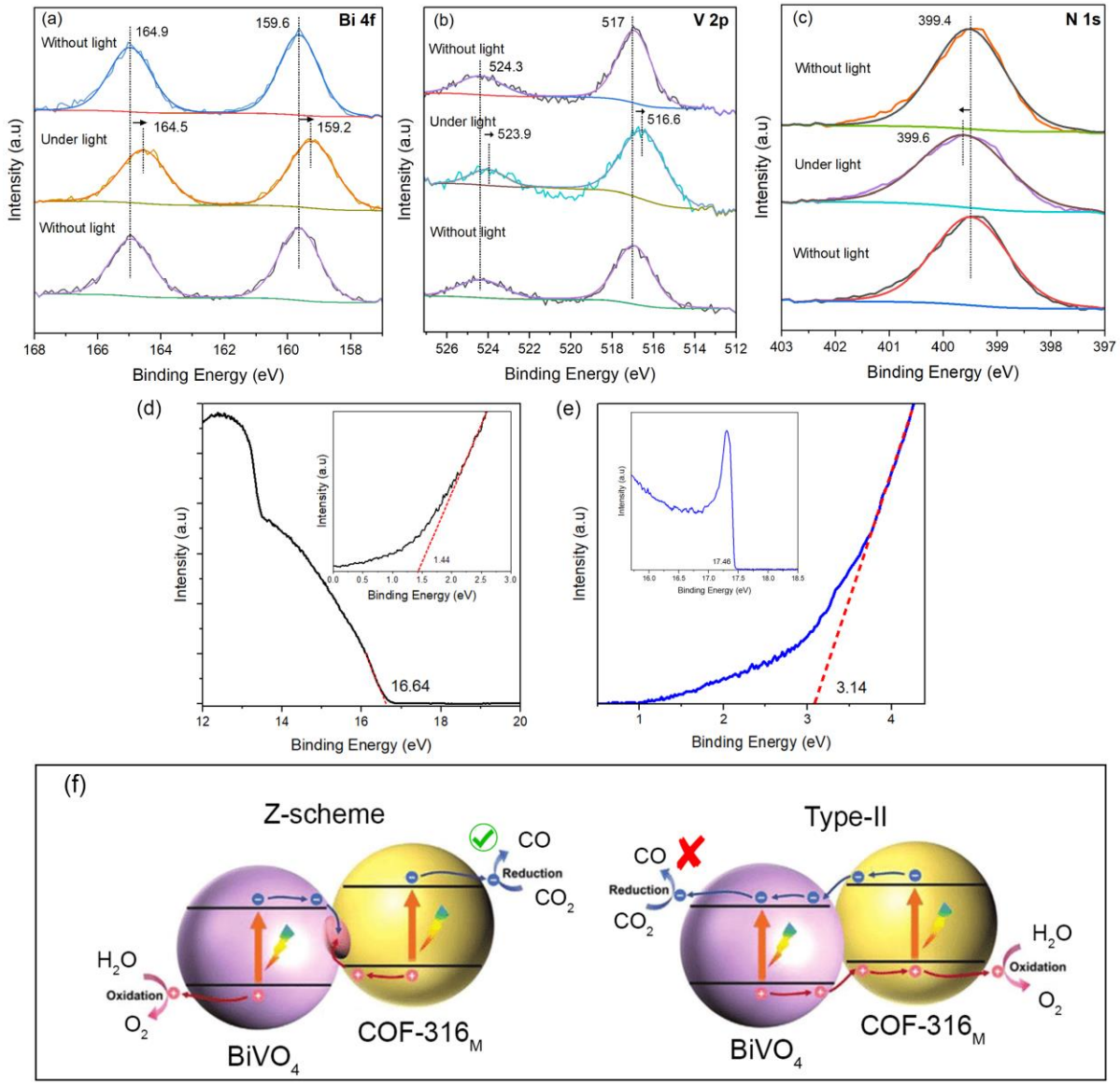


Figure 0.10. Analyse in-situ par XPS de COF-316$_M$/BiVO$_4$ : étude des comportements de (a) Bi 4f, (b) V 2p et (c) N 1s pendant les cycles d'extinction/allumage/extinction sous lumière UV. Spectre UPS de (d) COF-316$_M$ et (e) BiVO$_4$. (f) Mécanisme schématique de transfert de charges à l'interface de COF-316$_M$/BiVO$_4$.

## 0.6 Conclusion et perspectives

COF-316 a été synthétisé par une nouvelle méthode à micro-ondes qui a réduit le temps de réaction de 3 jours à 4 heures à 130 °C. COF-$316_M$ a montré une surface spécifique BET de 592,27 $m^2/g$, dépassant la surface de COF-$316_S$ synthétisé conventionnellement (544,34 $m^2/g$). COF-$316_M$ a montré une plus grande surface spécifique BET par rapport à COF-$316_S$. Des nanofeuillets 2D/2D COF-$316_M$/$BiVO_4$ ont été synthétisés et caractérisés par plusieurs techniques telles que la diffraction des rayons X, la spectroscopie infrarouge à transformée de Fourier, la microscopie électronique en transmission, la microscopie électronique en transmission à haute résolution, la cartographie EDX, la spectroscopie photoélectronique à rayons X et la spectroscopie UV-vis DRS. Les semi-conducteurs individuels ainsi que les composites COF-$316_M$/$BiVO_4$ avec différentes proportions massiques (de 20% à 50% de $BiVO_4$) ont été synthétisés et utilisés dans la réduction photocatalytique du $CO_2$. COF-$316_M$ a démontré un taux de production de CO plus élevé de 3.8 µmol $g^{-1}.h^{-1}$, tandis que COF-$316_S$ a montré un taux plus faible d'environ 2.5 µmol $g^{-1}.h^{-1}$. Les composites ont montré une réduction de l'activité photocatalytique par rapport à COF-$316_M$ et COF-$316_S$ non modifiés. Les résultats de XPS révèlent une diminution de la densité du nuage électronique autour de Bi 4f et V 2p dans COF/$BiVO_4$ lorsque les échantillons sont exposés à la lumière UV. Cela indique un mécanisme de transfert de charge de l'hétérojonction de type II à l'interface, où les électrons sont transférés du CB de COF-316 au CB de $BiVO_4$.

En ce qui concerne ce projet, afin d'améliorer l'activité photocatalytique, nous proposons deux suggestions pour l'avenir : (i) Abaisser le niveau de Fermi de $BiVO_4$ en dessous de celui de COF-316 pourrait potentiellement être une approche viable pour modifier le mécanisme de transfert de charge. Éliminer les lacunes d'oxygène dans le $BiVO_4$ par un processus de recuit pourrait aider à atteindre cet objectif, comme cela a été rapporté dans la littérature [16], [23]. L'optimisation des conditions de recuit pourrait potentiellement conduire à un mécanisme de transfert de charge en forme de Z, (ii) Bien que les échantillons composites n'aient pas montré de performances accrues de photoréduction du $CO_2$ par rapport à COF-$316_M$ et COF-$316_S$ non modifiés, ils présentent toujours des promesses pour des applications alternatives telles que le traitement photocatalytique

des eaux usées ou la production d'hydrogène. Les électrons et trous photo-générés peuvent participer à des réactions hautement productrices de radicaux, ce qui fait de ce photocatalyseur un candidat adapté à la dégradation efficace des polluants organiques dans les eaux usées. La haute surface spécifique de COF-316/$BiVO_4$ peut potentiellement faciliter une adsorption élevée des polluants à la surface du photocatalyseur, ce qui est une étape cruciale en photocatalyse. Une exploration plus approfondie de ces applications pourrait exploiter leur plein potentiel pour résoudre les problèmes environnementaux et contribuer aux technologies d'énergie renouvelable.

La synthèse assistée par micro-ondes des COFs réduit de manière significative les temps de réaction en chauffant efficacement les mélanges réactionnels grâce à des interactions avec les molécules polaires, principalement par rotation de dipôles, ce qui se traduit par un transfert de chaleur amélioré, un transfert d'énergie efficace vers les réactifs porteurs de dipôles, et une distribution uniforme de la température à l'intérieur du récipient de réaction, contribuant tous à améliorer la cinétique de réaction et le contrôle cinétique. Cependant, il convient de noter qu'à l'heure actuelle, il manque des preuves directes et exhaustives démontrant toute modification du mécanisme de synthèse des COFs grâce à l'assistance par micro-ondes. En tant que piste d'exploration future, la réalisation d'une étude mécanistique complète comparant la synthèse par micro-ondes à d'autres méthodes à travers diverses réactions de synthèse des COFs pourrait offrir des informations précieuses sur l'impact potentiel de cette technique.

# Contents

# Chapter 1: Introduction

*1.1. Principles of photocatalytic $CO_2$ reduction and product selectivity*

The immoderate release of $CO_2$ into the atmosphere, has a significant impact on the equilibrium of the carbon cycle in nature, resulting in severe environmental issues, such as the greenhouse effect that causes global warming or melting of the icecaps, among others[9], [37]. In addition, the fossil fuels depletion leads to the need of finding alternates to fulfill our increasing energy requirements in the near future[38], [39]. Thus, looking for sustainable and renewable sources of energy is imperative. Photocatalytic $CO_2$ reduction has appeared as a new sustainable technology that directly converts $CO_2$ in the presence of water and a photocatalyst, into hydrocarbon fuels, utilizing the boundless solar energy as the sole energy source[40].

The carbon present in $CO_2$ molecule, has the highest oxidation state known. It can undergo several reduction reactions to yield various products with different electron and proton counts, including carbon monoxide (CO), formic acid (HCOOH), formaldehyde (HCHO), methanol ($CH_3OH$), or methane ($CH_4$) (See Fig. 1.1) [41], [42]. The primary objective of photocatalytic $CO_2$ reduction reactions is to achieve a high yield of the convenient product. However, undesirable byproducts are usually obtained, consume a valuable number of photogenerated electrons and diminish the output of target products. Additionally, the potential occurrence of the hydrogen evolution reaction (HER) through direct photocatalytic reduction of $H_2O$ presents a competitive process that needs to be addressed[43]. For this reason, it is important to consider inhibiting the hydrogen evolution rate. Moreover, low product selectivity leads to a mixture of multiple products, posing a significant challenge in their separation[44]–[46]. Fine-tuning the product selectivity holds great significance in enhancing the yield of the target product and deepening our understanding on the reaction mechanisms[47], [48]. Finally, it is worth mentioning the key role of $H_2O$ as the proton donor during the reduction process given its essential role in effectively utilizing and consuming the continually produced holes through oxidation reactions[49], [50].

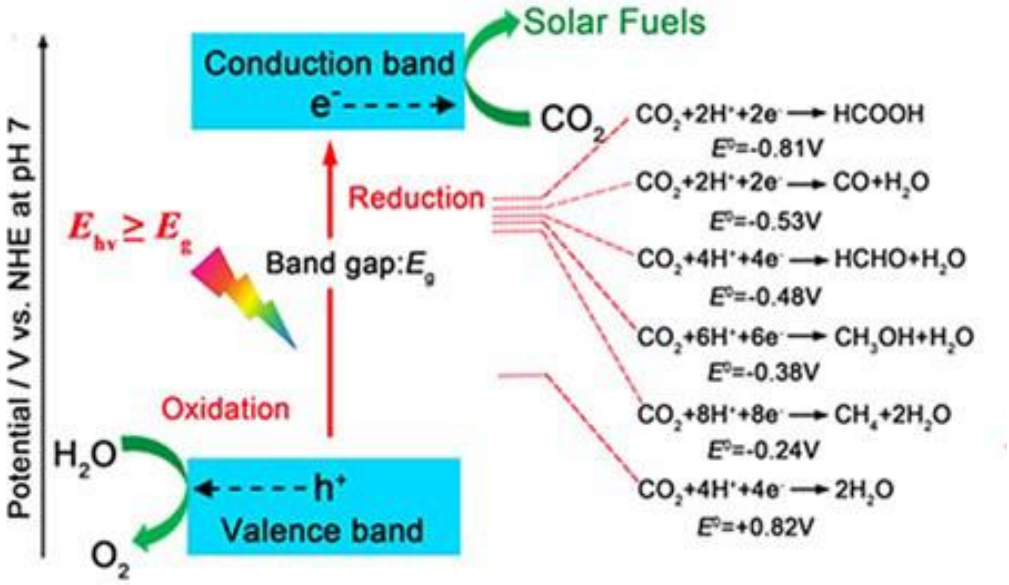


Figure 1.1. Energy diagram of reduction and oxidation reactions involved in photocatalytic $CO_2$ reduction[10]. Copyright 2020, Wiley Online Library.

Photocatalytic $CO_2$ reduction is the process where a photocatalyst harnesses light energy to facilitate the transfer of excited electrons, ultimately converting $CO_2$ into valuable carbon-based products. There are various factors that can impact product selectivity. Fig. 1.2 provides a summary of some factors that affect thermodynamics and kinetics in the product selectivity in photocatalytic $CO_2$ reduction process[41], [49]. The initial critical step involves the absorption of light by the photocatalyst (usually a semiconductor) to generate electrons and holes. Light excitation attributes, including photon energy and light intensity, are key determinants. The photon energy controls whether a semiconductor can absorb photons and excite electrons to a higher energy level, thereby affecting the product selectivity from a thermodynamic perspective[51], [52]. The light intensity determines the number of $e^-/h^+$ produced by photoexcitation, which subsequently influence the reaction rate and product selectivity of reactions involving multiple electrons[40], [52], [53]. The reduction capacity of generated electrons is closely related to the conduction band (CB) position of the semiconductor. Improved separation of electrons and holes can result in a higher surface density of charge carriers on the photocatalyst, which accelerates the rate of multi-electron reduction reactions and leads to higher degrees of reduction, thereby

impacting product selectivity as well [40], [48]. The surface active sites (*e.g.*, co-catalysts, metal centers, etc.) also have an influence on the selectivity of the carbon-based products by providing strong affinity binding sites for $CO_2$ molecules and lowering the energy barrier [3], [9]. Moreover, the adsorption and desorption properties of reactants and intermediates are key dynamic factors influencing product selectivity. Strong adsorption of reactants and facile desorption of the target product can result in high yields of the desired product. Adjusting the adsorption and desorption properties of reactants and intermediates can further optimize the product selectivity in complex photocatalytic $CO_2$ reduction reactions[1], [22].

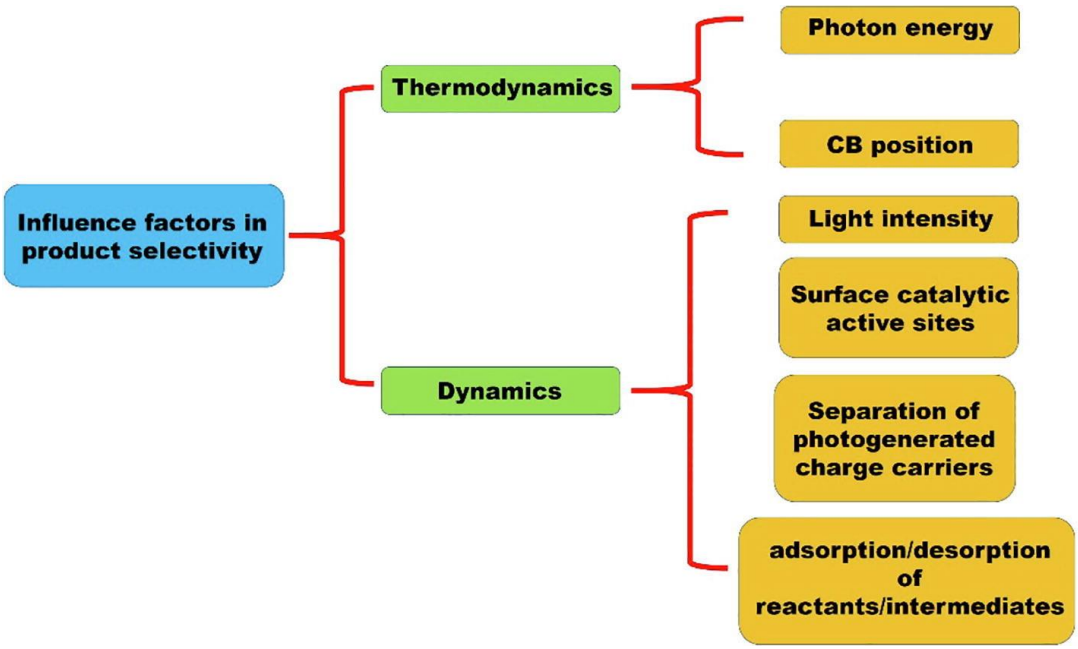


Figure 1.2. Summary of factors that affect thermodynamics and kinetics in product selectivity [41]. Copyright 2020, Elsevier.

The adsorption of $CO_2$ onto the surface of photocatalysts is a crucial step in the whole process. This adsorption interaction leads to the formation of partially negatively charged species, $CO_2^{\delta-}$. The primary adsorbed structures of $CO_2$ on the photocatalyst surface are illustrated in Fig. 1.3, including oxygen coordination, carbon coordination, and mixed coordination[54]. Fig. 1.3A depicts two possible structures involving bidentate binding in the oxygen coordination mode. Fig. 1.3B shows the typical carbon coordination, resulting

in carbonate-like species. The mixed coordination mode is presented in Fig. 1.3C. The different binding modes of $CO_2^{\delta-}$ play a key role in determining the reaction pathways. For instance, monodentate binding, where the carbon atom binds to Lewis base centers on the photocatalysts, favors the formation of the carboxyl radical (•COOH). Bidentate binding, involving two oxygen atoms, promotes the attachment of hydrogen to the carbon of $CO_2^{\delta-}$, leading to the binding of formate anion in the bidentate mode on the photocatalyst surface[54], [55]. The presence of different intermediates significantly impacts the reaction pathways and consequently alters the product selectivity[53], [56].

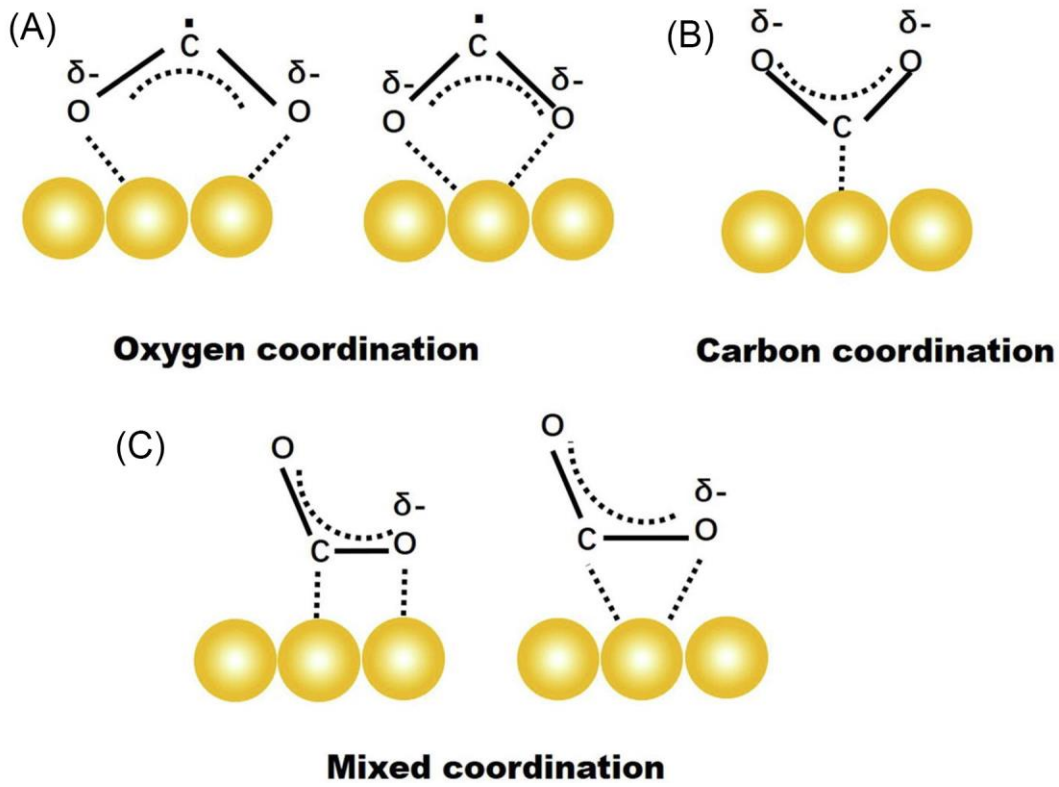


Figure 1.3. $CO_2$ adsorption modes that can occur on the surface of photocatalysts[54]. Copyright 2016, Royal Society of Chemistry.

Competing reactions occur not only between the reduction of $H_2O$ and $CO_2$ but also among different $CO_2$ reduction products arising from distinct reaction pathways[48], [53]. Assessing product selectivity is essential for comprehending the mechanism of these reaction pathways. Accurate measurement of product composition and content serves as the foundation for calculating product selectivity. Typically, gas phase products can be

quantitatively detected using gas chromatography (GC) equipped with a thermal conductivity detector (TCD) and a hydrogen flame ionization detector (FID) [57], [58]. Products in liquid state at room temperature and pressure, such as alcohols, can also be detected by gas chromatography through techniques such as heating gasification or direct liquid injection[59]. Furthermore, mass spectrometry (MS) can also be used to acquire information about the qualitative analysis of products. The combination of GC and MS (GC-MS) enables both qualitative and quantitative analysis of various products in the same analysis[60]. MS isotope labeling experiments can be carried out, aiding to determine the origin of the carbon source in the products (from the $CO_2$ reactant or from organic compounds or impurities adsorbed on the photocatalyst surface)[41], [61]. For example, in the case of carbon-containing photocatalysts like g-$C_3N_4$ and graphene, the actual source of carbon requires a more careful analysis because some organic carbon-containing compounds adsorbed on the photocatalyst surface may participate in the reactions[41]. Consequently, for these materials, their stability also influences the carbon source. Possible decomposition of the carbon-containing photocatalyst can result in carbon contamination in the products. Depending on the system, numerous control experiments should be conducted to determine whether a target product is present in the absence of $CO_2$ or $H_2O$ such as dark control (no light source), no-photocatalyst control and no-reactant control (without $CO_2$). Isotopically labeled hydrogen and carbon experiments serve as powerful tools for identifying the hydrogen and carbon sources in the products[62], [63].

Various semiconductors, including $TiO_2$[64], CdS[65], $MoS_2$[66], and $Cu_2O$[67] have been identified as active photocatalysts for $CO_2$ reduction. However, despite the promising potential, most materials exhibit low photocatalytic efficiency in $CO_2$ reduction and limited selectivity for desired products[68], [69]. A major drawback is that most of these photocatalysts are only active in the ultraviolet (UV) region, limiting their efficacy. Furthermore, the relatively low surface area as well as poor tunability inherent in mesoporous materials impede their broader effectiveness in the realm of photocatalytic processes. [57], [70]. The use of polymeric semiconductors in photocatalysis has gained significant attention in recent years, with researchers exploring materials such as graphitic carbon nitride (g-$C_3N_4$)[71], [72], conjugated polymers[73], [74], and covalent organic

frameworks[75], [76]. These materials have shown superior characteristics compared to non-polymeric and inorganic semiconductors, including enhanced tunability, higher light absorption, superior stability, increased surface area, and enhanced $CO_2$ adsorption ability[1], [8], [77].

For abovementioned reasons, in the upcoming section, we will focus on covalent organic frameworks (COFs) as a promising alternate for $CO_2$ reduction. COFs represent a distinct category of materials characterized by well-organized arrangements of organic building blocks interconnected through covalent bonds[68], [78]. They exhibit remarkable properties such as high porosity, tunable chemical composition, and extensive surface areas[79], [80]. We will delve into their structure and properties, the influence of linkers on the structure's stability and their synthesis methods. We will elaborate on recent progress in developing metal-free COFs as well as two strategies employed to enhance COFs' photocatalytic performance, including metalation and design of heterojunctions.

### *1.2. COFs and their application in photocatalytic $CO_2$ reduction*

#### *1.2.1. Structure and general properties of COFs*

COFs are highly porous polymers characterized by well-defined 2D or 3D crystalline structures. These structures consist of low dense elements such as O, C, B, and N, which are connected by covalent bonds[81] (Fig. 1.4). In 2D COFs, atomic layers are more stacked together through π–π interactions[82], [83]. In contrast, 3D COFs are covalently connected and arranged in extended networks[84]. COFs offer structural designability, allowing for the precise incorporation of organic sub-units at the atomic level into a predetermined skeleton[85]. They possess desirable properties such as low density, high surface area, high thermal stability, and tunable pore sizes and structures[86]. Additionally, COFs show a moderate bandgap and feature an extended π-conjugated electronic network, enabling their responsiveness to visible light[69]. Bandgap engineering can be achieved by carefully selecting monomers to alter the degree of conjugation or introducing diverse functional groups. The distinctive physical and chemical properties of COFs, including modularity, crystallinity, porosity, and stability, make them promising semiconductor photocatalysts[69].

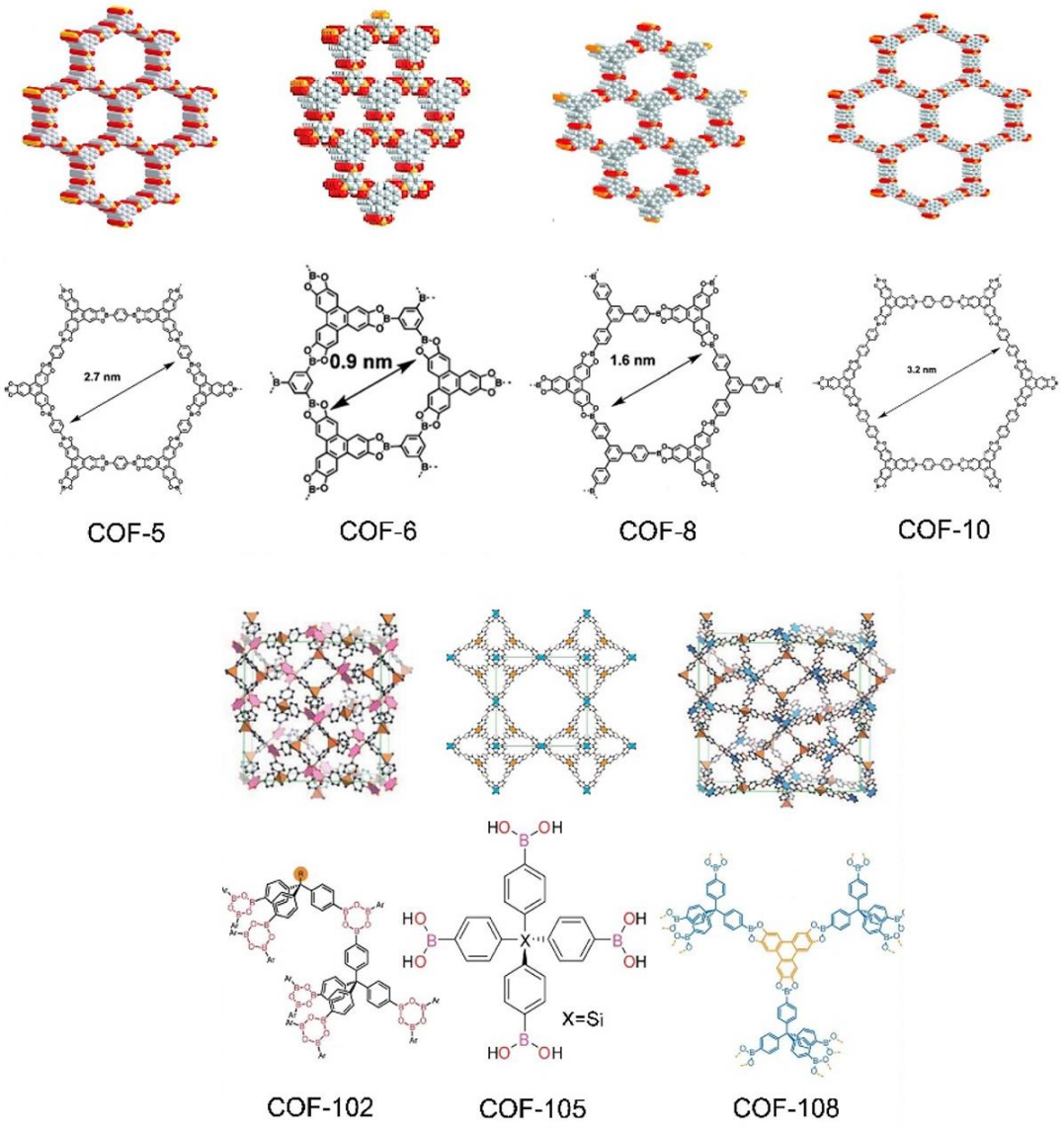


Figure 1.4. Structure of some COFs [87]. Copyright 2019, Elsevier.

The advantages of COFs over other catalysts lie in their ability to efficiently separate photogenerated charges through columnar π arrays, and their inherent pores that facilitate the transport and transformation of matter[88], [89]. In most cases, COFs display excellent stability, outperforming most metal organic frameworks (MOFs), even in organic solvents and under harsh reductive, oxidative ,acidic or basic conditions[90], [91]. This exceptional stability is attributed to the robust covalent bonds within COFs compared to

the coordinate bonds in MOFs. In contrast to other polymeric photocatalysts like graphitic carbon nitride (g-$C_3N_4$), COFs offer tunable structure, pore structure, and numerous catalytic sites, promoting high efficiency and selectivity in $CO_2$ reduction [92]. However, it is important to note that not all COFs exhibit high stability. Their stability is significantly influenced by the type of linkage, highlighting its importance in determining their overall stability.

### *1.2.2 Influence of linkages on COFs' stability*

The inception of COFs can be traced back to the early 2000s when the pioneering work of Yaghi and his team led to the synthesis of the first 2D COFs [93] . These COFs, known as COF-1 and COF-5, were formed through self-condensation or co-condensation reactions involving benzenediboronic acid (BDBA) and hexahydroxy triphenylene (HHTP), resulting in the formation of boroxine and boronate ester linkages. The incorporation of these linkages provided structural strength to the mentioned COFs, enabling flexibility in the selection of building blocks and the engineering of pore sizes.

Despite their rigidity, boronate ester and boroxine linkages have limited hydrolytic stability posing challenges for photochemical $CO_2$ conversion and water splitting[2]. Also, COFs with azodioxy [94] linkages are likely to be less stable under harsh conditions compared to COFs based on triazine [95], β-ketoenamine [76], imide [96], dioxin [24], [97], hydrazine [96], and amide [98] linkages. To address this issue, there has been a demand for new linkages with improved stability. One such class of linkages is imine-based linkages. The first publication containing imine-based COFs was done by Yaghi *et al*. The materials was synthetized through the condensation of amine and aldehyde linking units[99]. It was found out that the reversible nature of bond formations in COFs allows for error correction during the synthesis process in general[3]. This leads to the formation of crystalline products, which contributes to their superior properties compared to amorphous polymers[77]. However, COFs formed through reversible linkages generally show lower stability compared to those formed through irreversible reactions[93]. For reference, some of the most common linkages are shown in Fig. 1.5.

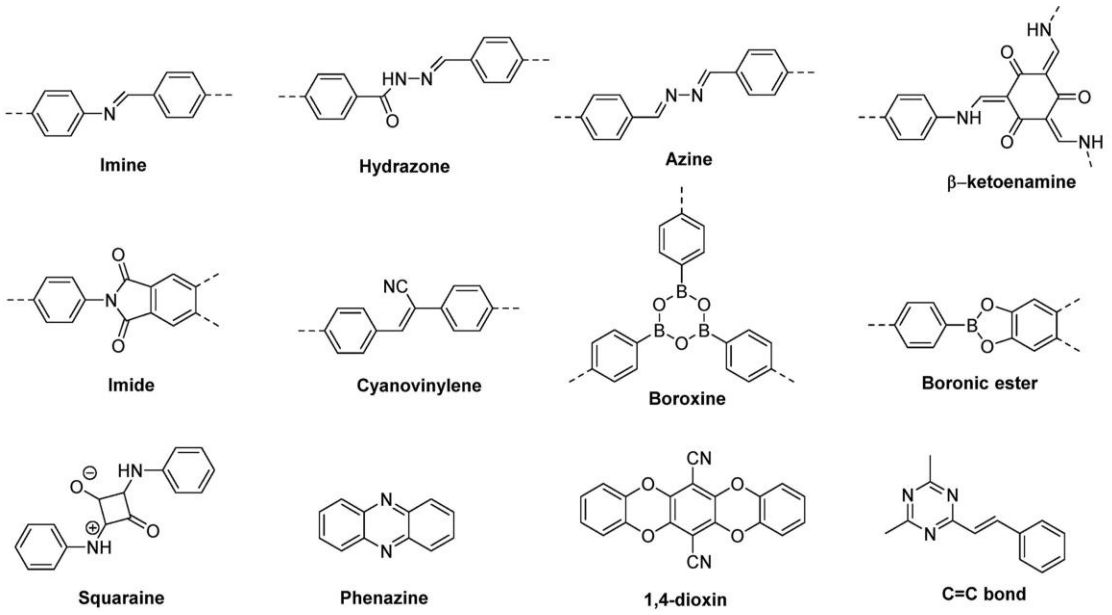


Figure 1.5. Some of the typical linkages used in the synthesis of COFs.

### *1.2.3. Synthesis of COFs*

The vast majority of COFs have been synthetized through solvothermal methods. Solvothermal synthesis is a technique that yields COFs with high crystallinity, minimal defects, favorable orientation, and uniform particle size under mild conditions[3], [8], [100]. In this approach, the necessary monomers, solvent, and catalyst are placed in a sealed container such as a tube, ampule, glass bottle, or teflon-lined stainless autoclave[101]. The container is typically heated above the boiling point of the solvent. Generally, in solvothermal synthesis, the reaction takes place in a non-aqueous organic solvent[102], [103]. The choice of an appropriate solvent is crucial for the synthesis because it directly affects the reaction kinetics, overall efficiency, and desired chemical reactions[104], [105]. By providing optimal conditions for dissolution and ensuring compatibility with COF precursors, the chosen solvent plays a crucial role in preventing undesired side reactions or degradation[106]. Commonly used solvents for COF synthesis include dimethyl sulfoxide [107], acetonitrile [108], dimethylformamide (DMF) [75], or mixed solvents such as mesitylene/dioxane, o-dichlorobenzene/dimethylacetamide [109], 1,4-dioxane/AcOH [99], dioxane/methanol

[110], among others. Mixed solvents like mesitylene/dioxane (1:1, v/v), o-dichlorobenzene/DMAc or dioxane/methanol, are typically employed for the synthesis of boronate-linked or hydrazone-linked COFs [111], [112], while DMSO, 1,4-dioxane [113], and mixed solvents like dioxane/AcOH, EtOH/mesitylene/AcOH [114], o-dichlorobenzene/n-butanol [115], etc., are used for imine-linked COF synthesis [116]. In addition to solvent selection, it is important to consider if the monomers are prone to oxidation, the reaction must take place under an inert atmosphere, such as argon or nitrogen [22], [117]. In spite of its ability to produce a wide range of COFs, the solvothermal method is hampered by drawbacks such as low yield rate and long reaction times, typically ranging from 3 to 7 days[21].

The utilization of microwave synthesis has been recently adopted in organic synthesis due to its ability to accelerate reaction times and provide facile control over conventional solvothermal methods. Microwave irradiation effectively generates the necessary energy by coupling microwave energy with substances such as solvents and reactants, compensating for the slower energy transfer inherent in traditional external heating methods[21], [65], [118]. While many COFs synthesized using the microwave method exhibit similar properties to those synthesized via the solvothermal route, the microwave approach enables the accelerated formation of covalent bonds. For instance, β-ketoenamine-linked TpPa−COF derived from 1,3,5-triformylphloroglucinol (Tp) and p-phenylenediamine (Pa) can be successfully synthetized within just 1 hour under microwave treatment[118]. Another of its significant advantages is the ability to achieve the desired products with improved crystallinity and larger surface areas. For example, crystalline COF-5, obtained from 1,4-benzenediboronic acid (BDBA) and HHTP, can be synthesized in just 20 minutes under microwave irradiation at 100℃, whereas solvothermal synthesis would typically require 72 hours. Furthermore, the surface area of COF-5 significantly improves from 902 $m^2/g$ to 2020 $m^2/g$ by employing microwave heating, surpassing the surface area of the initially reported COF-5 (1591 $m^2/g$) synthesized via solvothermal technique[29]. Additionally, the use of microwave irradiation allows for COFs synthesis at lower reaction temperatures[29]. In 2012, CTFs were prepared using the microwave method, allowing for room-temperature conditions instead of the conventional approach at approximately 120°C [119].

*1.2.4 COFs in $CO_2$ photoreduction*

COFs have been used as visible-light-driven photocatalysts for $CO_2$ conversion for several years[3], [7], [77]. They were firstly introduced in this field by Baeg *et al.* , who fabricated a CTF through the condensation reaction of 3,4,9,10-perylenetetracarboxylic diimide and cyanuric chloride [120]. This cost-efficient synthesis resulted in a flexible film of CTF with a suitable bandgap energy (2.05 eV) for artificial photoreduction of $CO_2$. CTF was able to convert $CO_2$ into HCOOH with a production yield of $881.3 \times 10^3$ μmol $g^{-1}$ $h^{-1}$. The high photocatalytic activity of CTF was attributed to two factors: enhanced visible-light harvesting efficiency compared to the monomer and a highly conjugated structure characterized by highly ordered π-electron channels, which facilitated photoexcited charge transfer.

To obtain highly crystalline COFs based on triazine units, Kong *et al*. incorporated triazine linkers into an imine-linked COF called CT-COF (Fig. 1.6), which contained donor (carbazole unit) and acceptor (triazine unit) moieties within the framework[121]. Under visible-light irradiation, a gas-phase reaction between $CO_2$ and water yielded CO as the major product (with a production rate of 102.7 μmol $g^{-1}$ $h^{-1}$) and $O_2$ in relatively close stoichiometry, even in the absence of any cocatalysts. In-situ Fourier-transform infrared spectroscopy (FT-IR) revealed that both $CO_2$ and $H_2O$ adsorbed on the CT-COF surface, produced COOH* species as intermediates. The formation of a donor-acceptor junction in CT-COF provided sufficient HOMO-LUMO (HOMO: highest occupied molecular orbital, LUMO: lowest unoccupied molecular orbital) separation for efficient $e^-/h^+$ pair generation and facilitated intramolecular charge transfer. Additionally, the presence of nitrogen atoms in the triazine rings provided active sites that enhanced the polarizability of $CO_2$ through dipole-quadrupole interactions, further stabilizing the delocalization of negative charge and prolonging the lifetime of photogenerated electrons[14], [27]. Fig. 1.6 illustrates the proposed pathway for the photoreduction of $CO_2$ through photoinduced electron transfer. This study demonstrated the effectiveness of heteroatom-based COFs as metal-free photocatalysts for $CO_2$ reduction. The presence of a donor-acceptor junction and the active sites provided by the triazine rings contributed to enhanced visible-light harvesting, efficient charge separation, and favorable $CO_2$ activation[121].

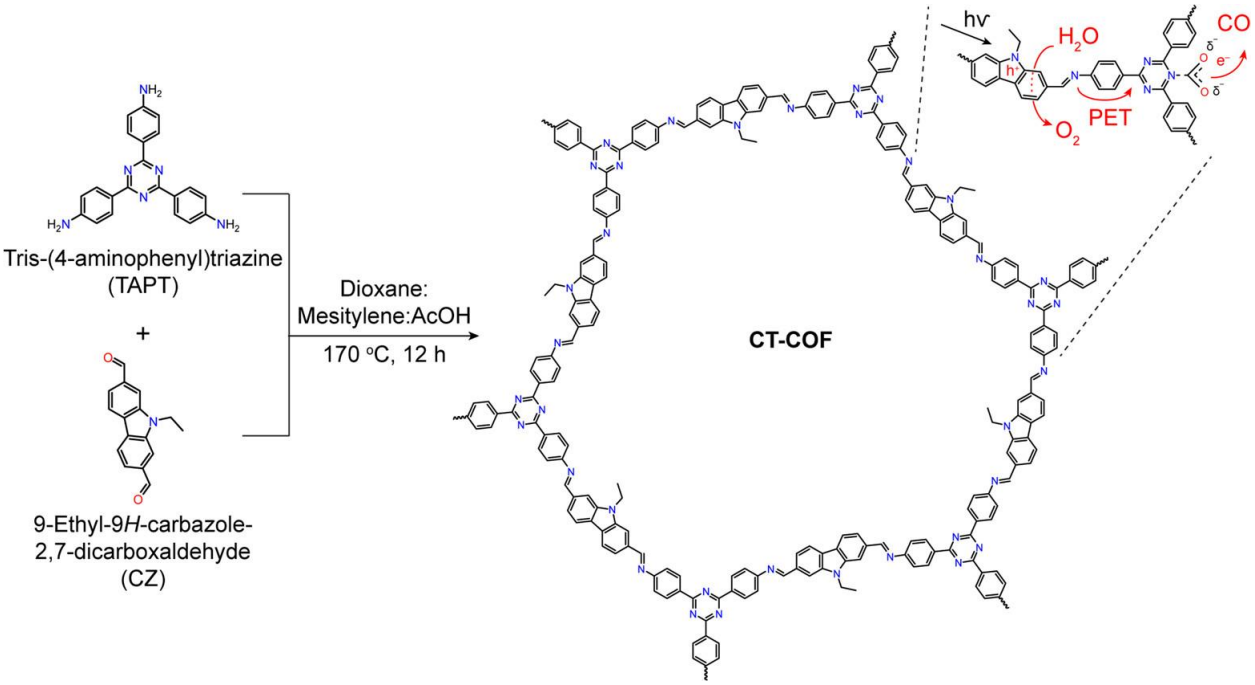


Figure 1.6. Synthetic procedure of CT-COF and the proposed pathway in the photoreduction of $CO_2$ through photoinduced electron transfer[121]. Copyright 2020, Chemistry Europe.

### *1.2.5 Strategies to improve COFs performance in $CO_2$ reduction*

This section will provide an explanation of how COFs can be modified to enhance their performance in CO2 photoreduction. We will explore two primary strategies in detail: metalation, which involves incorporating metals into the COF structure, and forming heterojunctions, where COFs are combined with other materials to create interfaces with unique properties.

#### *1.2.5.1 Metalation of COFs*

The incorporation of metal centers into COF frameworks serves two main important functions: (1) to act as active catalytic sites and (2) to provide strong affinity binding sites for $CO_2$. Bi *et al*. [122] conducted a study where $Co_3O_4$ was encapsulated within CTF to form Co/CTF-1, which can be reduced to Co(I) species that interact with $CO_2$ to facilitate $CO_2$ photoreduction. However, the inclusion of $Co_3O_4$ in the CTF structure can lead to aggregation and deactivation of the active sites. Moreover, the nonuniform distribution of

Co sites negatively impacts the photocatalytic performance of Co/CTF-1, as evidenced by the low production rate of CO (50 μmol $g^{-1}$ $h^{-1}$). However, the photocatalytic activity for CTF and $Co_3O_4$ were reported to be 44 times and 12 times lower than optimized Co/CTF-1. Recently, CTF-1 has been synthetized incorporating $CsPbBr_3$ perovskite into its structure. The resulting composite also exhibited a low CO generation rate of 48.2 μmol $g^{-1}$ $h^{-1}$.

The functionalization of COFs with active metal sites often involves the use of bipyridine ligands, porphyrin units, and layer-layer interactions[123]. Among these, bipyridine-functionalized COFs have been extensively employed, as they allow the direct coordination of metal complexes to the nitrogen present in their molecular structure[124]. As mentioned earlier, CTFs exhibited high activity for $CO_2$ photoreduction even without catalytic metal sites[125]. They can serve as synergistic platforms for the chemical incorporation of active metal complexes and the resulting materials could display enhanced photoreduction performance. An example of it was published by Xu *et al.* [126]. They reported CTF-based material denoted as CTF-pyridine, which contain bipyridine-like sites. Those groups served as docking centers for the inclusion of rhenium in the COF structure. The incorporation of $Re(CO)_5Cl$ into CTF-pyridine yielded a photocatalyst named Re-CTF-pyridine, as shown in Fig. 1.7. Under UV-vis light irradiation for 10 hours in the solid-gas phase using TEOA as an electron donor, Re-CTF-pyridine showed high selectivity towards CO, achieving a production rate of 353.06 μmol $g^{-1}$ $h^{-1}$, with minor formation of $CH_4$.

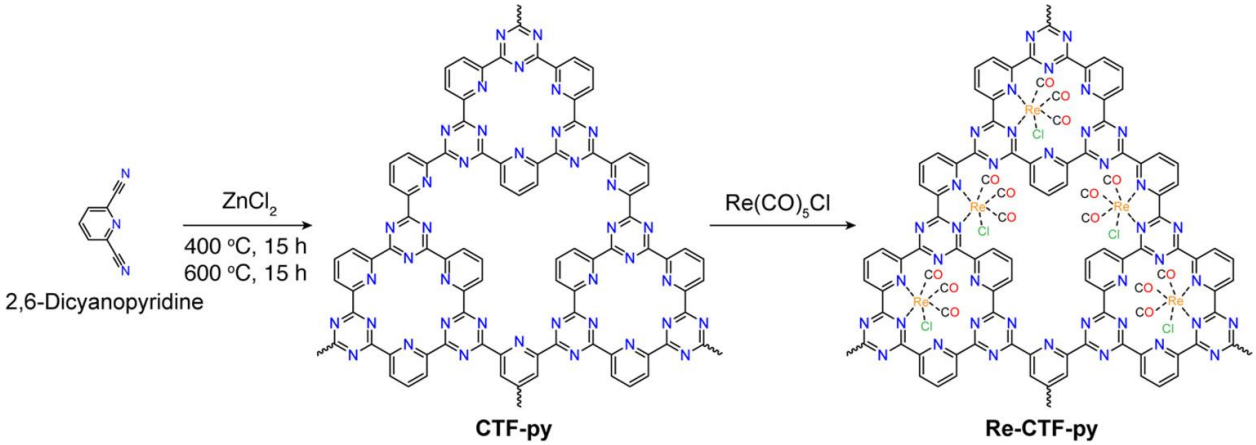

Figure 1.7. Synthetic pathway and chemical structures of Re-CTF and its post-functionalized counterpart, Re-CTF-Py[126]. Copyright 2018, Royal Society of Chemistry.

Adding metal nanoparticles to COFs' framework has been an effective strategy for suppressing charge recombination, thereby enhancing photoactivity[77]. However, bare-metal nanoparticles tend to aggregate during the metalation process. In this regard, COFs with confined pores offer a suitable platform to overcome this challenge. Fan *et al*.[126] recently reported the use of a bipyridine-linked TpBpy COF as a platform for highly dispersing ultrafine Ru NPs for the photoreduction of $CO_2$. The incorporation of 0.7 wt% Ru@TpBpy led to enhanced $CO_2$-to-HCOOH, resulting in the production of 172 μmol $g^{-1}$ $h^{-1}$ after 10 hours of visible-light irradiation.

Another recent study by Lan *et al.* [127] showed the photocatalytic activity of metal-modified tetrathiafulvalene (TTF) and porphyrin-based COFs, denoted as TTCOF-M (where M represents 2H, Zn, Ni, and Cu), for the photoreduction of $CO_2$ under aqueous conditions, without the need for photosensitizers, sacrificial electron donors, or noble-metal cocatalysts[128]. The combination of TTF and porphyrin building units, specifically 5,10,15,20-tetrakis(4-aminophenyl)porphine (TAPP), in TTCOFs were particularly synergistic. TTCOF-Zn possesses an optimal bandgap energy (1.49 eV) and band structure. In addition, its highly conjugated framework (Fig. 1.8) promotes efficient charge transfer and showed a remarkable selectivity of 100% for $CO_2$-to-CO photoreduction. Importantly, this reaction exhibits a CO production yield of 12.33 μmol under aqueous solution, without the requirement of sacrificial agents or cocatalysts. In this study we can see the significance of integrating three essential factors—strong conjugation system, active metal sites, and appropriate band structures—within a COF.

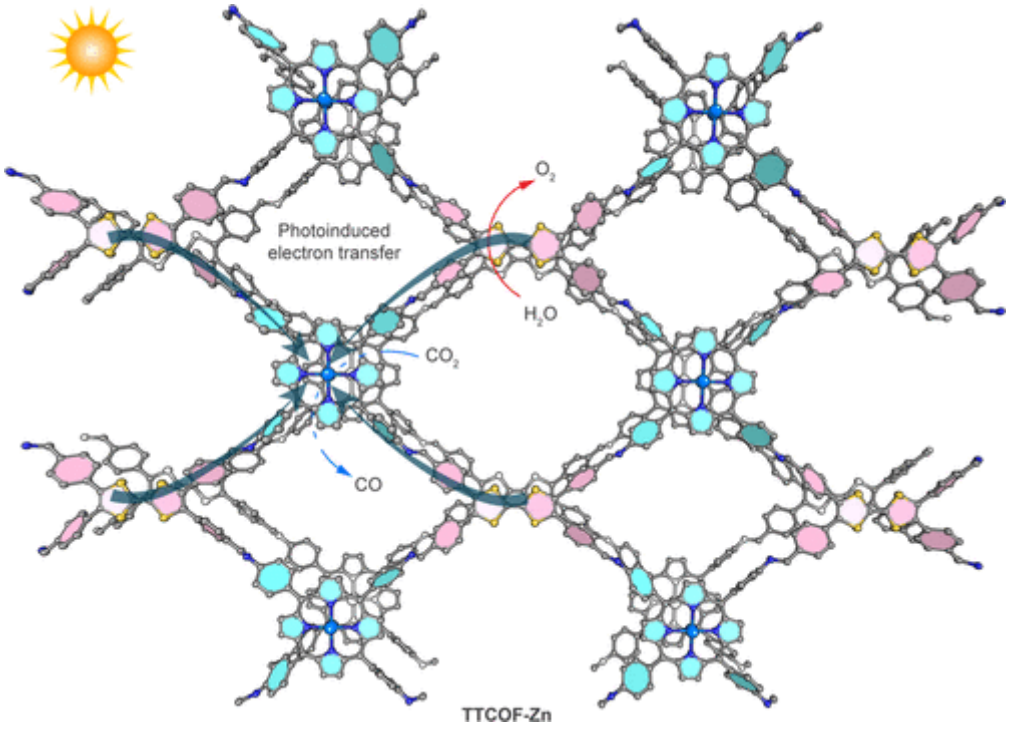


Figure 1.8. Crystal structure of TTCOF-Zn and illustration of the $CO_2$ photoreduction mechanism through the photoinduced electron transfer[128]. Copyright 2020, Wiley-VCH.

*1.2.5.2 Heterojunction composites*

Another approach to enhance the efficiency of photocatalysis involves the combination of COFs with other semiconductors[11], [78], [129]. Composite photocatalysts offer the advantage of significantly improving the efficiency of charge separation and transfer[61]. As shown in Fig. 1.9, heterojunctions can be categorized into different types based on charge transfer route and the energy positions of the conduction band (CB) and valence band (VB): (a) type I (straddling gap), (b) type III (broken gap), (c) type III and (d) Z-scheme [130].

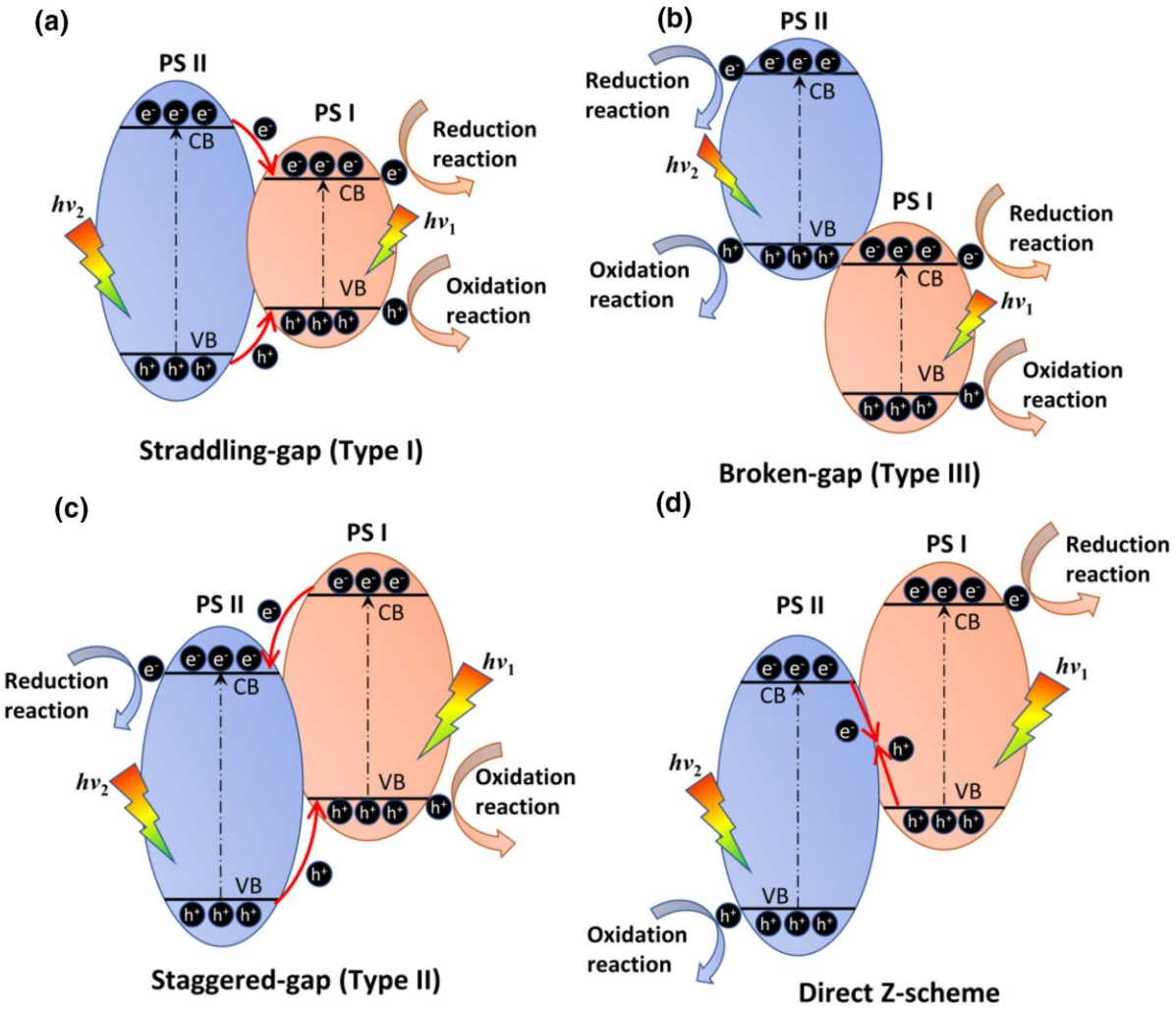


Fig. 1.9. Different types of heterojunctions based on their energy level position[131]. Copyright 2021, Elsevier.

The type II heterojunction promotes favorable charge separation for photocatalytic reactions [132]. In this type of charge transfer, electrons transfer from a material with a more negative CB to one with a more positive CB, while holes move in the opposite direction, from a more positive VB potential to a more negative one (see Fig. 1.9c), physically separating electrons and holes. However, the common type-II heterojunction is found to be less effective in photocatalytic reactions due to the migration of electrons towards a less reducing potential and holes towards a less oxidizing potential, which

results in a decrease in redox ability[130]. There are many examples of type II heterojunctions with two or more semiconductors where the charge separation has contributed to an increase of the photocatalytic activity. Nevertheless, there are situations where the loss of redox ability imposes limitations on the success of desired reactions. Therefore, efficient charge separation while maintaining the highest attainable redox potential for electrons and holes becomes highly crucial. This specific approach, known as the direct Z-scheme, successfully achieves the desired charge transfer objective (refer to Fig. 1.9d). In a Z-scheme heterojunction, the photoexcited electrons in one semiconductor (PS II) will move to and recombine with the holes generated in another semiconductor (PS I). This allows the remaining higher-energy electrons (in PS I) and holes (in PS II) to participate in redox reactions[133], [134]. Despite possessing the same band alignment as a type-II heterojunction, the crucial factor behind this charge transfer mechanism lies in the difference in work function. In Fig. 1.10a, it is observed that PS I possesses higher CB and VB positions as well as a smaller work function compared to PS II. When PS I and PS II come into close contact, the free electrons in PS I transfer to PS II at the interface until their Fermi levels are balanced (Fig. 1.10b). As a result, PS I becomes positively charged, while PS II becomes negatively charged at the interface, creating a built-in electric field directed from PS I to PS II. Additionally, PS I experiences upward band bending, and PS II experiences downward band bending at the interface. Under excitation by incident light, both photocatalysts generate electron-hole pairs. The built-in electric field at the interface promotes the recombination of photogenerated electrons in the CB of PS II with photogenerated holes in the VB of PS I (Fig. 1.10c)[135]. Moreover, the presence of the built-in electric field and the additional potential barrier due to band bending effectively suppress other charge transfer pathways, ensuring the Z-scheme mechanism is favored (Fig. 1.10d-e)[18], [136]. Consequently, the photogenerated electrons in the CB of PS I and holes in the VB of PS II become spatially separated and participate in the photocatalytic redox reactions.

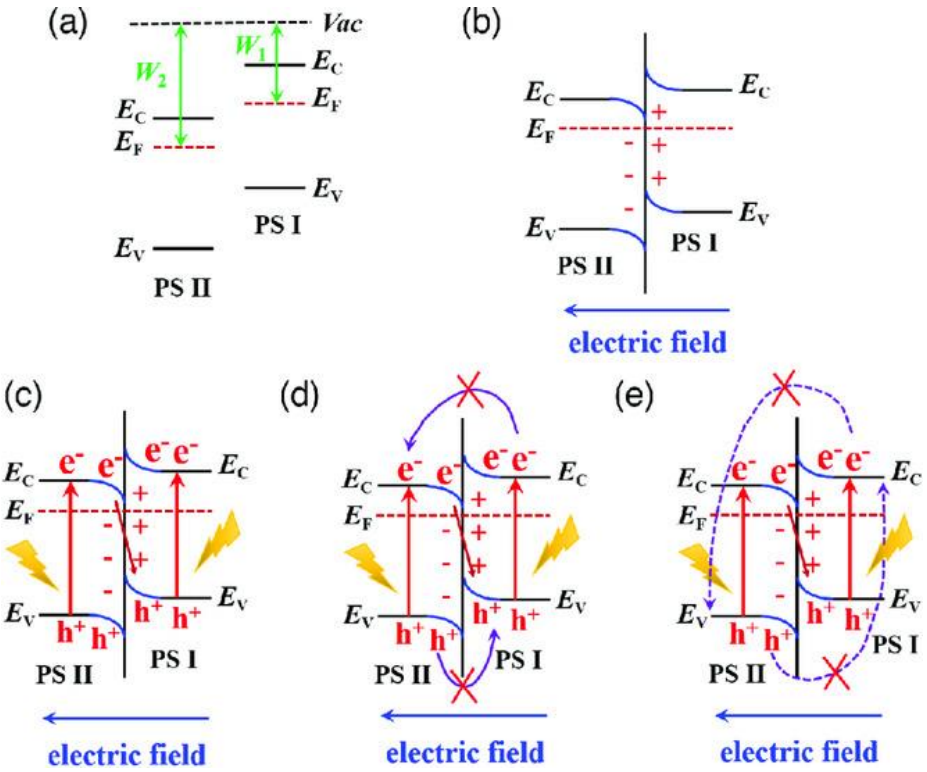


Figure 1.10. Illustration of semiconductor-semiconductor junction with staggered band configurations ($W_1 < W_2$) a) prior to contact, b) during contact. c) Z-scheme charge transfer mechanism. (d-e) Suppressed photogenerated carrier transfer routes in Z-scheme system. $W_1$ and $W_2$ represent the work function of PS I and PS II, respectively. $V_{ac}$, $E_C$, $E_V$, and $E_f$ correspond to the vacuum level, CB, CB, and Fermi level, respectively. Copyright 2017, Elsevier [137].

COF-based heterojunctions have been extensively utilized in various photocatalytic applications, including hydrogen evolution and wastewater treatment[138]–[140]. For example, in the study conducted by Yang *et al.*[75], $TiO_2$ NSs were incorporated into COP-64,enhancing the migration of electrons from the CB of COP-64 to the CB of $TiO_2$, as well as the transfer of holes from the VB of $TiO_2$ to COP-64. It displayed a high rate of hydrogen evolution (15.02 $mmol \cdot h^{-1}\ g^{-1}$). Thote *et al.*[128] demonstrated that combining CdS with 2D TpPa-2 COF not only enhances the photostability of CdS but also significantly increases its photocatalytic activity. Despite employing a small amount of TpPa-2 COF to anchor CdS nanoparticles, the CdS−COF hybrid (depicted in Fig. 1.11)

showed an impressive hydrogen evolution rate of 3.68 mmol·$g^{-1}$ $h^{-1}$ under visible light irradiation, employing lactic acid as the sacrificial agent. The photocatalytic performance of this system can be attributed to the uniform distribution of CdS on the sheet-like π-π stacking 2D TpPa-2 COF, which effectively reduces the recombination of electron pairs.

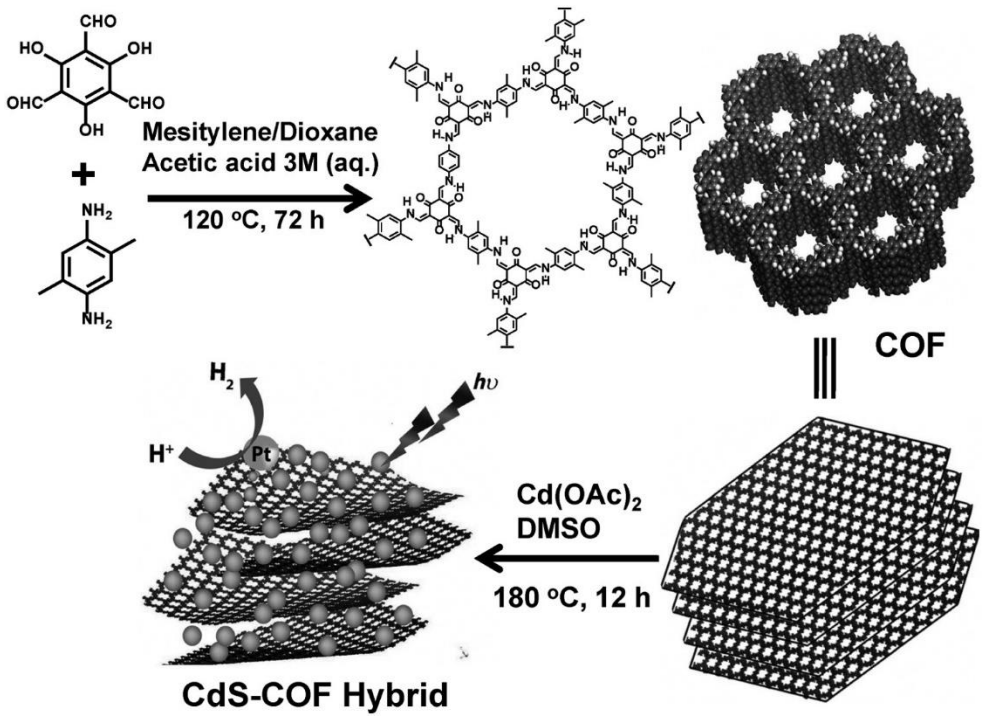


Figure 1.11. Schematic illustration of synthesis of COF TpPa-2 and the hydrothermal synthesis of CdS-COF hybrid[105]. Copyright 2014, Chemistry Europe.

In $CO_2$ photoreduction, Li *et al.*[128] successfully synthesized a metal-free 2D/2D photocatalyst by combining black phosphorus with CTF. The CTF- black phosphorus composite showed strong activity for $CO_2$-to-CO and $CO_2$-to-$CH_4$, which was attributed to the favorable band structure of the composite. DFT calculations revealed that CTF-BP stabilizes the CO* intermediate, thereby enhancing the hydrogenation of CO* to form $CH_4$. The production rates were found to be 7.81 μmol $g^{-1}$ $h^{-1}$ for $CH_4$ and 4.60 μmol $g^{-1}$ $h^{-1}$ for CO.

In $CO_2$ reduction, to harness the potential of Z-scheme systems, it is important to have suitable photocatalysts that are active for water oxidation (at the oxidation site) and $CO_2$ reduction (at the reduction site). Additionally, the combination of the two photocatalysts should result in a well-integrated, ordered, and uniform system [13], [80], [97], [129], [141]. These heterojunctions should possess favorable band structures and catalytic properties, aiming to enhance the photo-activity of the individual components and minimize $e^-/h^+$ recombination within the COFs[13], [75].

One of the most efficient and stable dioxane-lined COFs was reported in 2020, named as COF-318 (Fig. 1.12a) COF-318 is constructed using high conjugated units: HHTP and 2,3,5,6-tetrafluoro-4-pyridinecarbonitrile (TFPC)[97]. In a study carried out by Zhang *et al.* [12], the COF-318 was combined with three different inorganic semiconductors ($TiO_2$, $Bi_2WO_6$, and α-$Fe_2O_3$), among which $TiO_2$ exhibited superior performance in $CO_2$-to-CO photoreduction. The $TiO_2$- COF-318 composite demonstrated a remarkable CO production rate of 69.68 μmol $g^{-1}.h^{-1}$ with 100% selectivity achieved within just 4 hours of visible-light exposure. LUMO of COF-318 is more negative than the needed reduction potential to convert $CO_2$ into CO (-0.75 eV), while the HOMO of $TiO_2$ is more positive than the oxidation potential, which facilitates to the oxidation of water into hydrogen (Fig. 1.12b).They showed that COF-318-$TiO_2$ 2D/2D heterojunction formed a Z-scheme. Remarkably, no photosensitizer or sacrificial electron agent was required. DFT calculations revealed that the covalent binding between COF-318 and $TiO_2$, supported by FT-IR spectroscopy and X-ray photoelectron, plays a crucial role in facilitating the separation of $e^-/h^+$ pairs. Moreover, the high electronic conjugation of the linking units in COF-318 promotes the migration of excited electrons primarily responsible for $CO_2$-to-CO reduction. This study sheds light on the design and development of novel Z-scheme photocatalysts based on COFs to enhance $CO_2$ reduction performance and serve as a source of inspiration for my own research project, guiding me towards exploring novel approaches to improve $CO_2$ reduction efficiency.

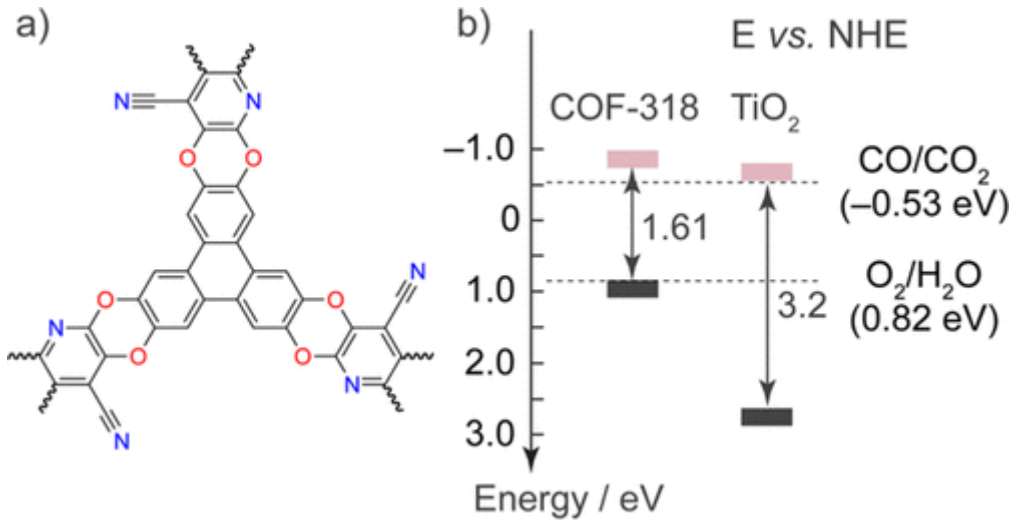


Figure 1.12. (a) COF-318 molecular structure and (b) schematic illustration of band structures of COF-318 and $TiO_2$. Copyright 2020, Wiley-VCH.

As one of the aims of this research project is to create an efficient heterojunction, in the next section, we will delve into the potential of bismuth vanadate ($BiVO_4$) as an exceptional candidate as a second semiconductor to form a 2D/2D composite with the chosen COF. Different from $TiO_2$, 2D $BiVO_4$ shows strong visible light excitation capability and well as high specific surface area. We will explore its main properties, structures, and its application in photocatalytic $CO_2$ conversion systems. $BiVO_4$ offers promising attributes such as favorable band structures and catalytic properties, which can significantly enhance the photo-activity of COFs and effectively minimize $e^-/h^+$ pair recombination rates within the COFs.

### *1.3 $BiVO_4$ in photocatalytic $CO_2$ reduction*

#### *1.3.1 $BiVO_4$ structure and properties*

In its natural form, bismuth vanadate ($BiVO_4$) adopts an orthorhombic crystalline structure known as pucherite[142]. Synthetic $BiVO_4$, on the other hand, primarily shows three crystal structures: monoclinic scheelite (m-s), tetragonal scheelite (t-s), and tetragonal zircon (t-z), as depicted in Fig. 1.13[143]. In all three structures, V ions are coordinated by four oxygen atoms, while Bi ions are coordinated by eight oxygen atoms (Fig. 1.13A-

C). However, the scheelite and zircon structures differ in terms of how Bi ions are bound to the $VO_4$ tetrahedra. In scheelite phases, Bi ions are surrounded by eight (or six) $VO_4$ tetrahedra, while in zircon phases, Bi ions are surrounded by six $VO_4$ tetrahedra. Similarly, the scheelite phases also differ on the V-O bond lengths, being 1.72 Å for the t-s structure, and 1.77 Å and 1.69 Å for m-s structure[133], [142], [144], [144].

The m-s $BiVO_4$ stands out as the favored choice for photocatalysis due to its stable thermodynamic properties and superior ability to harness visible light for catalytic reactions[145]. The higher photocatalytic performance of m-s $BiVO_4$, as compared to t-z $BiVO_4$, can be attributed to the creation of additional electronic states [146], [147]. This is a consequence of the interaction between Bi 6s and O 2p orbitals, which appear above the VB[144]. This interaction leads to a reduction in the bandgap from 2.9 eV (t-z) to 2.4 eV (m-s), enhancing its absorption in the visible range of the spectrum (see Fig. 1.13D)[133], [146], [148].

Experimental data have shown that its bandgap falls within the range of 2.4 to 2.5 eV[149]. Its absorption coefficient increases from 10000 $cm^{-1}$ at the onset of band edge absorption around 500 nm to 100000 at 460 nm, as illustrated in Fig. 1.13E. $BiVO_4$ displays a yellow hue due to its strong absorption of green to ultraviolet photons and its ability to transmit yellow to infrared photons[148], [133].

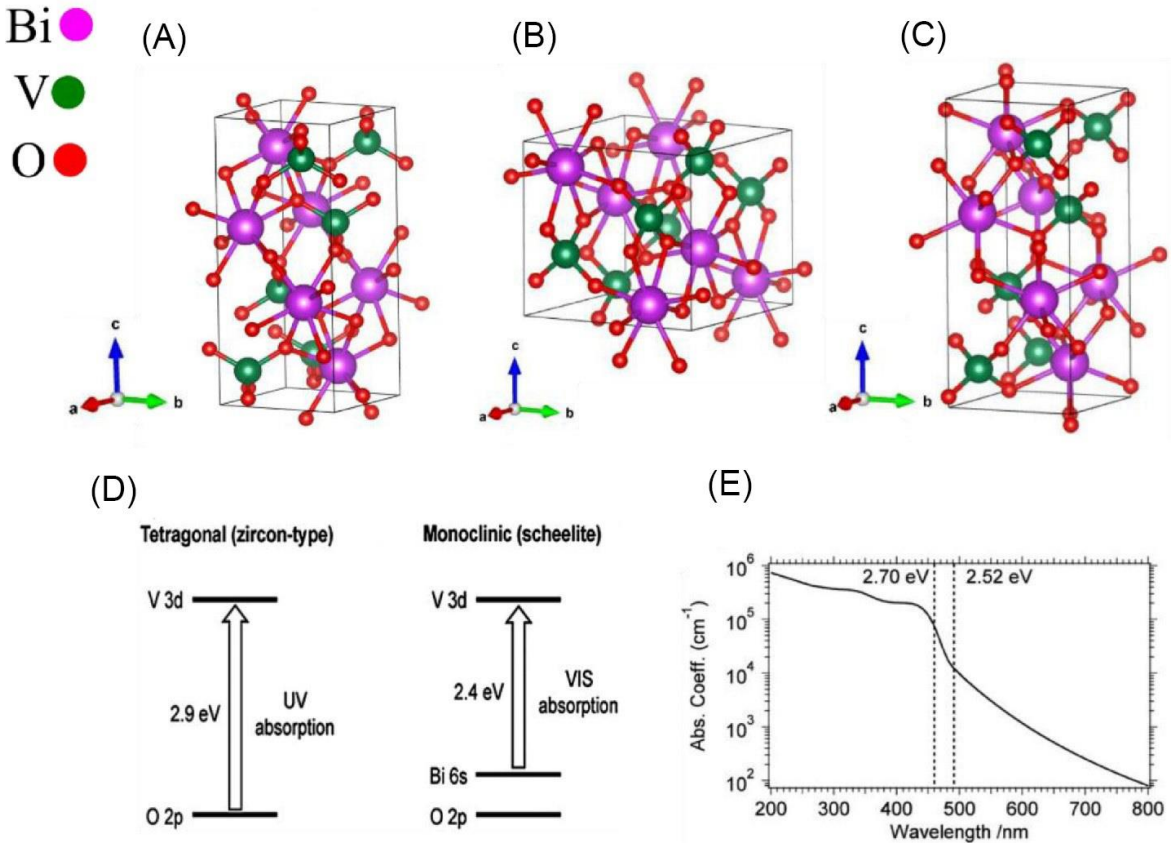


Figure 1.13. The crystal structure of $BiVO_4$: (A) tetragonal scheelite, (B) tetragonal zircon, (C) monoclinic scheelite and (D) band structures of monoclinic scheelite and tetragonal zircon $BiVO_4$ [150]. Copyright 2013, Royal Society of Chemistry (E) The absorption coefficient of monoclinic $BiVO_4$ [151]. Copyright 2015, American Chemical Society.

$BiVO_4$ is extensively employed as a photocatalyst in various reactions, including the degradation of organic pollutants, water splitting, and $CO_2$ reduction[147], [152]. In the context of photocatalytic water splitting, the generated holes in $BiVO_4$ are utilized to oxidize water molecules and produce $O_2$[153]. However, due to its relatively low CB position, $BiVO_4$ alone is insufficient to reduce water or $CO_2$ molecules[154], [155]. Because of this, the incorporation of another semiconductor in the system is of great importance, preferably forming a type II or Z-scheme heterojunction. In this configuration, $BiVO_4$ would facilitate the oxidation processes (*i.e.* water oxidation), while the other material would assist with the $CO_2$ reduction reactions[155], [156].

### *1.3.2 $BiVO_4$-based photocatalysts for $CO_2$ photoreduction*

Given the promising results reported for $BiVO_4$ photocatalysts in the water oxidation half-reaction, it is crucial to engineer multiple semiconductor materials to enhance solar light absorption, accelerate photocatalysis, and improve charge separation and transfer. Maintaining high redox potentials for both photoelectrons and holes is vital in order to enhance the conversion of $CO_2$ to fuel under photocatalytic conditions [157].

Up to date, there are many studies published using heterojunctions with $BiVO_4$ and other semiconductors[158]. One of the most used materials in combination with $BiVO_4$ is $Cu_2O$. It showcases favorable band energy positions, making it compatible for efficient charge transfer [159]. For example, Zhou *et al.* [160] recently published $BiVO_4${010}–Au–$Cu_2O$ solid-mediated Z-scheme heterojunction, which incorporates a facet-dependent junction that acts as an efficient route for electron transfer. The preparation process involved the solid-state synthesis of $BiVO_4$ with different co-exposed crystal facets ({010} and {110}), followed by the deposition of Au or $Cu_2O$ onto the $BiVO_4$ surface using a photoreduction method. Compared to pristine materials, this heterostructure displayed superior activity in the reduction of $CO_2$ into either $CH_4$ or CO, with rates of 3.15 and 2.08 μmol $g^{-1}$ $h^{-1}$, respectively. The authors proposed that the transfer of photoexcited electrons at the $BiVO_4$–Au interfaces to $Cu_2O$ played a crucial role in determining the efficiency of charge separation and controlling the photoreduction activity. In the photocatalyst, the electrons generated in the CB of $BiVO_4$ migrate towards the contact interface in between, where they recombine with holes residing in the VB of $Cu_2O$. Consequently, this recombination process leads to the formation of long-lived holes in the VB of $BiVO_4$ and electrons in the CB of $Cu_2O$. Fig. 1.14A illustrates the proposed mechanism.

In another study Li *et al*. [156] employed reduced graphene oxide (RGO) as an electron mediator in addition to the $Cu_2O/BiVO_4$, forming a Z-scheme heterojunction for $CO_2$ reduction. The bare $Cu_2O$ catalyst produced approximately 0.05 μmol of HCOOH and 0.06 μmol of $H_2$ after 24 hours of simulated solar light irradiation. In contrast, $Cu_2O$-RGO/$BiVO_4$ demonstrated higher conversion rates, yielding 0.65 μmol of HCOOH and 0.73 μmol of $H_2$. The improved photocatalytic performance was attributed to the formation of a Z-scheme, facilitating electron transfer from the CB of $BiVO_4$ to the VB of $Cu_2O$[161].

$BiVO_4/Cu_{0.4}V_2O_5$ direct Z-scheme catalyst was developed by employing a co-precipitation method to grow $Cu_{0.4}V_2O_5$ nanosheets on the surface of $BiVO_4$ microplates[162]. Pristine $BiVO_4$ displayed only trace amount of CO, indicating its low activity in the conversion of $CO_2$ to CO through photocatalysis. Pristine $Cu_{0.4}V_2O_5$ exhibited a CO production rate of 2.18 μmol $g^{-1}$ $h^{-1}$. However, when the two materials were combined to form the Z-scheme heterojunction, the CO production rate increased approximately 4.4 times compared to that of $Cu_{0.4}V_2O_5$ alone. According to the authors, the migration of charges in $BiVO_4/Cu_{0.4}V_2O_5$ occurred by transferring photoinduced electrons from the conduction CB of $BiVO_4$ to the VB of $Cu_{0.4}V_2O_5$, followed by recombination with the holes present in $Cu_{0.4}V_2O_5$. This process resulted in the accumulation of photoinduced electrons with a strong reduction potential in the CB of $Cu_{0.4}V_2O_5$ and holes with a high positive oxidation potential in the VB of $BiVO_4$. Finally, the photoexcited electrons in the CB of $Cu_{0.4}V_2O_5$ facilitated the reduction of $CO_2$ to CO, as shown in Fig. 1.14B.

Bian *et al.* [163] developed a novel heterojunction based on a cascade structure of (001) $TiO_2$-g-$C_3N_4/BiVO_4$. Various weight percentages of g-$C_3N_4$ and $TiO_2$ were investigated, being the optimal ratio 15 wt.% of g-$C_3N_4$ and 5 wt.% of (001) $TiO_2$. The system exhibited a CO production rate of 60 μmol $g^{-1}$ after 4 hours, with minimal $CH_4$ and $O_2$ resulting from the water oxidation half-reaction. The authors proposed that the enhanced activity was attributed to accelerated and maximized charge transfer facilitated by closely connected interfaces (see in Fig. 1.14C).

Mengfei Lu *et al.* [164] presented a similar catalyst employing a thermal-polymerization and subsequent hydrothermal method to create a 2D/2D coupling of g-$C_3N_4$ and $BiVO_4$ ultrathin nanosheets. The resulting heterostructures demonstrated significantly improved in the catalytic performance, with $CH_4$ and CO evolution rates of 4.57 and 5.19 μmol $g^{-1}$ $h^{-1}$, respectively. These values were 4.8 and 4.4 times higher compared to the gaseous products produced by pure g-$C_3N_4$. The remarkable enhancement in $CO_2$ reduction is due to the accelerated charge transfer and efficient charge separation facilitated by the face-to-face arrangement of the 2D/2D ultrathin nanosheets and the Z-scheme configuration (as illustrated in Fig. 1.14D). Importantly, from a thermodynamic perspective, it is worth highlighting that the photogenerated electrons in the CB of g-$C_3N_4$

possess sufficient energy to drive the reduction of $CO_2$, as their potentials are more negative than the potential of $CO_2/CH_4$ (-0.24 eV vs. NHE)[164].

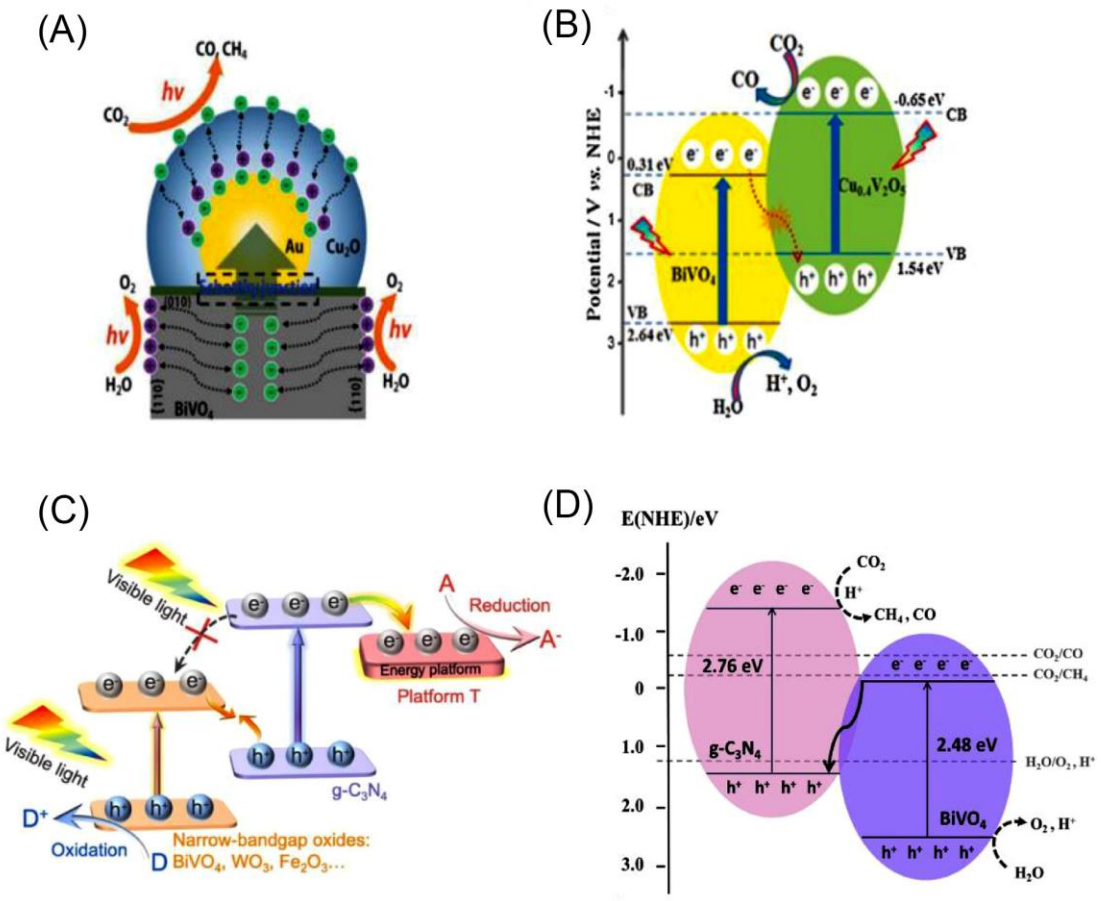


Figure 1.14. Z-scheme proposed to describe the charge transfer mechanism of (A) $BiVO_4${010}-Au-$Cu_2O$[160], (B) $BiVO_4/Cu_{0.4}V_2O_5$[162], (C) (001) $TiO_2$-g-$C_3N_4/BiVO_4$ [163] and (D) g-$C_3N_4/BiVO_4$ [164]. (A) Copyright 2018, Wiley Online Library, (B) Copyright 2021, Elsevier, (C) Copyright 2021, Wiley-VCH, and (D) Copyright 2020, Elsevier.

# Chapter 2: Materials and methods

## *2.1. Materials*

All solvents and reagents were used in their commercially sourced form without any additional purification. Tetrafluorophthalonitrile (99%, TFPN), bismuth nitrate pentahydrate ($Bi(NO_3)_3 \cdot 5H_2O$, 99.99%), ammonium metavanadate ($NH_4VO_3$, 99.9%), 1,4-dioxane, trimethylamine, N, N-dimethylformamide (DMF, AR), octadecene (ODE, 90%), oleylamine (OLA, 70%), oleic acid (OA, 90%), tetrahydrofuran (THF, 99.5%), ammonia solution ($NH_4OH$, 33%), mercaptopropionic acid (MPA, ≥99%), hexane, methanol, ethanol, and acetone were purchased from Sigma Aldrich. 2,3,6,7,10,11-hexahydroxytriphenylene (≥ 98%, HHTP) was purchased from Tokyo Chemical Industry (TCI) Co., Ltd. The reagents were used without any further purification unless specify.

## *2.2. Synthesis of COF-316*

### *2.2.1. Conventional synthesis (COF-316$_S$)*

The solvothermal synthesis of COF-316 was carried out according to a previously reported method[25]. In a Pyrex Schlenk tube (30 mL), 30 mg (0.09 mmol) of HHTP, 27.6 mg (0.138 mmol) of TFPN, 2 mL of 1,4-dioxane, and 0.078 mL of trimethylamine were combined. The mixture was sonicated for approximately 15 minutes before being rapidly frozen at 77 K (using a liquid $N_2$ bath) and degassed to achieve an internal pressure of ~100 mTorr. The mixture was then heated to 120 ºC and allowed to remain undisturbed (without stirring) for 72 hours. Following filtration and washing with DMF and THF, the wet sample was transferred to a Soxhlet extractor and washed with THF (for 24 hours) and acetone (for 24 hours). Finally, the product was subjected to dynamic vacuum at 150 ºC overnight to produce the activated sample.

### *2.2.2. Microwave-assisted synthesis (COF-316$_M$)*

In a Schlenk tube (30 mL), 30 mg (0.09 mmol) of HHTP, 27.6 mg (0.138 mmol) of TFPN, 2 mL of 1,4-dioxane, and 0.078 mL of trimethylamine were combined. The mixture was sonicated for approximately 15 minutes before being rapidly frozen at 77 K (using a liquid $N_2$ bath) and degassed to achieve an internal pressure of ~100 mTorr. After 3 pump-thaw

cycles, the mixture was transferred into a microwave reactor in the glove box. Then, the reactor was heated to 130 $^{o}$C in a microwave oven (CEM, 100 W, standard method) for 4h without stirring. Following filtration and washing with DMF and THF, the wet sample was transferred to a Soxhlet extractor and washed with THF (for 24 hours) and acetone (for 24 hours). Finally, the product was subjected to dynamic vacuum at 150 $^{o}$C overnight to produce the activated sample.

### *2.3. Synthesis of $BiVO_4$ nanosheets*

#### *2.3.1. Synthesis of ultrathin $BiVO_4$ nanosheets*

To synthesize ultrathin 2D $BiVO_4$ nanosheets, a standard procedure was followed[23]. Initially, a mixture of $Bi(NO_3)_3{\cdot}5H_2O$ (0.5 mmol), OA (1 mL), OLA (1 mL), and ODE (10 mL) was placed in a three-neck flask and heated to 170 °C under $N_2$ atmosphere until $Bi(NO_3)_3$ was fully dissolved. Meanwhile, $NH_4VO_3$ (1 mmol) was dissolved in a mixture of $HNO_3$ (2 mL) and $H_2O$ (10 mL) in a separate vessel. The resulting aqueous solution was then injected into the flask containing the dissolved $Bi(NO_3)_3$ and the mixture was kept at 100°C for 40 minutes under $N_2$ atmosphere. Afterward, the reaction solution was allowed to cool down naturally to room temperature before adding hexane and ethanol. The solution was then left to settle, and the aqueous solution at the bottom was discarded. The organic solution was centrifuged to remove any unreacted precursors, and the products were washed with hexane and ethanol through a total of three centrifugation cycles.

#### *2.3.2. Ligand exchange to obtain water-dispersible ultrathin $BiVO_4$ nanosheets*

The $BiVO_4$ nanosheets were made water-soluble by replacing their original hydrophobic ligands (primarily OLA) with hydrophilic thiol-terminated MPA. To do this, a standard exchange procedure was used[165], in which 450 µL of MPA was dissolved in 12.5 mL of methanol, and the pH value of the solution was raised to 10.0 by adding $NH_4OH$. The MPA solution was then mixed with a hexane dispersion of $BiVO_4$ (18 mg/mL) and stirred vigorously for 2 hours. The resulting MPA-coated $BiVO_4$ nanosheets were precipitated using 50 mL of hexane and 12.5 mL of IPA, and the $BiVO_4$ nanosheets were collected by centrifugation at 6000 rpm for 6 minutes, followed by two washing steps with IPA to

remove any excess MPA ligands. Finally, the product was dispersed in 10 mL of water, resulting in a homogeneous and yellow solution.

### *2.4. Synthesis of COF-316$_M$/BiVO$_4$ nanosheets*

The in-situ reaction method was used to synthesize COF-316$_M$/BiVO$_4$. HHTP (30 mg, 0.09 mmol), TFPN (24 mg, 0.138 mmol), and ligand-exchanged BiVO$_4$ (at quantities of 12 mg, 19.3 mg, 30 mg, and 48 mg) were combined with 1,4-dioxane (2 mL) in a microwave reactor tube (30 mL). The mixture was sonicated for 60 minutes to ensure complete mixing. Trimethylamine (0.078 mL) was added and the mixture was sonicated for an additional 10 minutes. The tube was then flash-frozen at 77 K (in a liquid $N_2$ bath) and degassed to achieve an internal pressure of ~100 mTorr. After three pump-thaw cycles, the solution was transferred into a microwave reactor tube in the glovebox. Using a microwave oven, the mixture was heated to 130 ºC and left undisturbed for 4 hours. The resulting mixture was filtered, washed with DMF and THF, and then transferred to a Soxhlet extractor. The sample was washed with THF (during 24 h) and acetone (during another 24 h). Finally, the samples activated by being evacuated at 150 ºC under a dynamic vacuum overnight to yield the final products (COF-316M/BiVO$_4$ (20%, 30%, 40% and 50% w/w).

### *2.5. Materials characterization*

The X-ray diffraction (XRD) patterns were obtained using a D/max-γA X-ray diffractometer (Rigaku, Japan) operating at 40 kV and 70 mA, with Cu Kα radiation (λ = 0.154178 nm) and a scanning rate of 0.7° per min in 2θ ranging from 2° to 90°. To examine the morphology and structure of the as-prepared nanosheets transmission electron microscopy (TEM) and high-resolution analytical transmission electron microscopy (HRTEM, JEM-2100F, JEOL) techniques were employed. Absorption of samples were analyzed using a LAMBDA™ 1050 UV/Vis/NIR spectrometer along with 150-mm integrating sphere (PerkinElmer, Inc., Shelton, CT USA). Fourier transform infrared spectroscopy (FTIR; Jasco 4200, accessorized by attenuated total reflectance (ATR) module. A Bruker ALPHA Platinum ATR-FTIR spectrometer, which featured a single reflection diamond ATR module, was utilized to record Attenuated Total Reflectance

(ATR) FT-IR spectra. The surface areas of the as-prepared nanostructures were identified using the $N_2$ adsorption–desorption isotherms achieved on a Brunauer–Emmett–Teller (BET) instrument (Quantachrome Autosorb-1). X-ray photoelectron spectroscopy (XPS) were recorded using a Escalab 250Xi instrument from Thermo Scientific equipped with an Al Kα micro-focused X-ray source as well as UV lamp and the C1s peak at 284.6 eV as internal standard.

### *2.6. Photocatalytic measurements*

In a continuous solid-gas reaction mode, an initial step involved the dispersion of 10 mg of photocatalyst in 2 mL of deionized water using ultrasonic waves, followed by pouring it into a round petri dish with a diameter of 5 cm placed at the bottom of the reactor. Ultra-pure $CO_2$ (99.99%) was passed through water to generate saturated $CO_2$ gas. The system was purged with a constant flow of 10 mL/min for 30 minutes in dark to eliminate any air present within the reactor. Then, during 3 hours of light irradiation, the concentrations of products in the reactor were analyzed by an online GC/FID/TCD. An auto-sampling system was employed to inject the gaseous sample into the GC/FID/TCD every 45 min. Also, a series of blank experiments were carried out to ensure that any carbon-containing products measured by GC were genuinely produced from $CO_2$ photocatalytic reduction.

# Chapter 3: COF-316/$BiVO_4$ nanocomposite photocatalyst

*3.1. Introduction*

COFs are a type of porous organic polymer with a high surface area and tunable properties, which makes them attractive for their use in photocatalysis[1]. Their specific surface area can vary depending on their structure and synthesis method[2], [3]. However, reported BET surface area values for COFs typically range from 300 to 2500 $m^2/g$ which is higher than metal oxides whose BET surface area typically ranges from tens to a few hundred $m^2/g$ [4]–[6]. Another great advantage of COFs over other types of photocatalysts is their ability to absorb a wide range of light wavelengths, including visible light, which enables efficient utilization of solar energy[7], [8]. Moreover, their structure can be designed and tailored to optimize the catalytic performance and selectivity towards desired products via different methods such as metalation or the formation of heterojunctions[9], [10]. These properties demonstrate the potential of COFs as a highly efficient and selective photocatalyst for $CO_2$ reduction applications[3].

Dioxane-linked COF-316, defined by its robust stability, 2D structure, copious micropores, extensive surface area (>500 $m_2/g$), and broad light absorption in UV and visible range, serves as a photocatalyst for $CO_2$ reduction under visible light[11]. The chemical structure of COF is shown in Fig. 3.1. It can effectively adsorb $CO_2$ molecules through its nitrile groups (-CN), primarily converting them into CO gas [97]. However, despite its impressive photocatalytic performance, COF-316 has some important limitations, such as low oxidation ability and high charge carrier recombination rate, hindering its photocatalytic activity especially in aquatic media. Therefore, researchers have been working on improving its performance by incorporating other materials or modifying its structure[7], [11], [13].

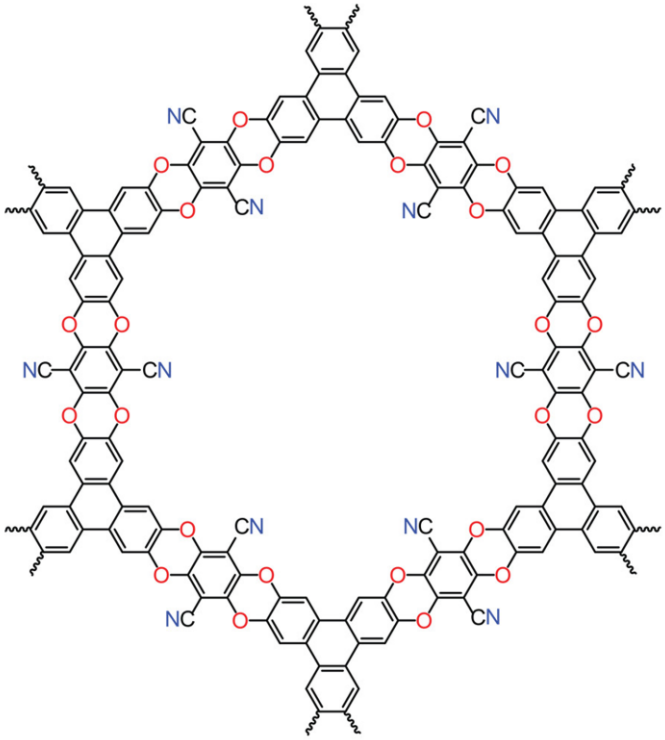


Figure 3.1. The chemical structure of COF-316

2D materials, such as COF-316, have gained significant traction in the field of photocatalysis due to their numerous advantages over bulk materials[14]. When compared to their bulk materials, 2D materials usually exhibit higher specific surface areas, allowing for greater interaction with $CO_2$ reactant molecules. Additionally, they offer shorter charge carrier migration distances from the interior to the surface, facilitating more efficient photocatalytic processes. Furthermore, 2D materials possess a higher concentration of catalytically useful defects (*e.g.,* oxygen vacancies) and an abundance of surface atoms with unsaturated coordination sites[15], [16]. These features contribute to the availability of a larger number of active sites for catalytic reactions. More importantly, the combination of 2D nanomaterials to generate 2D/2D heterojunctions can yield synergistic effects resulting from increased charge separation and reduced $e^-/h^+$ recombination. These enhancements are achieved through improved surface contact and an expanded interface area[17], [18].

Bismuth-based semiconductors have gained substantial attention as a class of 2D materials, owing to their distinctive physio-chemical properties[19]. Notably, $BiVO_4$ nanosheets exhibit remarkable photocatalytic activity for water splitting due to their advantageous electronic band structure and narrow bandgap of 2.4 eV[166]. This narrow bandgap facilitates enhanced absorption of visible light, resulting in their excellent performance. Furthermore, its high specific surface area provides abundant active sites for photocatalytic reactions, amplifying their catalytic performance[19], [166]. Its highly oxidative ability allows the system to oxidize water, eliminating the need for a sacrificial agent[19], [20]. Thus, the combination of $BiVO_4$ and COF-316 to build a 2D/2D composite can potentially create a highly efficient and versatile photocatalyst system that can effectively drive $CO_2$ reduction reaction in the presence of water.

Microwave-assisted synthesis of COFs has been found to reduce the reaction time significantly. Microwave irradiation is known to efficiently heat reaction mixtures through the interaction of electromagnetic radiation with polar molecules, primarily through dipole rotation[167]. This rapid and selective heating can lead to several factors affecting the reaction kinetics: (i) enhanced heat transfer: microwave heating generates localized heat within the reaction vessel. This enables faster and more uniform heating throughout the reaction mixture compared to conventional heating methods. As a result, heat transfer limitations are reduced, which can accelerate reaction rates, (ii) efficient energy transfer: microwaves directly couple with reactant molecules that have dipole moments. This efficient energy transfer can provide the activation energy required for chemical reactions more effectively than traditional heating methods, which might rely on slower heat diffusion, (iii) uniform temperature distribution: microwave heating tends to create a more uniform temperature distribution within the reaction vessel, minimizing temperature gradients. This can prevent uneven reaction progress, contributing to enhanced kinetic control[21], [22], [167], [168].

In my thesis, I pursued three main objectives: (i) to develop a novel microwave-assisted approach for synthesizing COF-316, in order to significantly reduce the synthesis time; (ii) to create a new 2D/2D COF-316/$BiVO_4$ nanocomposite, aiming to enhance charge transport and, consequently, improve $CO_2$ reduction efficiency by forming a 2D/2D

nanocomposite structure and achieve improved active catalytic surface area; and (iii) to establish a Z-scheme charge transfer system, enabling high photocatalytic $CO_2$ reduction performance in gas-solid state without the need for additional sacrificial agents or photosensitizers (see Fig. 3.2).

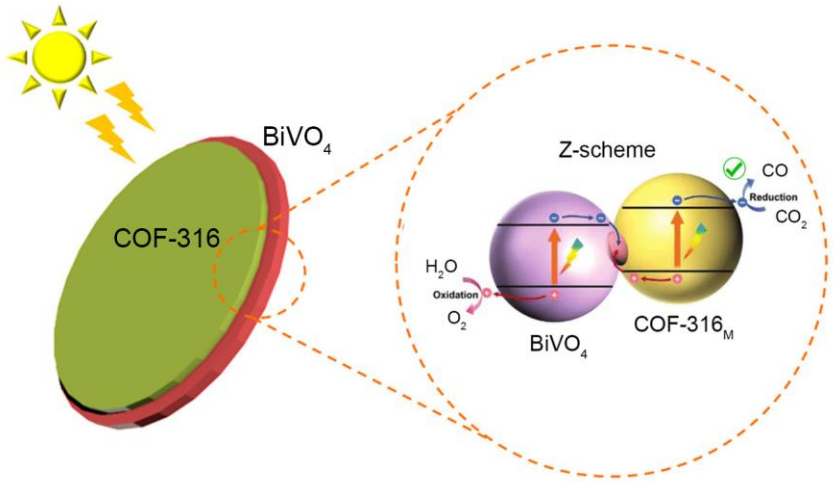


Figure 3.2. Desired 2D/2D Z-scheme charge transfer mechanism for photocatalytic $CO_2$ reduction process.

We reported a new microwave-assisted synthesis method for COF-316 which reduces the reaction time by 95% and developed a new 2D/2D COF-$316_M$/$BiVO_4$ composite for $CO_2$ reduction under visible light irradiation. This microwave heating method, unlike traditional techniques, allows for faster and more efficient heating from within[21]. This new approach, capitalizing on the benefits of microwaves, streamlines the synthesis process, making it quicker and more energy-efficient[22]. The samples were characterized using various analytical techniques and their photocatalytic performance was examined in gas-solid phase in presence of water without any sacrificial agent or any additional photosentesizer.

### *3.2. Structural and morphological characterization*

XRD was performed to validate the crystal structure of the nanomaterials and nanocomposite. Fig. 3.3a-b shows XRD of both COF-$316_S$ and COF-$316_M$ samples. Peaks at 2θ values of 4.34°, 8.8°, 11.22°, and 26.9° correspond to the reflection planes of (100), (200), (210), and (001), respectively, indicating an ordered and of orthorhombic

phase crystalline structure[97]. The XRD patterns of COF-316$_S$ and COF-316$_M$ showed an exact match. This serves as validation of the efficacy of the microwave-assisted synthesis. As can be seen from Fig. 3.3c, the peaks associated with $BiVO_4$ NSs affirm their pure monoclinic phase and high degree of crystallinity[23]. The XRD profile of the 2D/2D COF-316$_M$/$BiVO_4$ nanocomposite (showed in Fig. 3.3d) displays distinct diffraction peaks of both nanomaterials, providing evidence for the successful incorporation of $BiVO_4$ NSs and COF-316$_M$ onto the surface of each other of the without altering their crystal structure. The diffraction profiles of $BiVO_4$ and COF-316$_M$/$BiVO_4$ exhibited variations in the intensity of (020) and (040) peaks at 15° and 31°, respectively, indicative of a quantity-dependent change. This observation suggests a preferential parallel alignment between the {010} planes of $BiVO_4$ nanosheets and the substrate without any accompanying changes in the phase or composition of the material[16], [23].

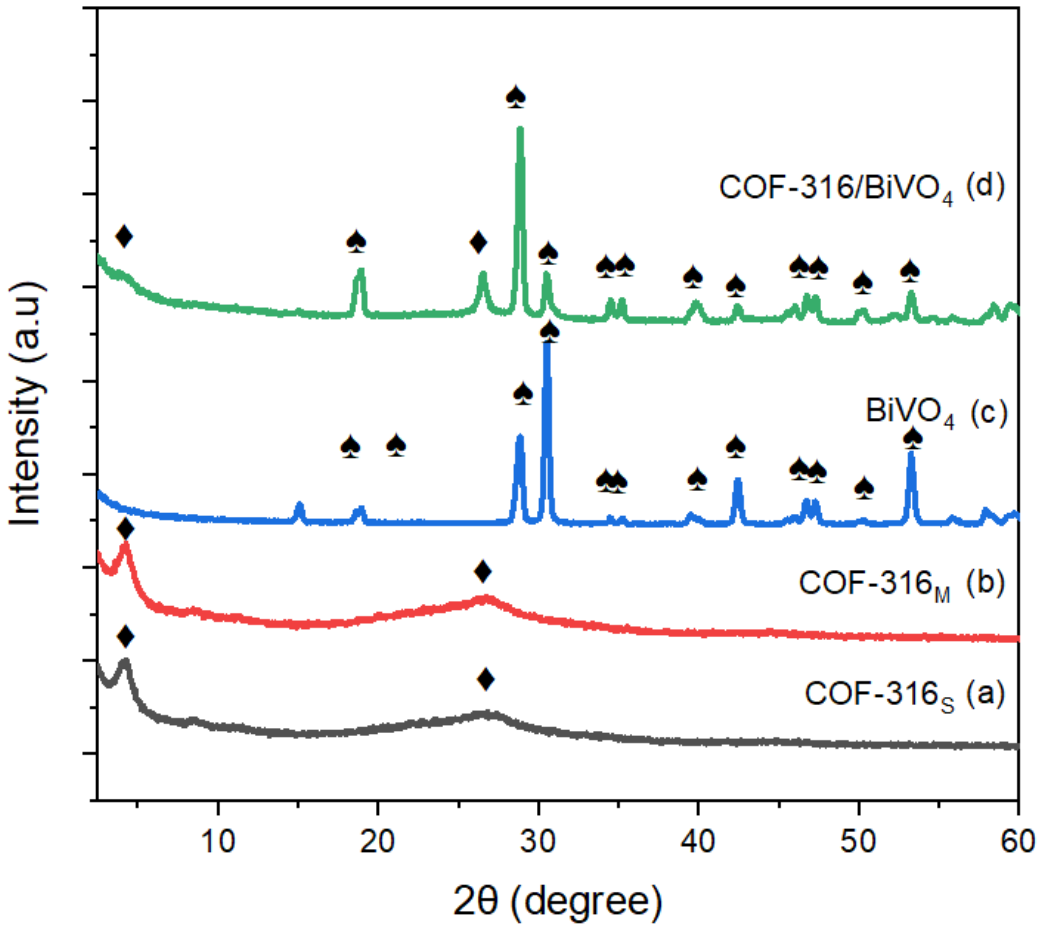

Figure 3.3. XRD patterns of (a) COF-316$_S$, (b) COF-316$_M$, (c) $BiVO_4$, and (d) COF-316$_M$/$BiVO_4$ nanocomposite.

To confirm the chemical composition and functional groups of the HTTP (building block), TFPN, COF-316$_S$, COF-316$_M$, $BiVO_4$, and COF-316$_M$/$BiVO_4$, Fourier-transform infrared spectroscopy (FTIR) was performed. Results shown in Fig. 3.4a-b displayed the characteristic dioxin C–O asymmetric and symmetric stretching modes, observed within both COF-S and COF-M samples, at 1240 to 1262 and 1008 to 1020 $cm^{-1}$, respectively[24]. This observation serves as evidence for the formation of the dioxin bond in the COF-316$_M$ structure. Meanwhile, the disappearance of -OH (~3300 $cm^{-1}$) in the HTTP further provided additional evidence for the formation of the bond[25]. Also, the results indicate the presence of -CN functional groups at ~2250 $cm^{-1}$ in COF-316$_S$, COF-316$_M$ and COF-316$_M$/$BiVO_4$ that can potentially facilitate photocatalytic $CO_2$ reduction reactions[11], [97]. The FTIR spectrum of the 2D/2D COF-316$_M$/$BiVO_4$ showed the absorption peaks of both the COF-316$_M$ and $BiVO_4$ components. The peak at 750 $cm^{-1}$ was attributed to $v_1(VO_4)$ of monoclinic $BiVO_4$[26]. These results confirmed the well incorporation of $BiVO_4$ NSs onto the surface of the COF-316$_M$. The FT-IR results supported the successful synthesis of COF-316$_S$, COF-316$_M$, $BiVO_4$, and 2D/2D COF-316$_M$/$BiVO_4$.

XPS and EDX measurements were performed to gain deeper insights into the elemental composition and chemical environment of the elements conforming COF-316$_M$/$BiVO_4$ nanocomposite. The full survey spectrum of COF-316$_M$/$BiVO_4$ (Fig. 3.4c) revealed the presence of C, O, N, Bi, V, and F within the structure. The obtained elemental composition from the XPS spectrum and EDX analysis for COF-316$_M$/$BiVO_4$ is summarized in Table 1.

| Element | Atomic fraction (%) from XPS | Atomic fraction (%) from EDX |
|---|---|---|
| C | 71.2 | 70.9 |
| O | 20.4 | 19.9 |
| Bi | 2.3 | 2.6 |
| V | 2.1 | 2.5 |
| N | 3.1 | 3.5 |
| F | 0.9 | 0.6 |

Table 1. Elemental composition of COF-316$_M$/$BiVO_4$ (20% w/w)

Fig. 3.4d illustrated the C 1s spectrum for COF-316$_M$/$BiVO_4$ sample, displaying distinct peaks at 286.1, 284.6, 286.6, and 288.2 eV, that are attributed to -C≡N, C-C/C=C, C-O, and C-F, respectively. For O 1s (Fig. 3.4e), the binding energy at 529.9 and 533.8 eV corresponds to lattice oxygen in the $BiVO_4$ structure and C-O in the COF-316$_M$ framework, respectively[16]. N 1s spectrum showed distinct peak of pyridinic N (-C≡N) at 399.48 (see Fig. 3.4f). The Bi 4f spectrum displayed spin-orbit splitting patterns for Bi $4f_{5/2}$ and Bi $4f_{7/2}$ peaks (Fig. 3.4g) at 164.96 and 159.64 eV, respectively. Furthermore, Fig. 3.4h showed the binding energy values of V $2p_{3/2}$ and V $2p_{1/2}$ in the COF-316$_M$/$BiVO_4$ at 517.05 and 524.36 eV, respectively, confirming the presence of $V^{5+}$ within the lattice[23]. A small amount of F was also detected in the form of C-F, attributed to residual TFPN linkers in the structure. This minor contamination is commonly reported in the synthesis of dioxane-linked COFs[11], [13], [24]. The C 1s XPS pattern of COF-316$_M$ achieved through microwave synthesis demonstrated a perfect match with that of COF-316$_S$, providing further proof the successful microwave synthesis (see Fig. 3.4i). [24], [97].

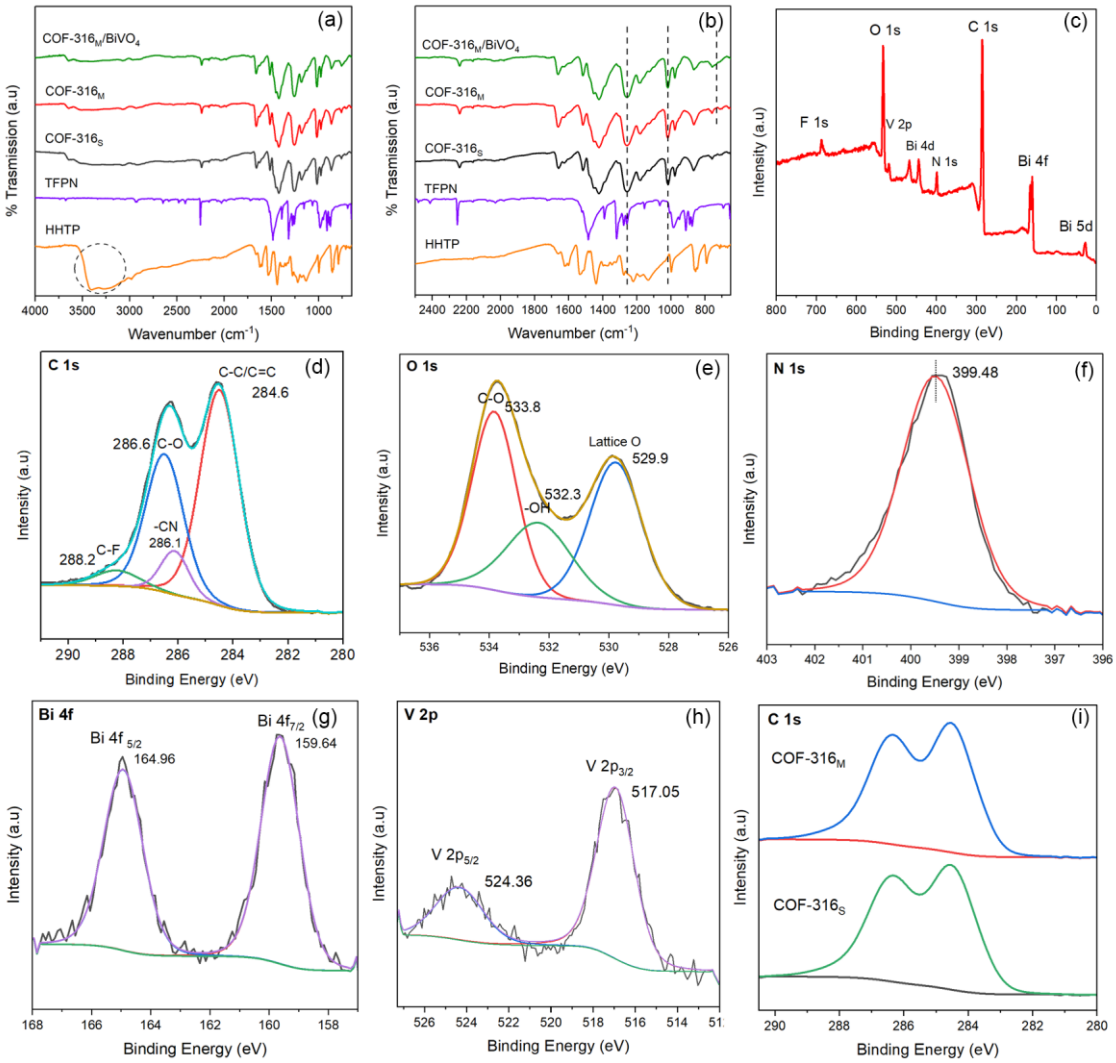


Figure 3.4. (a-b) FT-IR patterns of HTTP, TFPN, COF-316$_S$, COF-316$_M$, and COF-316$_M$/$BiVO_4$ nanocomposite. (c) Full survey XPS spectrum and high resolution XPS spectra of (d) C 1s (e) O 1s (f) N 1s (g) Bi 4f (h) V 2p of COF-316$_M$/$BiVO_4$ sample. (i) High resolution XPS spectra of C 1s of COF-316$_M$ and COF-316$_S$ samples.

In order to investigate the structure and morphology of the COF-316$_S$, COF-316$_M$, $BiVO_4$, and 2D/2D COF-316$_M$/ $BiVO_4$, TEM and HRTEM were carried out. The TEM images of the COF-316$_s$ and COF-316$_M$ revealed a remarkable similarity in their morphology, with both indicating a uniform and interconnected sheet-like structure (Fig. 3.5a-b). $BiVO_4$ NSs showed a lateral size of 1-1.5 micrometers, as it can be seen in Fig. 3.5c. The TEM analysis of the 2D/2D COF-316$_M$/$BiVO_4$ showed the successful growth of COF-316$_M$ on the $BiVO_4$ NSs (Fig. 3.5d). Also, HRTEM images of COF-316$_M$/ $BiVO_4$ (Fig. 3.5e-f) illustrated the distinguishable contact between the COF-316$_M$ and $BiVO_4$, essential for the separation and migration of photoinduced charge carriers[27]. The HRTEM image demonstrated that the $BiVO_4$ NSs possessed a high degree of crystallinity, featuring lattice fringes with interplanar spacings of 0.260 and 0.255 corresponding to the (200) and (002) planes of monoclinic $BiVO_4$, respectively[16]. However, due to the electron beam sensitivity of COFs, HRTEM imaging failed to reveal any clear lattice fringe or diffraction pattern for COF-316$_M$[28]. EDX mapping images provided evidence of the existence of C, O, N, Bi, and V elements in the composite sample, thereby indicating the absence of any contamination (Fig. 3.5g-l). The dispersion of C and N elements across the $BiVO_4$ nanosheets strongly supports the integration of $BiVO_4$ within the COF-316$_M$ layers, forming a distinct 2D/2D structure.

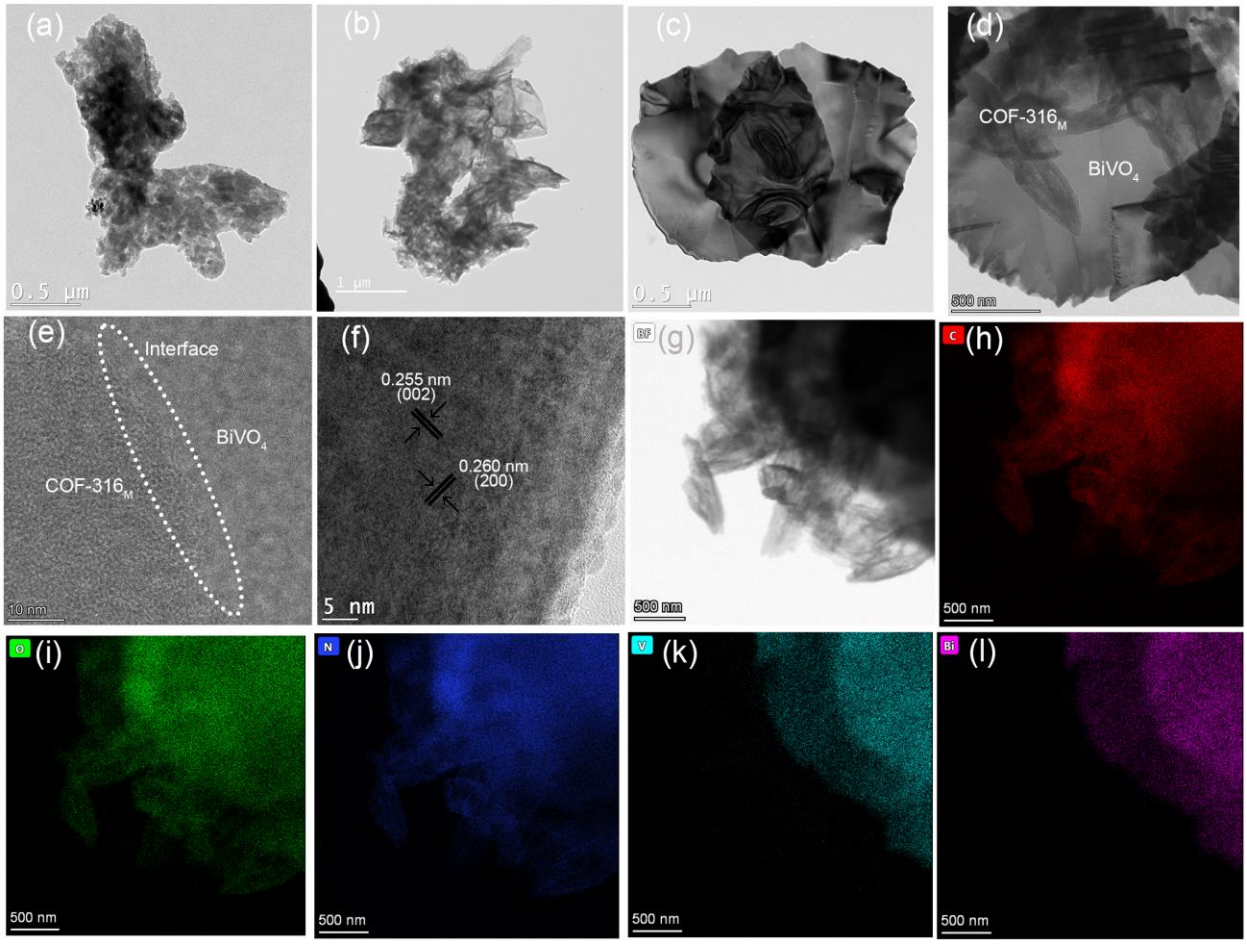


Figure 3.5. TEM images of (a) COF-316$_S$, (b) COF-316$_M$, (c) $BiVO_4$, (d) COF-316$_M$/$BiVO_4$ nanocomposite, (e-f) HRTEM images of COF-316$_M$/$BiVO_4$, (g-l) TEM image and associated EDS elemental mapping images of COF-316$_M$/$BiVO_4$. White circle in e highlights the interface between the two materials.

### *3.3. Textural property analysis*

$N_2$ adsorption/desorption measurements were conducted at standard temperature and pressure (STP) conditions to evaluate the porous structures and surface areas of COF-316$_S$, COF-316$_M$, $BiVO_4$, and 2D/2D COF-316$_M$/$BiVO_4$ samples (Figures 3.6a-d). By utilizing the BET technique, the specific surface area of COF-316$_M$ (592.264 $m^2/g$) was relatively higher than COF-316$_S$ (544.335 $m^2/g$). The isotherm patterns display a distinctive Type I shape[25], [29]. In addition, the surface area of COF-316$_M$/$BiVO_4$ was

260.291 $m^2/g$, which is relatively smaller than that of pure COF-$316_M$ (see the Fig. 3.6c-d). This discrepancy can be attributed to the presence of $BiVO_4$, which possesses a low surface area of approximately 1.8 $m^2/g$ and may block the micropores of COF-$316_M$. Pore size distribution analysis was done using nonlocal density functional theory (NL-DFT) model. The analysis of the $N_2$ adsorption isotherms revealed that the pore size distribution of COF-316 samples ranges between approximately 0.9 nm and 1.2 nm (see inset figures in Fig. 3.6a-b), in a good agreement with the experimental and theoretical results for the eclipsed stacking mode found in literature[11], [13], [25], [29], [97]. The similarities between the experimental and predicted pore size values not only provides robust validation of the analysis but also serves as compelling evidence of the efficacy of the microwave-assisted synthesis. This particular micropore characteristic was also observed in COF-$316_M$/$BiVO_4$.

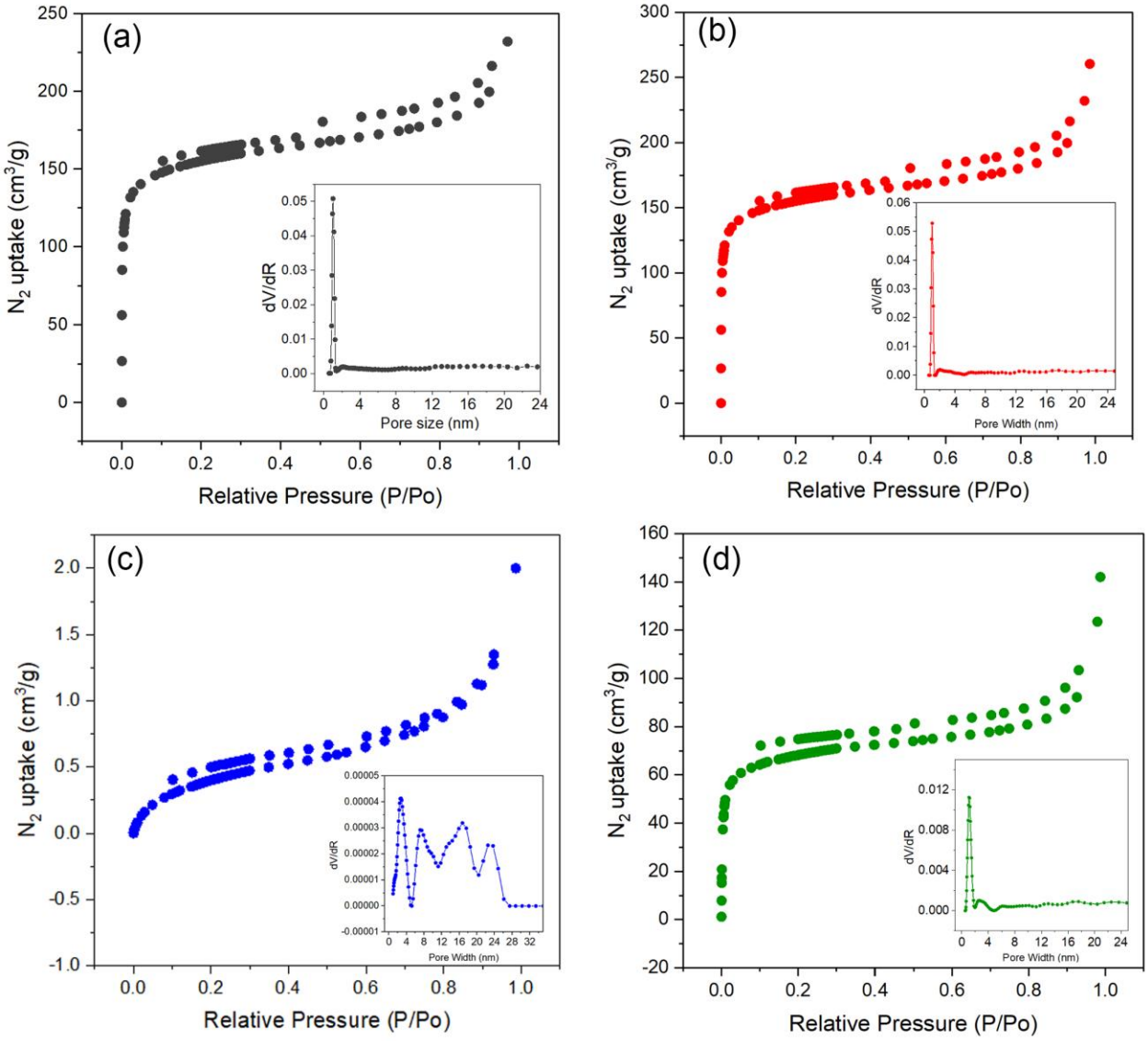


Figure 3.6. $N_2$ adsorption/desorption isotherms and pore size distribution (inset) of (a) COF-316$_S$, (b) COF-316$_M$, (c) $BiVO_4$, (d) COF-316$_M$/$BiVO_4$ nanocomposite.

### *3.4. Optical properties*

The optical properties of COF-316$_M$, $BiVO_4$ and COF-316$_M$/$BiVO_4$ nanocomposite were investigated using solid-state UV-vis absorption spectrophotometer. As shown in Fig. 3.7a, all samples have absorption from the UV range up to about 475 nm in the visible range. The absorption properties of COF-316$_S$ and COF-316$_M$ were almost similar. COF-316$_M$/$BiVO_4$ displayed a slight blue shift in the absorption edge compared to COF-316$_M$,

however, it exhibited enhanced absorption in visible range beyond the optical response of $BiVO_4$. Through the Tauc plot analysis, the measured optical band gaps for COF-$316_S$, COF-$316_M$, $BiVO_4$, and COF-$316_M$/$BiVO_4$ were 2.11 eV, 2.12 eV, 2.35 eV, and 2.28 eV, respectively (See the Fig. 3.7b). This suggests a slight reduction in the overall band gap when compared to bare $BiVO_4$. So, the reduction of the band gap combined with increased light absorption can promote the generation of $e^-/h^+$ pairs. Consequently, the COF-$316_M$/$BiVO_4$ nanocomposite can potentially offer improved performance and higher photocatalytic activity in $CO_2$ reduction reactions.

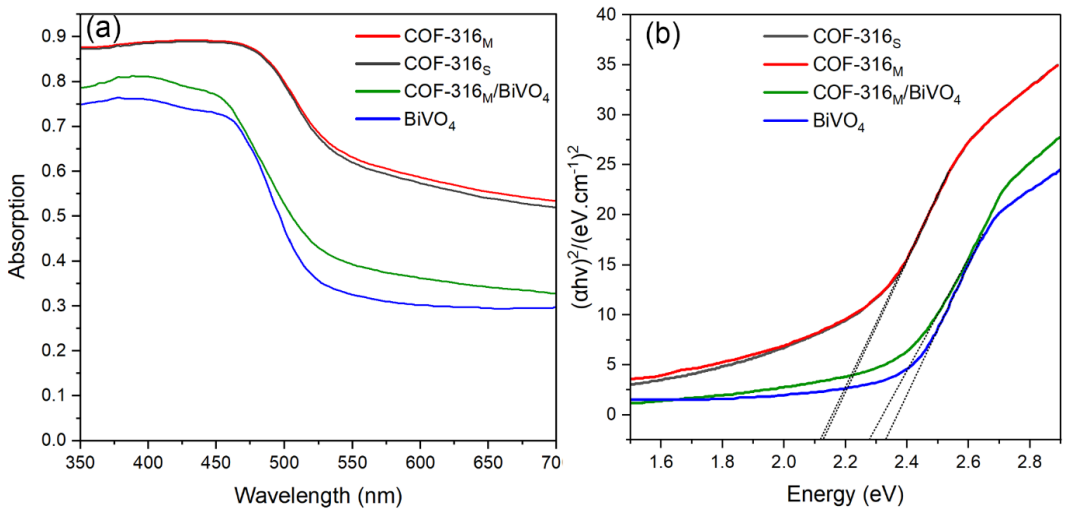


Figure 3.7. (a) Absorption spectra and (b) Tauc plots of COF-$316_S$, COF-$316_M$, $BiVO_4$ and COF-$316_M$/$BiVO_4$ nanocomposite.

### *3.5. Photocatalytic $CO_2$ reduction performance*

The photocatalytic performance of COF-$316_S$, COF-$316_M$, $BiVO_4$ and COF-$316_M$/$BiVO_4$ (20% - 50%) were studied under visible light (>420 nm, 100 mW/$m^2$) and results were shown in Fig. 3.8. COF-$316_S$ showed ~2.5 µmol.$g^{-1}$.$h^{-1}$, which is in a good agreement with reported values in the literature[11], [97]. Notably, COF-$316_M$ showed greater photocatalytic $CO_2$ reduction of 3.8 µmol. $g^{-1}$.$h^{-1}$ compared to its solvothermally synthetized counterpart (~150% of increased activity). This could be attributed to enhanced BET surface area of COF-$316_M$ obtained from microwave heating method compared to COF-$316_S$. In order to verify that the source of CO originates from the

conversion of $CO_2$ within the system and not from the COF or carbon contamination, three control experiments were conducted. The first involved passing $N_2$ instead of $CO_2$, while the second experiment involved passing $CO_2$ in the absence of photocatalysts. The third one involved with passing $CO_2$ in presence of catalyst but not presence of light (dark condition). In all experiments, no products were observed, providing evidence for the exclusive CO generation through $CO_2$ conversion. $BiVO_4$ itself produced trace amount of CO product due to its poor redox ability.

Since all the characterization techniques showed the same properties for solvothermal and microwave-assisted COF-$316_S$, and COF-$316_M$ with much shorter synthesis time displayed higher $CO_2$ production rate as well, only COF$_{-316M}$ has been chosen to combine with $BiVO_4$ to form the heterojunction. In addition, the facile and rapid synthesis of COF-$316_M$ has been taken into consideration on this regard. By incorporating $BiVO_4$ in the COF framework, the photocatalytic performance dropped compared to pristine COF-$316_S$ and COF-$316_M$ samples. The CO production rate for COF-$316_M$/$BiVO_4$ (20%), (30%), (40%) and (50%) was 1, 0.8, 0.25, 0.15 µmol. $g^{-1}.h^{-1}$.

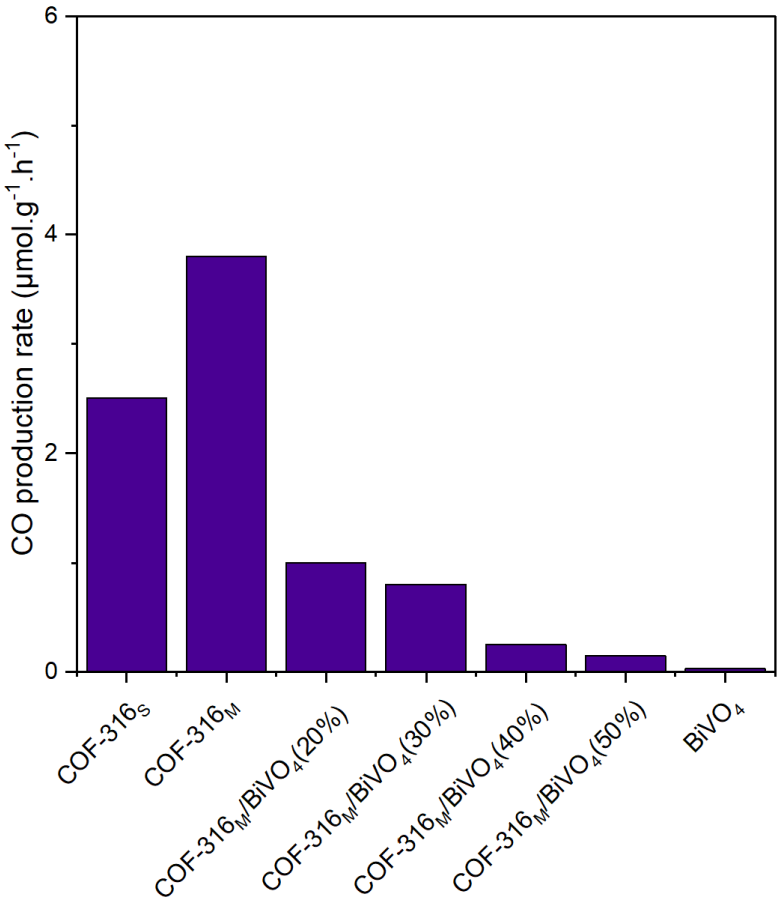


Figure 3.8. Comparative study on the photocatalytic activity of COF-316$_S$, COF-316$_M$, $BiVO_4$, and COF-316$_M$/$BiVO_4$ with different weight ratios under visible light, using water as a hole scavenger without any sensitizer.

We considered two potential reasons for the decrease in efficiency. Firstly, we explored the possibility that incomplete removal of long-chain organic ligands during the ligand-exchanging process from the surface of $BiVO_4$ could lead to relatively large interparticle distances, inefficient contact and poor charge transfer between the two COF-316$_M$ and $BiVO_4$ components[30], [31]. However, analysis of FTIR spectra before and after ligand exchange indicated almost complete removal of OLA or OA ligands with vibrations around 2300 and 2800-2850 $cm^{-1}$, ruling out this as the cause for the reduced efficiency (See Fig. 3.9).

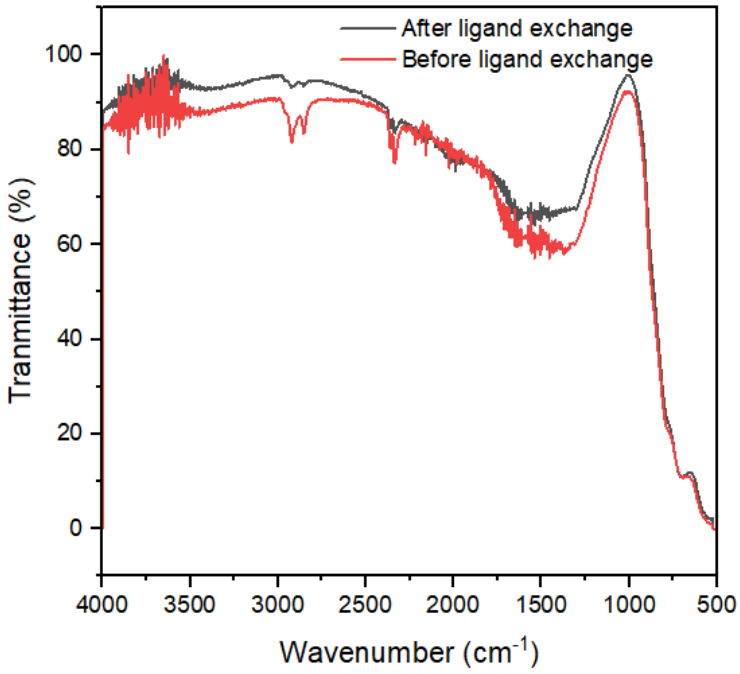


Figure 3.9. FTIR spectra of $BiVO_4$ nanosheets before and after ligand exchange process.

The second reason for drop in efficiency could be explored through investigating charge transfer route and mechanism. To obtain a thorough understanding of the charge transfer mechanism within the heterojunction, we conducted a detailed analysis by comparing the XPS spectra of COF-$316_M$/$BiVO_4$ under three different conditions: before exposure to light (in the dark), during light irradiation (under UV light), and after (again in the dark). It is important to note that changes in the binding energies of an element directly indicate variations in its electron density, something we expect to happen when performing this type of analysis[32], [33]. Specifically, a decrease or increase in electron density leads to a negative or positive shift in the binding energy, respectively[34]. This makes XPS a powerful technique for accurately determining the direction of charge transfer in heterojunctions, such as COF-$316_M$/$BiVO_4$[35]. According to Fig. 3.10a, the peaks corresponding to Bi $4f_{7/2}$ and Bi $4f_{5/2}$ experienced a shift towards lower values of approximately 0.4 eV. A similar trend was observed for V $2p_{3/2}$ and V $2p_{1/2}$, where they showed a shift towards negative binding energies (Fig. 3.10b). This phenomenon confirms that the electron cloud density near the Bi and V atoms of COF-$316_M$/$BiVO_4$

within the heterojunction increases. Consequently, electron transfer occurs from the CB of COF-316$_M$ to the CB of $BiVO_4$, following the type II heterojunction charge transfer pathway (see Fig. 3.10f). The opposite peak shift observed in the N 1s peak (Figure 3.10c) further supports this phenomenon. The subsequent return of the peaks to its original position after the UV light irradiation provides evidence that this shift is a result of charge transfer at the interface, rather than a change in the chemical composition of the material under light[33], [36].

The valance and conduction band energy level positions of COF-316$_M$ and $BiVO_4$ were evaluated using UPS technique (Fig. 3.10d-e). In the secondary cut-off region, the work function (W) is determined as W = 21.22 eV (He I) - (cutoff - $E_f$) eV vs. vacuum. To analyze the valence band level the equation $E_{VB}$ (vs. vacuum) = W + extrapolation value in the valence band region is employed. To convert the W and VB potential value to the NHE scale, the equation $E_{NHE}$ = 4.5 eV - $E_{vac}$ is used. Based on UPS results and Tauc plots in 3.4, accordingly, the $E_f$, $E_{VB}$ and $E_{CB}$ potentials of $BiVO_4$ were -3.76 eV, -6.9 eV and -4.55 eV vs vacuum level, respectively. Similarly, the $E_f$, $E_{VB}$ and $E_{CB}$ potentials of COF-316$_M$ were -4.58, -6.02 and -3.9 eV vs vacuum level respectively. As discussed, 1.2.5.2, due to the higher Fermi level of $BiVO_4$ in comparison to COF-316$_M$, the charge transfer mechanism upon the band bending and light illumination will follow the type II heterojunction charge transfer mechanism. Due to the poor redox potential of $BiVO_4$ (CB: +0.05 eV vs NHE), the redox ability of electrons transferring from the CB of COF-316$_M$ to the CB of $BiVO_4$ decrease significantly, resulting in diminished photocatalytic performance in the composites.

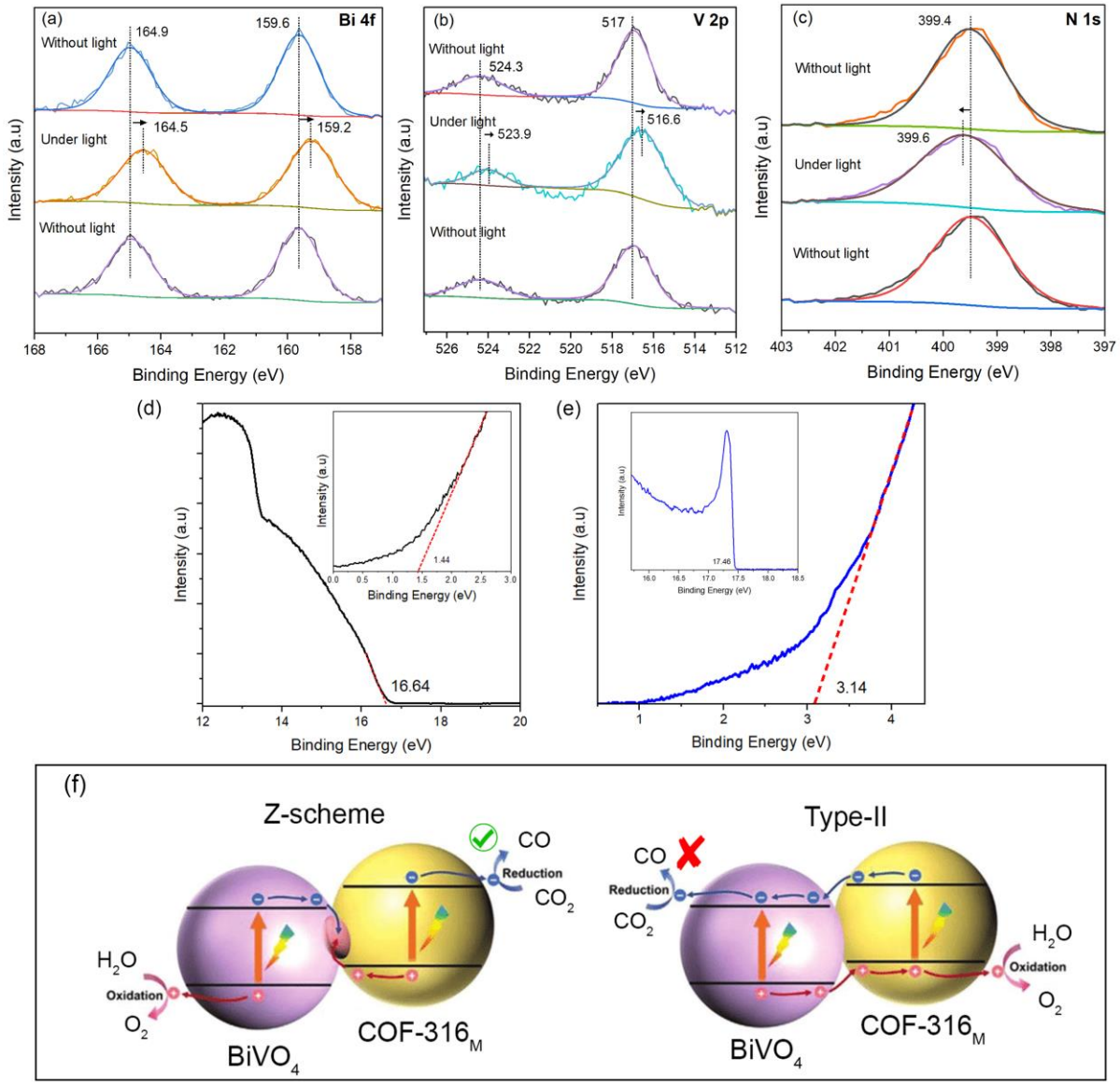


Figure 3.10. In-situ XPS analysis of COF-316$_M$/BiVO$_4$: investigating (a) Bi 4f, (b) V 2p, and (c) N 1s behaviors during off/on/off cycles under UV light. UPS spectrum of (d) COF-316$_M$ and (e) BiVO$_4$. (f) Schematic charge transfer mechanism at the interface of COF-316$_M$/BiVO$_4$.

# 4. Conclusion and future outlook

COF-316 was synthesized through a new microwave method that reduced the reaction time from 3 days to 4 hours at 130°C. COF-$316_M$ showed the BET surface area of 592.264 $m^2/g$, surpassing the surface area of conventionally synthesized COF-$316_S$ (544.335 $m^2/g$). COF-$316_M$ showed higher BET surface area compared to COF-$316_S$. 2D/2D COF-$316_M$/$BiVO_4$ nanosheets were synthetized and characterized by several techniques such as XRD, FTIR, TEM, HRTEM, EDX mapping, XPS and UV-vis DRS. The individual semiconductors as well as COF-$316_M$/$BiVO_4$ composites with different w/w ratios (from 20% to 50% of $BiVO_4$) were synthesized and used in photocatalytic $CO_2$ reduction. COF-$316_M$ demonstrated a higher CO production rate of 3.8 µmol $g^{-1}.h^{-1}$, whereas COF-$316_S$ showed a lower rate of approximately 2.5 µmol $g^{-1}.h^{-1}$. The composites exhibited a reduction in photocatalytic activity when compared to the pristine COF-$316_M$ and COF-$316_S$. The XPS findings reveal a decrease in electron cloud density around Bi 4f and V 2p in COF/$BiVO_4$ when the sample are exposed to UV light. This indicates a type-II heterojunction charge transfer occurring at the interface, where electrons are transferred from the CB of COF-316 to the CB of $BiVO_4$.

Regarding this project, in order to improve/enhance the photocatalytic activity, we propose two suggestions to be done in the future: (i) Lowering the fermi level of $BiVO_4$ below that of COF-316 could potentially serve as a viable approach to alter the charge transfer mechanism. Removing the oxygen vacancies in the $BiVO_4$ through an annealing process could help to achieve this goal, as it has been reported in literature [16], [23]. Optimizing the annealing conditions can potentially lead in achieving a Z-scheme charge transfer mechanism, (ii) Although the composite samples did not exhibit increased $CO_2$ photoreduction performance compared to pristine COF-$316_M$ and COF-$316_S$, they still hold promise for alternative applications such as photocatalytic wastewater treatment or hydrogen production. The photogenerated electron and holes can participate in highly radical producing reactions make this photocatalyst a suitable candidate for efficient degradation of organic pollutants in wastewater. Hight specific surface area of COF-316/$BiVO_4$ can potentially assist in high adsorption of pollutants on the surface of the photocatalyst which is a crucial step in photocatalysis. Further exploration of these

applications could unlock their full potential and contribute to address environmental issues and contribute on renewable energy technologies.

Microwave-assisted synthesis of COFs reduces reaction times significantly by efficiently heating reaction mixtures through interactions with polar molecules, primarily via dipole rotation, resulting in enhanced heat transfer, efficient energy transfer to dipole-bearing reactants, and uniform temperature distribution within the reaction vessel, all contributing to improved reaction kinetics and enhanced kinetic control. However, it's worth noting that, currently, there is a lack of direct and comprehensive evidence demonstrating any alterations in the COF synthesis mechanism through microwave assistance. As a future avenue of exploration, conducting a comprehensive mechanistic study that compares microwave synthesis with other methods across various synthesis reactions of COFs could offer valuable insights into this technique's possible impact.

## References


[1] H. Wang *et al.*, “Covalent organic framework photocatalysts: Structures and applications,” *Chem. Soc. Rev.*, vol. 49, no. 12, pp. 4135–4165, 2020, doi: 10.1039/d0cs00278j.

[2] J. You, Y. Zhao, L. Wang, and W. Bao, “Recent developments in the photocatalytic applications of covalent organic frameworks: A review,” *J. Clean. Prod.*, vol. 291, p. 125822, 2021, doi: 10.1016/j.jclepro.2021.125822.

[3] Q. Yang, M. Luo, K. Liu, H. Cao, and H. Yan, “Covalent organic frameworks for photocatalytic applications,” *Appl. Catal. B Environ.*, vol. 276, no. February, p. 119174, 2020, doi: 10.1016/j.apcatb.2020.119174.

[4] T. Naseem and T. Durrani, “Environmental Chemistry and Ecotoxicology The role of some important metal oxide nanoparticles for wastewater and antibacterial applications : A review,” *Environ. Chem. Ecotoxicol.*, vol. 3, pp. 59–75, 2021, doi: 10.1016/j.enceco.2020.12.001.

[5] C. Jiang *et al.*, “Constructing Universal Ionic Sieves via Alignment of Two-

Dimensional Covalent Organic Frameworks (COFs)," *Angew. Chemie - Int. Ed.*, vol. 57, no. 49, pp. 16072–16076, 2018, doi: 10.1002/anie.201809907.

[6] C. Wei, S. Sun, D. Mandler, and X. Wang, "Chem Soc Rev Approaches for measuring the surface areas of metal oxide electrocatalysts for determining their intrinsic electrocatalytic activity †," pp. 2518–2534, 2019, doi: 10.1039/c8cs00848e.

[7] H. Zhong *et al.*, "Covalent Organic Framework Hosting Metalloporphyrin-Based Carbon Dots for Visible-Light-Driven Selective CO2 Reduction," *Adv. Funct. Mater.*, vol. 30, no. 35, pp. 1–8, 2020, doi: 10.1002/adfm.202002654.

[8] S. Yang *et al.*, "2D Covalent Organic Frameworks as Intrinsic Photocatalysts for Visible Light-Driven CO2 Reduction," *J. Am. Chem. Soc.*, vol. 140, no. 44, pp. 14614–14618, 2018, doi: 10.1021/jacs.8b09705.

[9] H. L. Nguyen, "Reticular Materials for Artificial Photoreduction of CO2," *Adv. Energy Mater.*, vol. 10, no. 46, pp. 1–23, 2020, doi: 10.1002/aenm.202002091.

[10] H. Shen, T. Peppel, J. Strunk, and Z. Sun, "Photocatalytic Reduction of CO2 by Metal-Free-Based Materials: Recent Advances and Future Perspective," *Sol. RRL*, vol. 4, no. 8, 2020, doi: 10.1002/solr.201900546.

[11] H. Y. Yu *et al.*, "A stack-guiding unit constructed 2D COF with improved charge carrier transport and versatile photocatalytic functions," *Chem. Eng. J.*, vol. 445, no. 94, p. 136713, 2022, doi: 10.1016/j.cej.2022.136713.

[12] M. Zhang *et al.*, "Semiconductor/Covalent-Organic-Framework Z-Scheme Heterojunctions for Artificial Photosynthesis," *Angew. Chemie - Int. Ed.*, vol. 59, no. 16, pp. 6500–6506, 2020, doi: 10.1002/anie.202000929.

[13] Y. J. Chen, Y. Y. Wen, W. H. Li, Z. H. Fu, G. E. Wang, and G. Xu, "TiO2@COF Nanowire Arrays: A 'Filter Amplifier' Heterojunction Strategy to Reverse the Redox Nature," *Nano Lett.*, 2023, doi: 10.1021/acs.nanolett.3c00804.

[14] W. J. Ong, L. K. Putri, and A. R. Mohamed, "Rational Design of Carbon-Based 2D Nanostructures for Enhanced Photocatalytic CO2 Reduction: A Dimensionality

Perspective," *Chem. - A Eur. J.*, vol. 26, no. 44, pp. 9710–9748, 2020, doi: 10.1002/chem.202000708.

[15] H. Yu *et al.*, "Interface Engineering in 2D/2D Heterogeneous Photocatalysts," *Small*, vol. 2205767, pp. 1–30, 2022, doi: 10.1002/smll.202205767.

[16] D. Yao *et al.*, "Oxygen-Defective Ultrathin BiVO4 Nanosheets for Enhanced Gas Sensing," *ACS Appl. Mater. Interfaces*, vol. 11, no. 26, pp. 23495–23502, 2019, doi: 10.1021/acsami.9b05626.

[17] B. Zhu, B. Cheng, J. Fan, W. Ho, and J. Yu, " g-C 3 N 4 -Based 2D/2D Composite Heterojunction Photocatalyst ," *Small Struct.*, vol. 2, no. 12, p. 2100086, 2021, doi: 10.1002/sstr.202100086.

[18] X. Liu, Q. Zhang, and D. Ma, "Advances in 2D/2D Z-Scheme Heterojunctions for Photocatalytic Applications," *Sol. RRL*, vol. 5, no. 2, pp. 1–32, 2021, doi: 10.1002/solr.202000397.

[19] J. Wang, M. Kuo, P. Zeng, L. Xu, S. Chen, and T. Peng, "Few-layer BiVO4 nanosheets decorated with SrTiO3: Rh nanoparticles for highly efficient visible-light-driven overall water splitting," *Appl. Catal. B Environ.*, vol. 279, no. July, p. 119377, 2020, doi: 10.1016/j.apcatb.2020.119377.

[20] J. Feng *et al.*, "Efficient wide-spectrum photocatalytic overall water splitting over ultrathin molecular nickel phthalocyanine/BiVO4 Z-scheme heterojunctions without noble metals," *Appl. Catal. B Environ.*, vol. 295, no. April, p. 120260, 2021, doi: 10.1016/j.apcatb.2021.120260.

[21] B. Díaz de Greñu *et al.*, "Microwave-Assisted Synthesis of Covalent Organic Frameworks: A Review," *ChemSusChem*, vol. 14, no. 1, pp. 208–233, 2021, doi: 10.1002/cssc.202001865.

[22] S. Makhseed and J. Samuel, "Hydrogen adsorption in microporous organic framework polymer," *Chem. Commun.*, no. 36, pp. 4342–4344, 2008, doi: 10.1039/b805656k.

[23] C. Dong *et al.*, "Colloidal Synthesis of Ultrathin Monoclinic BiVO4 Nanosheets for

Z-Scheme Overall Water Splitting under Visible Light," *ACS Catal.*, vol. 8, no. 9, pp. 8649–8658, 2018, doi: 10.1021/acscatal.8b01645.

[24] W. Wang *et al.*, "All-in-One Hollow Flower-Like Covalent Organic Frameworks for Flexible Transparent Devices," *Adv. Funct. Mater.*, vol. 31, no. 29, pp. 1–9, 2021, doi: 10.1002/adfm.202010306.

[25] B. Zhang *et al.*, "Crystalline Dioxin-Linked Covalent Organic Frameworks from Irreversible Reactions," *J. Am. Chem. Soc.*, vol. 140, no. 40, pp. 12715–12719, 2018, doi: 10.1021/jacs.8b08374.

[26] J. B. Liu, H. Wang, S. Wang, and H. Yan, "Hydrothermal preparation of BiVO4 powders," *Mater. Sci. Eng. B Solid-State Mater. Adv. Technol.*, vol. 104, no. 1–2, pp. 36–39, 2003, doi: 10.1016/S0921-5107(03)00264-2.

[27] Y. Zhou *et al.*, "Engineering 2D Photocatalysts toward Carbon Dioxide Reduction," *Adv. Energy Mater.*, vol. 11, no. 8, pp. 1–19, 2021, doi: 10.1002/aenm.202003159.

[28] I. Castano, A. M. Evans, R. Dos Reis, V. P. Dravid, N. C. Gianneschi, and W. R. Dichtel, "Mapping Grains, Boundaries, and Defects in 2D Covalent Organic Framework Thin Films," *Chem. Mater.*, vol. 33, no. 4, pp. 1341–1352, 2021, doi: 10.1021/acs.chemmater.0c04382.

[29] W. Ji, Y. S. Guo, H. M. Xie, X. Wang, X. Jiang, and D. S. Guo, "Rapid microwave synthesis of dioxin-linked covalent organic framework for efficient micro-extraction of perfluorinated alkyl substances from water," *J. Hazard. Mater.*, vol. 397, no. February, p. 122793, 2020, doi: 10.1016/j.jhazmat.2020.122793.

[30] S. J. Oh *et al.*, "Engineering charge injection and charge transport for high performance PbSe nanocrystal thin film devices and circuits," *Nano Lett.*, vol. 14, no. 11, pp. 6210–6216, 2014, doi: 10.1021/nl502491d.

[31] C. R. Kagan and C. B. Murray, "Charge transport in strongly coupled quantum dot solids," *Nat. Nanotechnol.*, vol. 10, no. 12, pp. 1013–1026, 2015, doi: 10.1038/nnano.2015.247.

[32] G. Greczynski and L. Hultman, “X-ray photoelectron spectroscopy: Towards reliable binding energy referencing,” *Prog. Mater. Sci.*, vol. 107, no. June 2018, p. 100591, 2020, doi: 10.1016/j.pmatsci.2019.100591.

[33] S. Tardio and P. J. Cumpson, “Practical estimation of XPS binding energies using widely available quantum chemistry software,” *Surf. Interface Anal.*, vol. 50, no. 1, pp. 5–12, 2018, doi: 10.1002/sia.6319.

[34] L. Wu *et al.*, “In-situ assembling 0D/2D Z-scheme heterojunction of Lead-free Cs2AgBiBr6/Bi2WO6 for enhanced photocatalytic CO2 reduction,” *J. Colloid Interface Sci.*, vol. 629, pp. 233–242, 2023, doi: 10.1016/j.jcis.2022.08.152.

[35] L. Wang, B. Cheng, L. Zhang, and J. Yu, “In situ Irradiated XPS Investigation on S-Scheme TiO2@ZnIn2S4 Photocatalyst for Efficient Photocatalytic CO2 Reduction,” *Small*, vol. 17, no. 41, pp. 1–9, 2021, doi: 10.1002/smll.202103447.

[36] Y. Cui, “In-situ synthesis of C3N4/CdS composites with enhanced photocatalytic properties,” *Cuihua Xuebao/Chinese J. Catal.*, vol. 36, no. 3, pp. 372–379, 2015, doi: 10.1016/S1872-2067(14)60237-0.

[37] H. Abdullah, M. M. R. Khan, H. R. Ong, and Z. Yaakob, “Modified TiO2 photocatalyst for CO2 photocatalytic reduction: An overview,” *J. CO2 Util.*, vol. 22, no. August, pp. 15–32, 2017, doi: 10.1016/j.jcou.2017.08.004.

[38] X. Xiong *et al.*, “Photocatalytic CO2 Reduction to CO over Ni Single Atoms Supported on Defect-Rich Zirconia,” *Adv. Energy Mater.*, vol. 10, no. 46, pp. 1–8, 2020, doi: 10.1002/aenm.202002928.

[39] C. D. Windle and R. N. Perutz, “Advances in molecular photocatalytic and electrocatalytic CO 2 reduction,” *Coord. Chem. Rev.*, vol. 256, no. 21–22, pp. 2562–2570, 2012, doi: 10.1016/j.ccr.2012.03.010.

[40] Q. Liu, J. Lin, H. Cheng, L. Wei, and F. Wang, “ Simultaneous co-Photocatalytic CO 2 Reduction and Ethanol Oxidation towards Synergistic Acetaldehyde Synthesis ,” *Angew. Chemie*, vol. 135, no. 13, 2023, doi: 10.1002/ange.202218720.

[41] J. Fu, K. Jiang, X. Qiu, J. Yu, and M. Liu, “Product selectivity of photocatalytic CO2 reduction reactions,” *Mater. Today*, vol. 32, no. February, pp. 222–243, 2020, doi: 10.1016/j.mattod.2019.06.009.

[42] C. Du, X. Wang, W. Chen, S. Feng, J. Wen, and Y. A. Wu, “CO2 transformation to multicarbon products by photocatalysis and electrocatalysis,” *Mater. Today Adv.*, vol. 6, 2020, doi: 10.1016/j.mtadv.2020.100071.

[43] K. Teramura, Z. Wang, S. Hosokawa, Y. Sakata, and T. Tanaka, “A doping technique that suppresses undesirable H2 evolution derived from overall water splitting in the highly selective photocatalytic conversion of CO2 in and by water,” *Chem. - A Eur. J.*, vol. 20, no. 32, pp. 9906–9909, 2014, doi: 10.1002/chem.201402242.

[44] P. R. Yaashikaa, P. Senthil Kumar, S. J. Varjani, and A. Saravanan, “A review on photochemical, biochemical and electrochemical transformation of CO2 into value-added products,” *J. CO2 Util.*, vol. 33, no. March, pp. 131–147, 2019, doi: 10.1016/j.jcou.2019.05.017.

[45] M. Ramdin *et al.*, “High-Pressure Electrochemical Reduction of CO2 to Formic Acid/Formate: Effect of pH on the Downstream Separation Process and Economics,” *Ind. Eng. Chem. Res.*, vol. 58, no. 51, pp. 22718–22740, 2019, doi: 10.1021/acs.iecr.9b03970.

[46] L. Fan, C. Xia, P. Zhu, Y. Lu, and H. Wang, “Electrochemical CO2 reduction to high-concentration pure formic acid solutions in an all-solid-state reactor,” *Nat. Commun.*, vol. 11, no. 1, pp. 1–9, 2020, doi: 10.1038/s41467-020-17403-1.

[47] S. H. Guo *et al.*, “Enhanced CO2 photoreduction via tuning halides in perovskites,” *J. Catal.*, vol. 369, pp. 201–208, 2019, doi: 10.1016/j.jcat.2018.11.004.

[48] S. Hennessey and P. Farràs, “Production of solar chemicals: Gaining selectivity with hybrid molecule/semiconductor assemblies,” *Chem. Commun.*, vol. 54, no. 50, pp. 6662–6680, 2018, doi: 10.1039/c8cc02487a.

[49] R. Das, S. Chakraborty, and S. C. Peter, “Systematic Assessment of Solvent Selection in Photocatalytic CO2Reduction,” *ACS Energy Lett.*, vol. 6, no. 9, pp. 3270–3274, 2021, doi: 10.1021/acsenergylett.1c01522.

[50] N. M. Dimitrijevic *et al.*, “Role of water and carbonates in photocatalytic transformation of CO 2 to CH4 on titania,” *J. Am. Chem. Soc.*, vol. 133, no. 11, pp. 3964–3971, 2011, doi: 10.1021/ja108791u.

[51] J. Ran, M. Jaroniec, and S. Z. Qiao, “Cocatalysts in Semiconductor-based Photocatalytic CO2 Reduction: Achievements, Challenges, and Opportunities,” *Adv. Mater.*, vol. 30, no. 7, pp. 1–31, 2018, doi: 10.1002/adma.201704649.

[52] E. Karamian and S. Sharifnia, “On the general mechanism of photocatalytic reduction of CO2,” *J. CO2 Util.*, vol. 16, pp. 194–203, 2016, doi: 10.1016/j.jcou.2016.07.004.

[53] Y. Zhang, B. Xia, J. Ran, K. Davey, and S. Z. Qiao, “Atomic-Level Reactive Sites for Semiconductor-Based Photocatalytic CO2 Reduction,” *Adv. Energy Mater.*, vol. 10, no. 9, pp. 1–23, 2020, doi: 10.1002/aenm.201903879.

[54] X. Chang, T. Wang, and J. Gong, “CO2 photo-reduction: Insights into CO2 activation and reaction on surfaces of photocatalysts,” *Energy Environ. Sci.*, vol. 9, no. 7, pp. 2177–2196, 2016, doi: 10.1039/c6ee00383d.

[55] A. Vasileff, C. Xu, Y. Jiao, Y. Zheng, and S. Z. Qiao, “Surface and Interface Engineering in Copper-Based Bimetallic Materials for Selective CO2 Electroreduction,” *Chem*, vol. 4, no. 8, pp. 1809–1831, 2018, doi: 10.1016/j.chempr.2018.05.001.

[56] A. Pougin, M. Dilla, and J. Strunk, “Identification and exclusion of intermediates of photocatalytic CO2 reduction on TiO2 under conditions of highest purity,” *Phys. Chem. Chem. Phys.*, vol. 18, no. 16, pp. 10809–10817, 2016, doi: 10.1039/c5cp07148h.

[57] Y. Wei *et al.*, “Efficient photocatalysts of TiO2 nanocrystals-supported PtRu alloy nanoparticles for CO2 reduction with H2O: Synergistic effect of Pt-Ru,” *Appl.*

*Catal. B Environ.*, vol. 236, no. February, pp. 445–457, 2018, doi: 10.1016/j.apcatb.2018.05.043.

[58] K. Kočí *et al.*, “Influence of reactor geometry on the yield of CO2 photocatalytic reduction,” *Catal. Today*, vol. 176, no. 1, pp. 212–214, 2011, doi: 10.1016/j.cattod.2010.12.054.

[59] J. Albero, Y. Peng, and H. García, “Photocatalytic CO2Reduction to C2+ Products,” *ACS Catal.*, vol. 10, no. 10, pp. 5734–5749, 2020, doi: 10.1021/acscatal.0c00478.

[60] H. Takeda, H. Koizumi, K. Okamoto, and O. Ishitani, “Photocatalytic CO2 reduction using a Mn complex as a catalyst,” *Chem. Commun.*, vol. 50, no. 12, pp. 1491–1493, 2014, doi: 10.1039/c3cc48122k.

[61] J. Low, L. Zhang, T. Tong, B. Shen, and J. Yu, “TiO2/MXene Ti3C2 composite with excellent photocatalytic CO2 reduction activity,” *J. Catal.*, vol. 361, pp. 255–266, 2018, doi: 10.1016/j.jcat.2018.03.009.

[62] N. G. Moustakas and J. Strunk, “Photocatalytic CO2 Reduction on TiO2-Based Materials under Controlled Reaction Conditions: Systematic Insights from a Literature Study,” *Chem. - A Eur. J.*, vol. 24, no. 49, pp. 12739–12746, 2018, doi: 10.1002/chem.201706178.

[63] S. S. Bhosale, A. K. Kharade, S. Narra, S. M. Chang, and E. Wei-Guang Diau, “Self-Photocatalytic Splitting of Carbon Dioxide Using Co-cationic Perovskite Nanocrystals in the Absence of Water,” *ACS Energy Lett.*, vol. 8, no. 1, pp. 280–288, 2023, doi: 10.1021/acsenergylett.2c02342.

[64] W. Tu *et al.*, “An in situ simultaneous reduction-hydrolysis technique for fabrication of TiO2-graphene 2D sandwich-like hybrid nanosheets: Graphene-promoted selectivity of photocatalytic-driven hydrogenation and coupling of CO 2 into methane and ethane,” *Adv. Funct. Mater.*, vol. 23, no. 14, pp. 1743–1749, 2013, doi: 10.1002/adfm.201202349.

[65] J. Yu, J. Jin, B. Cheng, and M. Jaroniec, “A noble metal-free reduced graphene

oxide-cds nanorod composite for the enhanced visible-light photocatalytic reduction of CO2 to solar fuel," *J. Mater. Chem. A*, vol. 2, no. 10, pp. 3407–3416, 2014, doi: 10.1039/c3ta14493c.

[66] X. Zong *et al.*, "Enhancement of photocatalytic H2 evolution on CdS by loading MoS2 as cocatalyst under visible light irradiation," *J. Am. Chem. Soc.*, vol. 130, no. 23, pp. 7176–7177, 2008, doi: 10.1021/ja8007825.

[67] X. An, K. Li, and J. Tang, "Cu2O/reduced graphene oxide composites for the photocatalytic conversion of CO2," *ChemSusChem*, vol. 7, no. 4, pp. 1086–1093, 2014, doi: 10.1002/cssc.201301194.

[68] S. Wang *et al.*, "Application of COFs in capture / conversion of CO 2 and elimination of organic / inorganic pollutants," *Environ. Funct. Mater.*, no. March, 2023, doi: 10.1016/j.efmat.2023.03.001.

[69] X. Guan *et al.*, "Chemically stable polyarylether-based covalent organic frameworks," *Nat. Chem.*, vol. 11, no. 6, pp. 587–594, 2019, doi: 10.1038/s41557-019-0238-5.

[70] F. F. Chen *et al.*, "Upcycling of heavy metal adsorbents into sulfide semiconductors for photocatalytic CO2 reduction," *Appl. Surf. Sci.*, vol. 558, no. February, p. 149647, 2021, doi: 10.1016/j.apsusc.2021.149647.

[71] Q. Wang, Z. Fang, W. Zhang, and D. Zhang, "High-Efficiency g-C3N4 Based Photocatalysts for CO2 Reduction: Modification Methods," *Adv. Fiber Mater.*, vol. 4, no. 3, pp. 342–360, 2022, doi: 10.1007/s42765-021-00122-7.

[72] W. J. Ong, L. L. Tan, S. P. Chai, and S. T. Yong, "Graphene oxide as a structure-directing agent for the two-dimensional interface engineering of sandwich-like graphene-g-C3N4 hybrid nanostructures with enhanced visible-light photoreduction of CO2 to methane," *Chem. Commun.*, vol. 51, no. 5, pp. 858–861, 2015, doi: 10.1039/c4cc08996k.

[73] J. J. Leung, J. A. Vigil, J. Warnan, E. Edwardes Moore, and E. Reisner, " Rational Design of Polymers for Selective CO 2 Reduction Catalysis ," *Angew. Chemie*,

vol. 131, no. 23, pp. 7779–7783, 2019, doi: 10.1002/ange.201902218.

[74] X. Chi *et al.*, “Electronic Transmission Channels Promoting Charge Separation of Conjugated Polymers for Photocatalytic CO2 Reduction with Controllable Selectivity,” *Angew. Chemie - Int. Ed.*, vol. 362801, pp. 1–5, 2023, doi: 10.1002/anie.202303785.

[75] Q. Yang, P. Peng, and Z. Xiang, “Covalent organic polymer modified TiO2 nanosheets as highly efficient photocatalysts for hydrogen generation,” *Chem. Eng. Sci.*, vol. 162, pp. 33–40, 2017, doi: 10.1016/j.ces.2016.12.071.

[76] S. Kandambeth, A. Mallick, B. Lukose, M. V. Mane, T. Heine, and R. Banerjee, “Construction of crystalline 2D covalent organic frameworks with remarkable chemical (Acid/Base) stability via a combined reversible and irreversible route,” *J. Am. Chem. Soc.*, vol. 134, no. 48, pp. 19524–19527, 2012, doi: 10.1021/ja308278w.

[77] H. L. Nguyen and A. Alzamly, “Covalent Organic Frameworks as Emerging Platforms for CO2Photoreduction,” *ACS Catal.*, vol. 11, no. 15, pp. 9809–9824, 2021, doi: 10.1021/acscatal.1c02459.

[78] J. Wang *et al.*, “Covalently connected core–shell NH2-MIL-125@COFs-OH hybrid materials for visible-light-driven CO2 reduction,” *J. Colloid Interface Sci.*, vol. 637, pp. 1–9, 2023, doi: 10.1016/j.jcis.2022.12.154.

[79] Z. He, J. Goulas, E. Parker, Y. Sun, X. dong Zhou, and L. Fei, “Review on covalent organic frameworks and derivatives for electrochemical and photocatalytic CO2 reduction,” *Catal. Today*, vol. 409, no. April 2022, pp. 103–118, 2023, doi: 10.1016/j.cattod.2022.04.021.

[80] Y. Zhang, L. Cao, G. Bai, and X. Lan, “Engineering Single Cu Sites into Covalent Organic Framework for Selective Photocatalytic CO2 Reduction,” *Small*, vol. 2300035, pp. 1–10, 2023, doi: 10.1002/smll.202300035.

[81] R. Mercado, R. S. Fu, A. V. Yakutovich, L. Talirz, M. Haranczyk, and B. Smit, “In Silico Design of 2D and 3D Covalent Organic Frameworks for Methane Storage

Applications,” *Chem. Mater.*, vol. 30, no. 15, pp. 5069–5086, 2018, doi: 10.1021/acs.chemmater.8b01425.

[82] S. Bhunia, K. A. Deo, and A. K. Gaharwar, “2D Covalent Organic Frameworks for Biomedical Applications,” *Adv. Funct. Mater.*, vol. 30, no. 27, pp. 1–27, 2020, doi: 10.1002/adfm.202002046.

[83] S. B. Alahakoon, S. D. Diwakara, C. M. Thompson, and R. A. Smaldone, “Supramolecular design in 2D covalent organic frameworks,” *Chem. Soc. Rev.*, vol. 49, no. 5, pp. 1344–1356, 2020, doi: 10.1039/c9cs00884e.

[84] S. Q. Xu, T. G. Zhan, Q. Wen, Z. F. Pang, and X. Zhao, “Diversity of Covalent Organic Frameworks (COFs): A 2D COF Containing Two Kinds of Triangular Micropores of Different Sizes,” *ACS Macro Lett.*, vol. 5, no. 1, pp. 99–102, 2016, doi: 10.1021/acsmacrolett.5b00804.

[85] D. N. Bunck and W. R. Dichtel, “Bulk synthesis of exfoliated two-dimensional polymers using hydrazone-linked covalent organic frameworks,” *J. Am. Chem. Soc.*, vol. 135, no. 40, pp. 14952–14955, 2013, doi: 10.1021/ja408243n.

[86] S. M. J. Rogge *et al.*, “Metal-organic and covalent organic frameworks as single-site catalysts,” *Chem. Soc. Rev.*, vol. 46, no. 11, pp. 3134–3184, 2017, doi: 10.1039/c7cs00033b.

[87] S. Cao, B. Li, R. Zhu, and H. Pang, “Design and synthesis of covalent organic frameworks towards energy and environment fields,” *Chem. Eng. J.*, vol. 355, no. August 2018, pp. 602–623, 2019, doi: 10.1016/j.cej.2018.08.184.

[88] J. You, Y. Zhao, L. Wang, W. Bao, and Y. He, “Atomic layer deposition of γ-Fe2O3 nanoparticles on modified MWCNT for efficient adsorption of Cr(VI) ions from aqueous solution,” *J. Phys. Chem. Solids*, vol. 142, no. November 2019, p. 109441, 2020, doi: 10.1016/j.jpcs.2020.109441.

[89] T. Banerjee, K. Gottschling, G. Savasci, C. Ochsenfeld, and B. V. Lotsch, “H2 Evolution with Covalent Organic Framework Photocatalysts,” *ACS Energy Lett.*, vol. 3, no. 2, pp. 400–409, 2018, doi: 10.1021/acsenergylett.7b01123.

[90] W. Tu, Y. Xu, S. Yin, and R. Xu, “Rational Design of Catalytic Centers in Crystalline Frameworks,” *Adv. Mater.*, vol. 30, no. 33, pp. 1–29, 2018, doi: 10.1002/adma.201707582.

[91] Y. Zhang *et al.*, “Application of MOFs and COFs for photocatalysis in CO2 reduction, H2 generation, and environmental treatment,” *EnergyChem*, vol. 4, no. 4, p. 100078, 2022, doi: 10.1016/j.enchem.2022.100078.

[92] W. J. Ong, L. L. Tan, Y. H. Ng, S. T. Yong, and S. P. Chai, “Graphitic Carbon Nitride (g-C3N4)-Based Photocatalysts for Artificial Photosynthesis and Environmental Remediation: Are We a Step Closer to Achieving Sustainability?,” *Chem. Rev.*, vol. 116, no. 12, pp. 7159–7329, 2016, doi: 10.1021/acs.chemrev.6b00075.

[93] N. W. Ockwig, M. O. Keeffe, A. J. Matzger, and O. M. Yaghi, “Porous , Crystalline , Covalent Organic Frameworks,” vol. 310, no. November, pp. 1166–1171, 2005.

[94] D. Beaudoin, T. Maris, and J. D. Wuest, “Constructing monocrystalline covalent organic networks by polymerization,” *Nat. Chem.*, vol. 5, no. 10, pp. 830–834, 2013, doi: 10.1038/nchem.1730.

[95] P. Kuhn, M. Antonietti, and A. Thomas, “Porous, covalent triazine-based frameworks prepared by ionothermal synthesis,” *Angew. Chemie - Int. Ed.*, vol. 47, no. 18, pp. 3450–3453, 2008, doi: 10.1002/anie.200705710.

[96] F. J. Uribe-Romo, C. J. Doonan, H. Furukawa, K. Oisaki, and O. M. Yaghi, “Crystalline covalent organic frameworks with hydrazone linkages,” *J. Am. Chem. Soc.*, vol. 133, no. 30, pp. 11478–11481, 2011, doi: 10.1021/ja204728y.

[97] M. Zhang *et al.*, “Semiconductor/Covalent-Organic-Framework Z-Scheme Heterojunctions for Artificial Photosynthesis,” *Angew. Chemie*, vol. 132, no. 16, pp. 6562–6568, 2020, doi: 10.1002/ange.202000929.

[98] D. Stewart *et al.*, “Stable and ordered amide frameworks synthesised under reversible conditions which facilitate error checking,” *Nat. Commun.*, vol. 8, no. 1, pp. 1–9, 2017, doi: 10.1038/s41467-017-01423-5.

[99] F. J. Uribe-Romo, J. R. Hunt, H. Furukawa, C. Klöck, M. O'Keeffe, and O. M. Yaghi, "A crystalline imine-linked 3-D porous covalent organic framework," *J. Am. Chem. Soc.*, vol. 131, no. 13, pp. 4570–4571, 2009, doi: 10.1021/ja8096256.

[100] G. B. Wang *et al.*, "Covalent organic frameworks: emerging high-performance platforms for efficient photocatalytic applications," *J. Mater. Chem. A*, vol. 8, no. 15, pp. 6957–6983, 2020, doi: 10.1039/d0ta00556h.

[101] L. Niu *et al.*, "Hotpots and trends of covalent organic frameworks (COFs) in the environmental and energy field: Bibliometric analysis," *Sci. Total Environ.*, vol. 783, p. 146838, 2021, doi: 10.1016/j.scitotenv.2021.146838.

[102] Y. Yusran, Q. Fang, and S. Qiu, "Postsynthetic Covalent Modification in Covalent Organic Frameworks," *Isr. J. Chem.*, vol. 58, no. 9, pp. 971–984, 2018, doi: 10.1002/ijch.201800066.

[103] J. L. Segura, S. Royuela, and M. Mar Ramos, "Post-synthetic modification of covalent organic frameworks," *Chem. Soc. Rev.*, vol. 48, no. 14, pp. 3903–3945, 2019, doi: 10.1039/c8cs00978c.

[104] S. Yuan, X. Li, J. Zhu, G. Zhang, P. Van Puyvelde, and B. Van Der Bruggen, "Covalent organic frameworks for membrane separation," *Chem. Soc. Rev.*, vol. 48, no. 10, pp. 2665–2681, 2019, doi: 10.1039/c8cs00919h.

[105] Y. Chen *et al.*, "Covalent organic frameworks as a sensing platform for water in organic solvent over a broad concentration range," *Anal. Chim. Acta*, vol. 1109, pp. 114–121, 2020, doi: 10.1016/j.aca.2020.03.003.

[106] A. M. Elewa *et al.*, "Solvent polarity tuning to enhance the crystallinity of 2D-covalent organic frameworks for visible-light-driven hydrogen generation," *J. Mater. Chem. A*, vol. 10, no. 23, pp. 12378–12390, 2022, doi: 10.1039/d2ta00328g.

[107] S. Periyasamy and N. Viswanathan, "Hydrothermal Synthesis of Melamine-Functionalized Covalent Organic Polymer-Blended Alginate Beads for Iron Removal from Water," *J. Chem. Eng. Data*, vol. 64, no. 6, pp. 2280–2291, 2019,

doi: 10.1021/acs.jced.8b01085.

[108] C. Hu, Z. Zhang, S. Liu, X. Liu, and M. Pang, “Monodispersed CuSe Sensitized Covalent Organic Framework Photosensitizer with an Enhanced Photodynamic and Photothermal Effect for Cancer Therapy,” *ACS Appl. Mater. Interfaces*, vol. 11, no. 26, pp. 23072–23082, 2019, doi: 10.1021/acsami.9b08394.

[109] X. Ding *et al.*, “Synthesis of metallophthalocyanine covalent organic frameworks that exhibit high carrier mobility and photoconductivity,” *Angew. Chemie - Int. Ed.*, vol. 50, no. 6, pp. 1289–1293, 2011, doi: 10.1002/anie.201005919.

[110] E. L. Spitler *et al.*, “Lattice Expansion of Highly Oriented 2D Phthalocyanine Covalent Organic Framework Films,” *Angew. Chemie*, vol. 124, no. 11, pp. 2677–2681, 2012, doi: 10.1002/ange.201107070.

[111] G. Chen *et al.*, “Stable Hydrazone-Linked Covalent Organic Frameworks Containing O,N,O′-Chelating Sites for Fe(III) Detection in Water,” *ACS Appl. Mater. Interfaces*, vol. 11, no. 13, pp. 12830–12837, 2019, doi: 10.1021/acsami.9b02640.

[112] E. L. Spitler *et al.*, “A 2D covalent organic framework with 4.7-nm pores and insight into its interlayer stacking,” *J. Am. Chem. Soc.*, vol. 133, no. 48, pp. 19416–19421, 2011, doi: 10.1021/ja206242v.

[113] S. Wang *et al.*, “Pathway Complexity in the Stacking of Imine-Linked Macrocycles Related to Two-Dimensional Covalent Organic Frameworks,” *Chem. Mater.*, vol. 31, no. 17, pp. 7104–7111, 2019, doi: 10.1021/acs.chemmater.9b03088.

[114] W. Liu *et al.*, “A Scalable General Synthetic Approach toward Ultrathin Imine-Linked Two-Dimensional Covalent Organic Framework Nanosheets for Photocatalytic CO2 Reduction,” *J. Am. Chem. Soc.*, vol. 141, no. 43, pp. 17431–17440, 2019, doi: 10.1021/jacs.9b09502.

[115] M. Afshari and M. Dinari, “Synthesis of new imine-linked covalent organic framework as high efficient absorbent and monitoring the removal of direct fast scarlet 4BS textile dye based on mobile phone colorimetric platform,” *J. Hazard.*

*Mater.*, vol. 385, no. October 2019, p. 121514, 2020, doi: 10.1016/j.jhazmat.2019.121514.

[116] S. Y. Ding *et al.*, “Construction of covalent organic framework for catalysis: Pd/COF-LZU1 in Suzuki-Miyaura coupling reaction,” *J. Am. Chem. Soc.*, vol. 133, no. 49, pp. 19816–19822, 2011, doi: 10.1021/ja206846p.

[117] L. Stegbauer, K. Schwinghammer, and B. V. Lotsch, “A hydrazone-based covalent organic framework for photocatalytic hydrogen production,” *Chem. Sci.*, vol. 5, no. 7, pp. 2789–2793, 2014, doi: 10.1039/c4sc00016a.

[118] H. Wei, S. Chai, N. Hu, Z. Yang, L. Wei, and L. Wang, “The microwave-assisted solvothermal synthesis of a crystalline two-dimensional covalent organic framework with high CO2 capacity,” *Chem. Commun.*, vol. 51, no. 61, pp. 12178–12181, 2015, doi: 10.1039/c5cc04680g.

[119] S. Ren *et al.*, “Porous, fluorescent, covalent triazine-based frameworks via room-temperature and microwave-assisted synthesis,” *Adv. Mater.*, vol. 24, no. 17, pp. 2357–2361, 2012, doi: 10.1002/adma.201200751.

[120] R. K. Yadav, A. Kumar, N. J. Park, K. J. Kong, and J. O. Baeg, “A highly efficient covalent organic framework film photocatalyst for selective solar fuel production from CO2,” *J. Mater. Chem. A*, vol. 4, no. 24, pp. 9413–9418, 2016, doi: 10.1039/c6ta01625a.

[121] K. Lei *et al.*, “A Metal-Free Donor–Acceptor Covalent Organic Framework Photocatalyst for Visible-Light-Driven Reduction of CO2 with H2O,” *ChemSusChem*, vol. 13, no. 7, pp. 1725–1729, 2020, doi: 10.1002/cssc.201903545.

[122] J. Bi *et al.*, “A Cobalt-Modified Covalent Triazine-Based Framework as an Efficient Cocatalyst for Visible-Light-Driven Photocatalytic CO2 Reduction,” *Chempluschem*, vol. 84, no. 8, pp. 1149–1154, 2019, doi: 10.1002/cplu.201900329.

[123] P. L. Cheung and S. K. Lee, “Facile Solvent-Free Synthesis of Thin Iron Porphyrin

COFs on Carbon Cloth Electrodes for CO 2 Reduction," 2019, doi: 10.1021/acs.chemmater.8b04370.

[124] V. N. Gopalakrishnan, J. Becerra, E. F. Pena, M. Sakar, F. Béland, and T. Do, "materials : recent advances and future perspective," vol. 1, pp. 8332–8360, 2021, doi: 10.1039/d1gc02439f.

[125] S. Guo, Y. Xiao, and B. Jiang, "Encapsulation of Pd Nanoparticles in Covalent Triazine Frameworks for Enhanced Photocatalytic CO2Conversion," *ACS Sustain. Chem. Eng.*, 2021, doi: 10.1021/acssuschemeng.1c04176.

[126] R. Xu, X. S. Wang, H. Zhao, H. Lin, Y. B. Huang, and R. Cao, "Rhenium-modified porous covalent triazine framework for highly efficient photocatalytic carbon dioxide reduction in a solid-gas system," *Catal. Sci. Technol.*, vol. 8, no. 8, pp. 2224–2230, 2018, doi: 10.1039/c8cy00176f.

[127] H. J. Zhu *et al.*, "Efficient electron transmission in covalent organic framework nanosheets for highly active electrocatalytic carbon dioxide reduction," *Nat. Commun.*, vol. 11, no. 1, pp. 1–10, 2020, doi: 10.1038/s41467-019-14237-4.

[128] M. Lu *et al.*, " Rational Design of Crystalline Covalent Organic Frameworks for Efficient CO 2 Photoreduction with H 2 O ," *Angew. Chemie*, vol. 131, no. 36, pp. 12522–12527, 2019, doi: 10.1002/ange.201906890.

[129] J. Li *et al.*, "Metal-Free 2D/2D Black Phosphorus and Covalent Triazine Framework Heterostructure for CO2 Photoreduction," *ACS Sustain. Chem. Eng.*, vol. 8, no. 13, pp. 5175–5183, 2020, doi: 10.1021/acssuschemeng.9b07591.

[130] S. J. A. Moniz, S. A. Shevlin, D. J. Martin, Z. X. Guo, and J. Tang, "Visible-light driven heterojunction photocatalysts for water splitting-a critical review," *Energy Environ. Sci.*, vol. 8, no. 3, pp. 731–759, 2015, doi: 10.1039/c4ee03271c.

[131] X. Li *et al.*, "A review of material aspects in developing direct Z-scheme photocatalysts," *Mater. Today*, vol. 47, no. August, pp. 75–107, 2021, doi: 10.1016/j.mattod.2021.02.017.

[132] H. Wang *et al.*, "Semiconductor heterojunction photocatalysts: Design,

construction, and photocatalytic performances," *Chem. Soc. Rev.*, vol. 43, no. 15, pp. 5234–5244, 2014, doi: 10.1039/c4cs00126e.

[133] C. Martinez Suarez, S. Hernández, and N. Russo, "BiVO4 as photocatalyst for solar fuels production through water splitting: A short review," *Appl. Catal. A Gen.*, vol. 504, pp. 158–170, 2015, doi: 10.1016/j.apcata.2014.11.044.

[134] F. Stelo, N. Kublik, S. Ullah, and H. Wender, "Recent advances in Bi2MoO6 based Z-scheme heterojunctions for photocatalytic degradation of pollutants," *J. Alloys Compd.*, vol. 829, p. 154591, 2020, doi: 10.1016/j.jallcom.2020.154591.

[135] L. J. Zhang, S. Li, B. K. Liu, D. J. Wang, and T. F. Xie, "Highly efficient CdS/WO3 photocatalysts: Z-scheme photocatalytic mechanism for their enhanced photocatalytic H2 evolution under visible light," *ACS Catal.*, vol. 4, no. 10, pp. 3724–3729, 2014, doi: 10.1021/cs500794j.

[136] Q. Xu, L. Zhang, J. Yu, S. Wageh, A. A. Al-Ghamdi, and M. Jaroniec, "Direct Z-scheme photocatalysts: Principles, synthesis, and applications," *Mater. Today*, vol. 21, no. 10, pp. 1042–1063, 2018, doi: 10.1016/j.mattod.2018.04.008.

[137] W. Yu, J. Chen, T. Shang, L. Chen, L. Gu, and T. Peng, "Direct Z-scheme g-C3N4/WO3 photocatalyst with atomically defined junction for H2 production," *Appl. Catal. B Environ.*, vol. 219, pp. 693–704, 2017, doi: 10.1016/j.apcatb.2017.08.018.

[138] C. Cheng, B. He, J. Fan, B. Cheng, S. Cao, and J. Yu, "An Inorganic/Organic S-Scheme Heterojunction H2-Production Photocatalyst and its Charge Transfer Mechanism," *Adv. Mater.*, vol. 33, no. 22, pp. 1–8, 2021, doi: 10.1002/adma.202100317.

[139] C. Sun *et al.*, "Facile sonochemical synthesis of CdS/COF heterostructured nanocomposites and their enhanced photocatalytic degradation of Bisphenol-A," *Sep. Purif. Technol.*, vol. 271, no. February, p. 118873, 2021, doi: 10.1016/j.seppur.2021.118873.

[140] H. Ge, F. Xu, B. Cheng, J. Yu, and W. Ho, "S-Scheme Heterojunction TiO2/CdS

Nanocomposite Nanofiber as H2-Production Photocatalyst," *ChemCatChem*, vol. 11, no. 24, pp. 6301–6309, 2019, doi: 10.1002/cctc.201901486.

[141] J. Thote, H. B. Aiyappa, A. Deshpande, D. Díaz Díaz, S. Kurungot, and R. Banerjee, "A Covalent Organic Framework-Cadmium Sulfide Hybrid as a Prototype Photocatalyst for Visible-Light-Driven Hydrogen Production," *Chem. - A Eur. J.*, vol. 20, no. 48, pp. 15961–15965, 2014, doi: 10.1002/chem.201403800.

[142] R. L. Frost, D. A. Henry, M. L. Weier, and W. Martens, "Raman spectroscopy of three polymorphs of BiVO4: Clinobisvanite, dreyerite and pucherite, with comparisons to (VO4) 3-bearing minerals: namibite, pottsite and schumacherite," *J. Raman Spectrosc.*, vol. 37, no. 7, pp. 722–732, 2006, doi: 10.1002/jrs.1499.

[143] H. L. Tan, R. Amal, and Y. H. Ng, "Alternative strategies in improving the photocatalytic and photoelectrochemical activities of visible light-driven BiVO4: A review," *J. Mater. Chem. A*, vol. 5, no. 32, pp. 16498–16521, 2017, doi: 10.1039/c7ta04441k.

[144] Z. Zhao, Z. Li, and Z. Zou, "Electronic structure and optical properties of monoclinic clinobisvanite BiVO4," *Phys. Chem. Chem. Phys.*, vol. 13, no. 10, pp. 4746–4753, 2011, doi: 10.1039/c0cp01871f.

[145] L. E. Gomes *et al.*, "Enhanced photocatalytic activity of BiVO4/Pt/PtOx photocatalyst: The role of Pt oxidation state," *Appl. Surf. Sci.*, vol. 567, no. July, pp. 22–24, 2021, doi: 10.1016/j.apsusc.2021.150773.

[146] A. Walsh, Y. Yan, M. N. Huda, M. M. Al-Jassim, and S. H. Wei, "Band edge electronic structure of BiVO 4: Elucidating the role of the Bi s and V d orbitals," *Chem. Mater.*, vol. 21, no. 3, pp. 547–551, 2009, doi: 10.1021/cm802894z.

[147] M. Tayebi and B. K. Lee, "Recent advances in BiVO4 semiconductor materials for hydrogen production using photoelectrochemical water splitting," *Renew. Sustain. Energy Rev.*, vol. 111, no. May, pp. 332–343, 2019, doi: 10.1016/j.rser.2019.05.030.

[148] S. Wang *et al.*, "Vacancy defect engineering of BiVO4photoanodes for

photoelectrochemical water splitting," *Nanoscale*, vol. 13, no. 43, pp. 17989–18009, 2021, doi: 10.1039/d1nr05691c.

[149] X. Zhang, Z. Ai, F. Jia, L. Zhang, X. Fan, and Z. Zou, "Selective synthesis and visible-light photocatalytic activities of BiVO4 with different crystalline phases," *Mater. Chem. Phys.*, vol. 103, no. 1, pp. 162–167, 2007, doi: 10.1016/j.matchemphys.2007.02.008.

[150] Y. Park, K. J. Mc Donald, and K. S. Choi, "Progress in bismuth vanadate photoanodes for use in solar water oxidation," *Chem. Soc. Rev.*, vol. 42, no. 6, pp. 2321–2337, 2013, doi: 10.1039/c2cs35260e.

[151] J. K. Cooper *et al.*, "Indirect bandgap and optical properties of monoclinic bismuth vanadate," *J. Phys. Chem. C*, vol. 119, no. 6, pp. 2969–2974, 2015, doi: 10.1021/jp512169w.

[152] L. Zou, H. Wang, and X. Wang, "High Efficient Photodegradation and Photocatalytic Hydrogen Production of CdS/BiVO4 Heterostructure through Z-Scheme Process," *ACS Sustain. Chem. Eng.*, vol. 5, no. 1, pp. 303–309, 2017, doi: 10.1021/acssuschemeng.6b01628.

[153] Z. Zhang, W. Wang, M. Shang, and W. Yin, "Photocatalytic degradation of rhodamine B and phenol by solution combustion synthesized BiVO4 photocatalyst," *Catal. Commun.*, vol. 11, no. 11, pp. 982–986, 2010, doi: 10.1016/j.catcom.2010.04.013.

[154] J. Mao, T. Peng, X. Zhang, K. Li, and L. Zan, "Selective methanol production from photocatalytic reduction of CO 2 on BiVO 4 under visible light irradiation," *Catal. Commun.*, vol. 28, pp. 38–41, 2012, doi: 10.1016/j.catcom.2012.08.008.

[155] X. Wang *et al.*, "BiVO4 /Bi4Ti3O12 heterojunction enabling efficient photocatalytic reduction of CO2 with H2O to CH3OH and CO," *Appl. Catal. B Environ.*, vol. 270, no. January, 2020, doi: 10.1016/j.apcatb.2020.118876.

[156] X. Li, D. Wei, L. Ye, and Z. Li, "Fabrication of Cu 2 O-RGO/BiVO 4 nanocomposite for simultaneous photocatalytic CO 2 reduction and benzyl

alcohol oxidation under visible light," *Inorg. Chem. Commun.*, vol. 104, no. February, pp. 171–177, 2019, doi: 10.1016/j.inoche.2019.04.012.

[157] X. Deng *et al.*, "Metal-Organic Framework Coating Enhances the Performance of Cu2O in Photoelectrochemical CO2 Reduction," *J. Am. Chem. Soc.*, vol. 141, no. 27, pp. 10924–10929, 2019, doi: 10.1021/jacs.9b06239.

[158] L. K. S. Ng *et al.*, "Mesoporous SiO 2 /BiVO 4 /CuO x nanospheres for Z-scheme, visible light aerobic C–N coupling and dehydrogenation," *Appl. Mater. Today*, vol. 15, pp. 192–202, 2019, doi: 10.1016/j.apmt.2019.01.010.

[159] J. C. Wang *et al.*, "Enhanced photoreduction CO2 activity over direct Z-Scheme α-Fe2O3/Cu2O heterostructures under visible light irradiation," *ACS Appl. Mater. Interfaces*, vol. 7, no. 16, pp. 8631–8639, 2015, doi: 10.1021/acsami.5b00822.

[160] C. Zhou, S. Wang, Z. Zhao, Z. Shi, S. Yan, and Z. Zou, "A Facet-Dependent Schottky-Junction Electron Shuttle in a BiVO4{010}–Au–Cu2O Z-Scheme Photocatalyst for Efficient Charge Separation," *Adv. Funct. Mater.*, vol. 28, no. 31, pp. 1–10, 2018, doi: 10.1002/adfm.201801214.

[161] W. K. Jo and N. C. S. Selvam, "Z-scheme CdS/g-C3N4 composites with RGO as an electron mediator for efficient photocatalytic H2 production and pollutant degradation," *Chem. Eng. J.*, vol. 317, pp. 913–924, 2017, doi: 10.1016/j.cej.2017.02.129.

[162] Z. Duan, X. Zhao, and L. Chen, "BiVO4/Cu0.4V2O5composites as a novel Z-scheme photocatalyst for visible-light-driven CO2conversion," *J. Environ. Chem. Eng.*, vol. 9, no. 1, p. 104628, 2021, doi: 10.1016/j.jece.2020.104628.

[163] J. Bian *et al.*, "Energy Platform for Directed Charge Transfer in the Cascade Z-Scheme Heterojunction: CO2 Photoreduction without a Cocatalyst," *Angew. Chemie - Int. Ed.*, vol. 60, no. 38, pp. 20906–20914, 2021, doi: 10.1002/anie.202106929.

[164] M. Lu *et al.*, "Remarkable photocatalytic activity enhancement of CO2 conversion over 2D/2D g-C3N4/BiVO4 Z-scheme heterojunction promoted by efficient

interfacial charge transfer," *Carbon N. Y.*, vol. 160, pp. 342–352, 2020, doi: 10.1016/j.carbon.2020.01.038.

[165] Q. Zhang *et al.*, "Extracting hot holes from plasmonic semiconductors for photocatalysis," *Appl. Catal. B Environ.*, vol. 317, no. March, p. 121792, 2022, doi: 10.1016/j.apcatb.2022.121792.

[166] Y. Li *et al.*, "2D/2D heterostructure of ultrathin BiVO4/Ti3C2 nanosheets for photocatalytic overall Water splitting," *Appl. Catal. B Environ.*, vol. 285, no. December 2020, p. 119855, 2021, doi: 10.1016/j.apcatb.2020.119855.

[167] S. Głowniak, B. Szczęśniak, J. Choma, and M. Jaroniec, "Advances in Microwave Synthesis of Nanoporous Materials," *Adv. Mater.*, vol. 33, no. 48, pp. 1–28, 2021, doi: 10.1002/adma.202103477.

[168] Y. N. Gong, X. Guan, and H. L. Jiang, "Covalent organic frameworks for photocatalysis: Synthesis, structural features, fundamentals and performance," *Coord. Chem. Rev.*, vol. 475, p. 214889, 2023, doi: 10.1016/j.ccr.2022.214889.